INFORMATION TO USERS

This manuscript has been reproduced from the microfilm master. UMI films the text directly from the original or copy submitted. Thus, some thesis and dissertation copies are in typewriter face, while others may be from any type of computer printer.

The quality of this reproduction is dependent upon the quality of the copy submitted. Broken or indistinct print, colored or poor quality illustrations and photographs, print bleedthrough, substandard margins, and improper alignment can adversely affect reproduction.

In the unlikely event that the author did not send UMI a complete manuscript and there are missing pages, these will be noted. Also, if unauthorized copyright material had to be removed, a note will indicate the deletion.

Oversize materials (e.g., maps, drawings, charts) are reproduced by sectioning the original, beginning at the upper left-hand corner and continuing from left to right in equal sections with small overlaps.

Photographs included in the original manuscript have been reproduced xerographically in this copy. Higher quality 6" x 9" black and white photographic prints are available for any photographs or illustrations appearing in this copy for an additional charge. Contact UMI directly to order.

ProQuest Information and Learning
300 North Zeeb Road, Ann Arbor, MI 48106-1346 USA
800-521-0600

UMI®

Sub-millimeter Tests of the Gravitational Inverse-Square Law

Charles D. Hoyle, Jr.

A dissertation submitted in partial fulfillment
of the requirements for the degree of

Doctor of Philosophy

University of Washington

2001

Program Authorized to Offer Degree: Physics

UMI Number: 3036486

ProQuest Information and Learning Company
300 North Zeeb Road
P.O. Box 1346
Ann Arbor, MI 48106-1346

In presenting this dissertation in partial fulfillment of the requirements for the Doctoral degree at the University of Washington, I agree that the Library shall make its copies freely available for inspection. I further agree that extensive copying of this dissertation is allowable only for scholarly purposes, consistent with "fair use" as prescribed in the U.S. Copyright Law. Requests for copying or reproduction of this dissertation may be referred to Bell and Howell Information and Learning, 300 North Zeeb Road, Ann Arbor, MI 48106-1346, to whom the author has granted "the right to reproduce and sell (a) copies of the manuscript in microform and/or (b) printed copies of the manuscript made from microform."

Signature__________________

Date 10/01/01

University of Washington
Graduate School

This is to certify that I have examined this copy of a doctoral dissertation by

Charles D. Hoyle, Jr.

and have found that it is complete and satisfactory in all respects,
and that any and all revisions required by the final
examining committee have been made.

Chair of Supervisory Committee:

Eric G. Adelberger
Eric G. Adelberger

Reading Committee:

Eric G. Adelberger
Eric Adelberger

Jens Gundlach

Blayne Heckel

Date: 10/01/01

University of Washington

Abstract

Sub-millimeter Tests of the Gravitational Inverse-Square Law

by Charles D. Hoyle, Jr.

Chair of Supervisory Committee:

Professor Eric G. Adelberger
Department of Physics

The Newtonian Law of Universal Gravitation states that the strength of the gravitational force between point test bodies falls as the inverse-square of the distance between them. Recently, novel new theoretical scenarios, inspired by string or M theory, predict possible violations of this inverse-square behavior with test mass separations below 1 mm.

Motivated by these theories, we tested the gravitational inverse-square law at separations ranging down to 138 μm using 10-fold symmetric torsion pendulums and rotating 10-fold symmetric attractors. We improved previous constraints on inverse-square law violations by up to a factor of 10^4 and saw no deviations from Newtonian physics. These measurements describe the first direct observation of the gravitational interaction with test mass separations below 0.5 mm.

We performed two similar experiments denoted by 'I' and 'II' throughout the text. This dissertation includes thorough descriptions of the apparatus, analysis procedures, and results of these experiments.

TABLE OF CONTENTS

LIST OF FIGURES

LIST OF TABLES

ACKNOWLEDGMENTS

I would like to sincerely thank those who made the work described in this dissertation enjoyable, enlightening, and possible.

The members of the Eöt-Wash group have been, of course, invaluable to this effort. Eric Adelberger's knowledge, attention to detail, and enthusiasm were crucial to the development and ultimate success of these experiments. With his widespread knowledge of experimental and theoretical physics, he contributed enormously to my graduate education.

Blayne Heckel's help, intuition, and understanding made the laboratory a stimulating and enjoyable place to be every day.

Jens Gundlach's insight into solving many mechanical and experimental problems was invaluable.

Erik Swanson designed and built the majority of the electronic components used in the experiments, as well as the data-taking software.

The bulk of the analysis programs and the all of the code used for the calculation of the Newtonian and Yukawa torques were written by Ulrich Schmidt. His knowledge of all things statistical and computational was extremely helpful.

I thank Greg Smith for his assistance and patience during my first two years with the Eöt-Wash group.

In addition to being good friends, Dan Kapner and I spent the long hours in the laboratory necessary to perform the experiments in a reasonable amount of time.

I would also like to thank the Eöt-Wash undergraduates Nathan Collins, Angela

Kopp and Deb Spain for assistance with the apparatus.

Hank Simons and Jim Elms machined the precision pieces we needed with patience and extreme accuracy. Their skills and good humors are much appreciated.

Furthermore, the staff of the Nuclear Physics Laboratory and the Physics Department helped me navigate the ins and outs of the graduate school. Barbara Fulton, Karin Hendrickson, Kate Higgins, and Kimberly Hawley receive my greatest thanks for their assistance.

In my first year of study, I labored over many problem sets with Christian D'Urso and enjoyed the great hospitality and friendship of he and his wife, Cathy LaValley.

I would like to thank my parents, who fascinated me with science from an early age, for their love, encouragement, and support (emotional and financial).

My greatest thanks go to Catherine Keil, for giving me the love and support I needed, when I needed it most.

Chapter 1

INTRODUCTION AND MOTIVATION

1.1 The Newtonian Law of Universal Gravitation

Although gravity was the first of the fundamental forces to be described mathematically, it remains the most intriguing after over three hundred years of experimentation. Newton's law of universal gravitation states that the force between two point test bodies of separation $\vec{r}$ and masses m_1 and m_2 is given by the familiar equation

$$\vec{F}_{12} = -G\,\frac{m_1\,m_2\,\hat{r}}{r^2} = -m_1\,\vec{g}_2, \tag{1.1}$$

where G is the coupling strength and we have defined the gravitational field of m_2 to be $\vec{g}_2$. The inverse-square dependence on the separation ensures that the gravitational field satisfies Gauss' Law in the three spatial dimensions:

$$\oint_S \vec{g}_2\cdot d\vec{a} = 4\pi G\,m_2, \tag{1.2}$$

where the integral runs over any closed boundary, S, containing the mass m_2 with surface normal $d\vec{a}$. Gauss' Law demonstrates the fact that there are no gravitational sources in empty space.

In actuality, Newton's formulation is the weak field limit of the more comprehensive, classical metric theory of General Relativity, formulated by Einstein. However, for most practical purposes the assumption of inverse-square behavior is valid. General Relativity itself is a vastly successful theory that predicts several effects that have been experimentally confirmed. Such effects include the precession of the perihelion of Mercury [1], gravitational radiation from binary pulsar systems [2], gravitational red shift effects [3], and lensing phenomena [4].

1.2 The Standard Model of Particle Physics

The success of General Relativity is rivaled only by the success of the Standard Model of particle physics. This model is based entirely on the principles of quantum field theory where the fundamental fermions are taken to be point particles. The successful predictions of the Standard Model are far too long to list; however, the model does not incorporate the gravitational interaction.

Although many have attempted to formulate a quantum field theory of gravity, there has been no successful integration of General Relativity into the Standard Model. Such a unification is necessary for several reasons. For example, General Relativity predicts a point singularity at the center of a black hole. Since quantum field theory deals with phenomena that occur at very small length scales, a complete quantum theory must be able to describe physics at the singularity. The Standard Model, in its present form, is unable to describe the properties of the singularity.

Another curiosity associated with gravity is its extreme weakness compared to the strong, electromagnetic, and weak interactions of the Standard Model. This seemingly unnatural hierarchy has led to the construction of theories which attempt to solve this problem.

The Standard Model has internal inconsistencies of its own. The model fails to predict such fundamental values such as the magnitude of CP violation, the smallness of the cosmological constant, and the observed particle/antiparticle asymmetry.

It is thus generally assumed that a complete model exists which includes a fully quantum mechanical description of gravity and the predictions of the Standard Model, as well as correcting its inconsistencies. Many of these candidate theories predict exotic new phenomena that are either ruled out by existing observations or too small to have been observed by previous experiments. Some of these proposed phenomena appear as modifications of the gravitational inverse-square law (ISL) at untested distance scales.

1.3 String Theory: The Quantum Theory of Gravity?

In recent years, string theories have received much attention as candidate unification models. These theories describe the Standard Model particles as pieces of open string and the graviton as a closed loop of string, instead of point particles. String theories also require spatial dimensions in addition to the known three. The number and size of these dimensions is of great debate, however. In these models, the standard model particles are constrained to exist on a 3+1-dimensional subspace of the "bulk" geometry.

Until recently, it was assumed that the effects of string theory do not become apparent until one probes distances of order the Planck length,

$$R_P = \sqrt{G\hbar/c^3} = 1.6 \times 10^{-33}\ \text{cm}. \tag{1.3}$$

Such a small distance corresponds to an energy (the Planck mass) of $M_P = 1.2 \times 10^{16}$ TeV and is unreachable by any foreseeable high-energy experiment. Novel recent scenarios have, however, reduced the predicted energy scale associated with string theory or provided models that predict effects in the experimentally observable realm, while simultaneously resolving the hierarchy problem.

1.4 *Scenarios Predicting a Violation of the Inverse-Square Law*

Several theoretical scenarios predict violations of the gravitational ISL potentially detectable by the work described in this thesis.

1.4.1 Large Extra Dimensions

A very exciting recent class of string-inspired models [5, 6], invoked to solve the hierarchy problem, conjectures the existence of large spatial dimensions in addition to the three familiar ones. In its simplest form, the framework assumes that the fundamental energy scale of gravity is the same as that of the Standard Model, about 1 TeV. The apparent weakness of gravity is then interpreted as a consequence of the fact that gravitons are free to propagate in all spatial dimensions, while the particles and fields of the Standard Model are confined to a 3+1-dimensional "brane." Thus, if we assume n large extra dimensions of equal size R^* and the fundamental Planck mass is $M^* = 1$ TeV, one concludes [5]

$$R^* = \frac{\hbar c}{M^* c^2}\left(\frac{M_P}{M^*}\right)^{2/n} . \tag{1.4}$$

According to Equation 1.4, if there were one large extra dimension it would have size $\sim 3 \times 10^{13}$ m. This case is excluded by the concordance of celestial mechanics with inverse-square behavior. Table 1.1 shows the predicted size of the large extra dimensions as a function of their number. Because the gravitational field must obey Gauss' Law in 3+n dimensions in the bulk geometry, the presence of extra dimensions would transform the ISL to a $1/r^{(2+n)}$ dependence when test masses are separated by a distance $r << R^*$. With a test mass separation $r \gtrsim R^*$, the presence of the extra dimensions appears as a Yukawa modification to the Newtonian potential [7, 8]:

$$V(r) = -G\frac{m_1 m_2}{r}\left(1 + \alpha e^{-r/\lambda}\right), \tag{1.5}$$

Table 1.1: Size of "large" extra dimensions as a function of their number according to Equation 1.4. We have assumed the fundamental Planck mass to be $M^* = 1$ TeV, and that all of the "large" extra dimensions have the same size.

n	1	2	3	4	5	6	7
R^* (m)	10^{13}	10^{-3}	10^{-8}	10^{-11}	10^{-12}	10^{-14}	10^{-14}

where α determines the strength of the deviation relative to Newtonian gravity and λ is its characteristic range. In the simplest scenarios, $\lambda = R^*$ and $\alpha = n + 1$ or $\alpha = 2n$ for compactification of the extra dimensions on a n-sphere or n-torus, respectively [7, 8].

The case of $n = 2$ is of interest for our experiment. If there were two large extra dimensions, we should see a deviation from the gravitational ISL at a length scale of ~1 mm with strength 3-4 times that of gravity. Meaningful measurements for $n > 2$ are inaccessible to mechanical experiments due to the very small distance scale associated with the predicted ISL violation, if one assumes that all of the extra dimensions are of equal size. However, it has been recently noted [9] that one may constrain the size of the *largest* extra dimension for any n from ISL tests.

It should be noted that the previous scenario is just one of a class of extra-dimensional theories. Other models [10] allow very large (or infinite) extra dimensions with no observable effect on the ISL.

1.4.2 New Particles

String theories inherently contain scalar partners of the graviton (dilaton) and fundamental fermions (moduli) that may generate Yukawa interactions that could appear in tests of the gravitational ISL. If supersymmetry is broken at low energies, these scalar particles would produce mm-scale effects [11, 12]. The range, λ, of the new interaction depends on the mass of the mediating particle ($\lambda \propto 1/M_{particle}$). The prediction of the strength of these effects relative to gravity is, however, less precise than that of the extra dimension scenarios. In general, the interactions have a strength much greater than gravity.

1.4.3 A Small Cosmological Constant

It is of some interest [13] that the observed size of the energy density of cosmological constant, $\Lambda = 3$ keV/cm^3, deduced from distant Type-1A supernovae [14, 15], corresponds to a length scale of $\sqrt[4]{\hbar c/\Lambda} \approx 0.1$ mm. In fact, scenarios have been proposed [16] that "explain" the small value of Λ by invoking an ISL violation at this sub-millimeter scale.

1.5 Existing Experimental Constraints on an Inverse-Square Law Violation

Several approaches yield constraints on violations of the gravitational ISL.

1.5.1 Parameterization

In general, we may parameterize a deviation from inverse-square behavior by the addition of a Yukawa term to the Newtonian potential (Eq. 1.5). For the simple extra-dimension scenarios, λ denotes the size of the extra dimensions, while for new interactions, λ is determined by the properties of the mediating particles. The strength, α, of these effects may lie in a vast region. Negative results of searches for a violation of the gravitational ISL are interpreted as constraints in the $\alpha - \lambda$ parameter space.

1.5.2 Astrophysical Bounds

The orbits of planets and artificial satellites obey Kepler's Laws to high precision, indicating that the ISL holds to high precision on the distance scale of the solar system. A good review of large distance limits is given by Fischbach and Talmage [17].

Astrophysical data may also be used to constrain the size of extra dimensions. The observation of the cooling rate of SN1987A gives the best such limits. If the extra dimensions are large, energy will be deposited in them during a supernova and the cooling will therefore be accelerated and fewer neutrinos will be emitted. Assuming standard stellar model parameters, the data from SN1987A gives an upper limit [18, 19] of $R^* \lesssim 1\ \mu\mathrm{m}$ for $n = 2$. However, this limit does not directly test the gravitational ISL, only a specific theoretical scenario allows it to be interpreted as such a test.

1.5.3 Constraints from High Energy Physics

The best chance for probing the possibility of more than two large extra dimensions comes from high energy collider experiments. Such experiments look either for the energy lost in a collision when a graviton is emitted into the extra dimensions, or the effect of virtual graviton exchange on angular distributions. Recent results [20, 21, 22] have set limits of $R^* \lesssim 0.6$ mm for $n = 2$. However, these results again do not directly test the gravitational ISL.

1.5.4 Laboratory Bounds

Laboratory scale experiments provide the best direct measure of the ISL in the millimeter regime. Figure 1.1 shows the 95% confidence level constraints on a direct observation of a Yukawa ISL violation as they stood before our measurement. The three heavy curves were obtained from torsion balance experiments; the region above

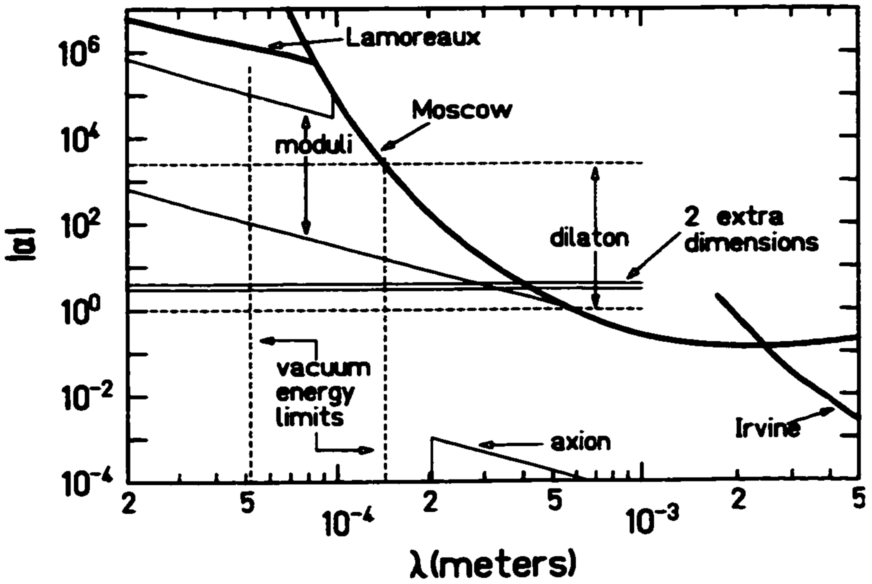

Figure 1.1: Existing 95% confidence upper limits on a short-range Yukawa violation of the gravitational inverse-square law. The region excluded by previous torsion balance experiments [23, 24, 25] lies above the heavy lines labeled Lamoreaux, Moscow, and Irvine, respectively. The constraints and predictions are adapted from Ref. [26], except for the dilaton prediction which is from Ref. [11].

the curves is excluded. We see there is little information on a gravitational strength interaction (or gravity itself) for distances less than ~ 1 mm. Also shown in the figure are expected regions associated with the theoretical predictions described above.

1.6 Goals of This Experiment

Through the work described in this thesis, we aimed to be the first to observe the gravitational interaction and test the validity of the gravitational ISL at distances of less than 0.5 mm. We used a sensitive torsion balance instrument specially designed for this purpose. This thesis describes two separate experiments denoted by 'I' and 'II.' The experiments were similar and only the relevant differences will be noted.

Chapter 2

APPARATUS

This chapter describes the main components of our torsion balance instrument. We begin with a general overview of the experimental technique, then proceed with detailed descriptions of the individual parts of the apparatus.

2.1 General Principles of the Eöt-Wash Short-Range Instrument

Torsion balances have been widely used for over 200 years to study the gravitational interaction. However, to study gravity at length scales much smaller than had been studied before, we had to develop a new type of torsion balance. Figure 2.1 shows the basic design of our instrument.

A torsion pendulum was suspended in a vacuum by an 80-cm-long, 20-μm-diameter tungsten fiber above a rotating attractor mass. A tightly stretched, 20-μm-thick, gold-coated BeCu membrane between the pendulum and attractor prevented any electrostatic communication between the two. The "active" components of the pendulum and attractor were circular plates containing 10 holes evenly spaced about the azimuth (ideally local vertical). The attractor consisted of two stacked disks. The tenfold rotational symmetry of the attractor created a torque on the pendulum which varied periodically at a fundamental frequency of 10ω, where ω was the attractor rotation frequency. Because the torque did not vary as a pure sinusoid, higher harmonics were also present, i.e., torques which varied periodically at 20ω, 30ω, etc. The lower attractor disk contained holes located azimuthally between those in the upper

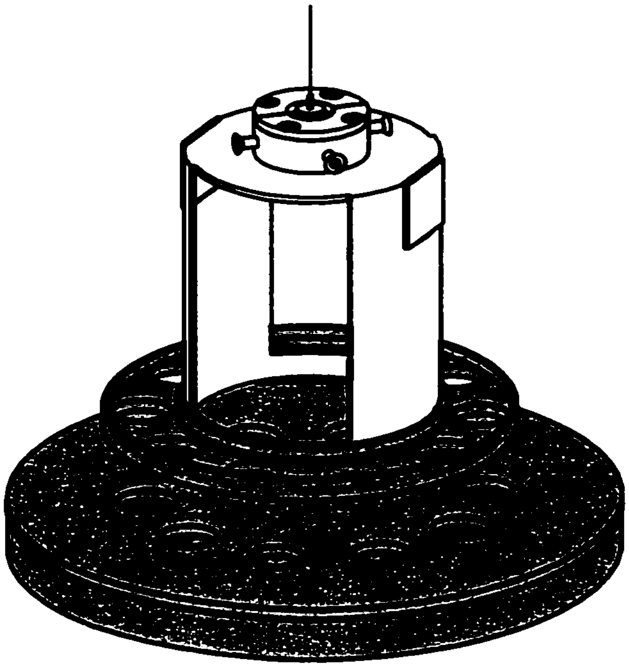

Figure 2.1: Torsion pendulum and rotating attractor for Experiment I. The active components are shaded. For clarity, we show an unrealistically large 1.5 cm vertical separation between pendulum and attractor, and omit the conducting membrane and attractor drive mechanism. The four horizontal screws at the top of the pendulum were adjusted to make the pendulum level, as described in Section 3.1.

disk. These holes greatly reduced the 10ω torque from Newtonian gravity, while 10ω torque arising from a short-range interaction was not suppressed. An interaction with a range small compared to the upper disk thickness did not "see" the bottom disk.

The torque on the pendulum was inferred from the pendulum twist angle, θ, which we measured by reflecting an autocollimator light beam from mirrors mounted on the pendulum frame. The amplitude of the twist oscillations was determined by the driving torque, the torsional spring constant, κ, of the suspension fiber, and the rotational inertia of the pendulum. The twist was measured as a function of the vertical separation as well as the horizontal offset between the pendulum and

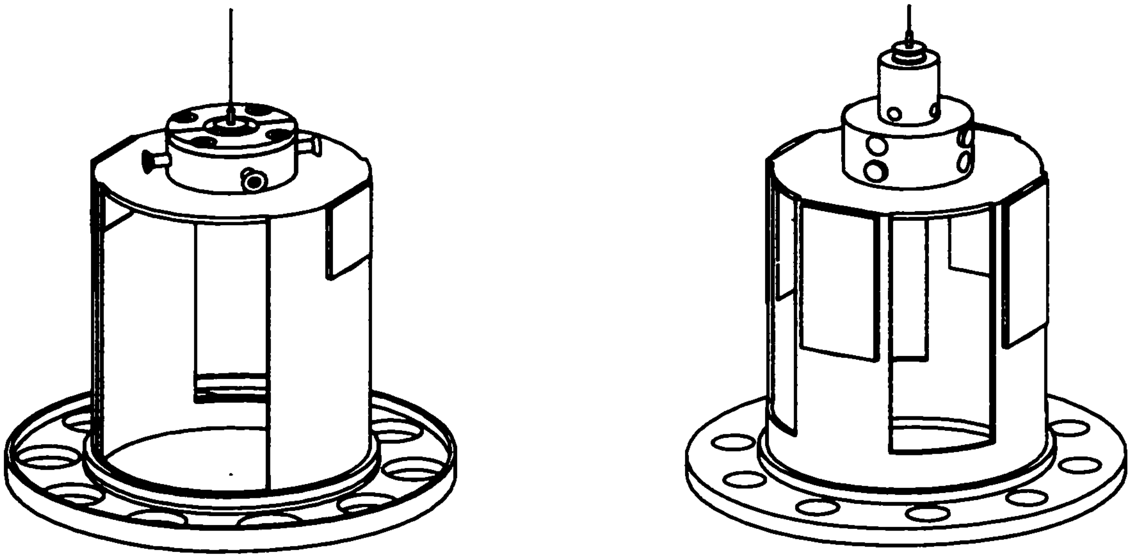

Figure 2.2: Torsion pendulums used in the two experiments. The pendulum used in Experiment I, shown on the left, had a frame with two-fold rotational symmetry, while the frame for Experiment II had four-fold symmetry. The mirrors for reflecting the light beam and leveling screws are shown. In Experiment I, the screws moved the fiber attachment point, while in Experiment II, screws were driven through the pendulum body to translate the center of mass of the pendulum (see Section 3.1).

attractor. After accounting for pendulum inertia, electronic effects, and calibration issues, the harmonic components of the torque were extracted from the measured twist. Finally, these measured torques were compared to calculated values from a detailed model that included predictions for Newtonian as well as possible Yukawa contributions to the torque (see Chapter 5).

2.2 The Torsion Pendulums

The torsion pendulums used in the two experiments, shown in Figure 2.2, differed somewhat, although the principle of the measurement remained unchanged.

2.2.1 The Active Mass Rings

The active masses of the two pendulums were rings made from 7075 aluminum with 10 torque-producing holes evenly spaced about the azimuth. The most important properties of the rings were the dimensions, placement and the "missing mass" of the holes, that is, the mass removed by drilling the holes.

The ring used in Experiment I had outer and inner diameters of 67.591±0.003 mm and 42.036±0.003 mm, respectively. The ten 9.545±0.003-mm-diameter (average diameter) holes were placed on a 55.33±0.01-mm-diameter circle, as measured with a measuring microscope. The thickness of the active region of the plate was measured mechanically to be 2.002±0.002 mm. Thicker lips on the inner and outer edge of the ring provided rigidity and mounting ability. The average mass of an individual hole was 0.3972±0.0004 g. All quoted masses include small corrections for buoyancy in air and the thin layer of evaporated gold that covered the entire surface. The layer of gold provided an electrostatic equipotential surface to reduce effects from local charge build-up. The whole pendulum and its enclosure as well as the top of the upper attractor plate were gold coated for this same reason.

In the Experiment II ring, the holes had an average diameter of 6.375±0.003 mm and were on a 53.33±0.01-mm-diameter circle. The thickness of the active part of the ring was 2.979±0.002 mm. These holes had an average individual mass of 0.266177±0.000014 g.

2.2.2 Frame and Adjustment Screws

The supporting frames for the pendulum rings were machined from aluminum. The frame for Experiment I (II) had two-fold (four-fold) azimuthal symmetry. The two (four) mirrors were 1.25 cm wide, 0.10 cm thick, and spanned 1.25 cm (2.50 cm) vertically. The upper portion of the frame contained the screws used to align the

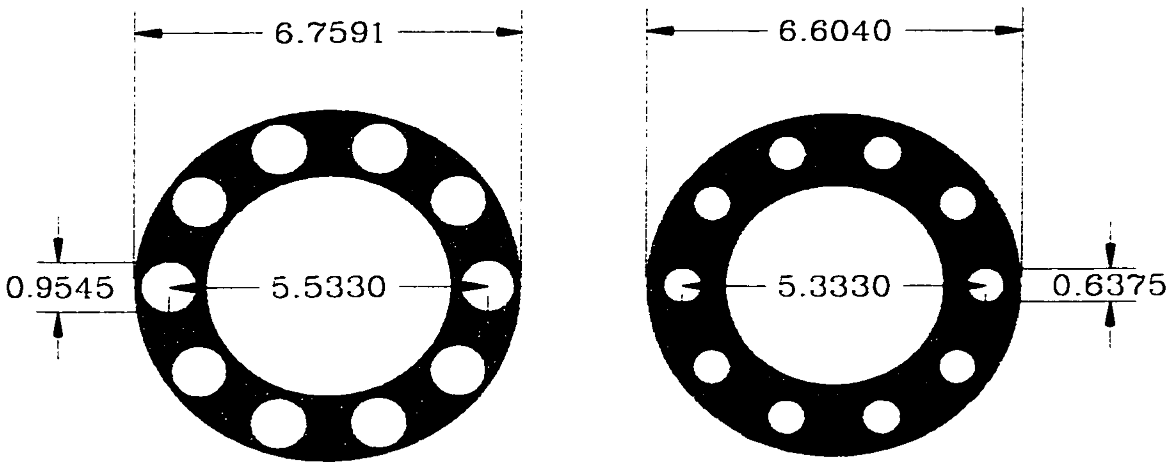

Figure 2.3: Top view of the pendulum rings used in the two experiments. The ring for Experiment I is on the left, Experiment II's on the right. The drawings are exactly two-thirds scale and all dimensions are in centimeters.

pendulum disk to the horizontal (see Section 3.1). The total mass of the frame including adjusting screws and mirrors was 18.5494±0.0001 g (23.2832±0.0001 g).

2.3 The Pendulum Suspension

The pendulum suspension system consisted of the torsion fiber and devices used to reduce possible systematic effects. This section describes this system, which was affixed to a stainless steel shaft that passed through the upper lid of the vacuum chamber.

2.3.1 Torsion Fiber

The torsion fiber was 80-cm-long, 20-μm-diameter, gold-coated tungsten. The fiber attached directly to the top of the pendulum frame via a crimp tube that was embedded in a copper 4-40 screw. The breaking strength of the fiber was approximately 100 g. Thus, the pendulum masses, <40 g, were well below the fiber breaking strength.

The diameter and length of the fiber were set by the existing conditions in the apparatus when this measurement began [27].

2.3.2 Prehanger

A 3-cm-long, 150-μm-diameter fiber was attached directly to the stainless steel shaft (see Figure 2.4). This "prehanger," being torsionally stiff to any pendulum motion, served to reduce any tilt-twist coupling to the torsion fiber by acting as a gimbal. It is well known (see, for example, [28], pp. 77) that a tilt of the fiber attachment creates a corresponding twist in the fiber. The prehanger also served as a suspension for the magnetic damper disk.

2.3.3 Magnetic Damper

A magnetic eddy current damper was placed in series between the torsion fiber and the prehanger. The damper consisted of an aluminum shaft and disk suspended between two sets of 3 ceramic ring magnets. As the fiber executed its simple pendulum "swing" mode, eddy currents were induced that damped this motion. The typical exponential damping time of such oscillations was approximately 1000 s. The axial symmetry of the damper plate reduced potential damping of the torsional motion.

2.3.4 Fiber Heat Treatment

Our tungsten torsion fibers had a slight built-in helicity that produced a steady unwinding of the fiber over time. We called this phenomenon 'drift.' The drift decreased exponentially with time, but was a strong function of temperature. Also, if the load was removed from the fiber, the next loading would initially result in drift rates of > 100 μrad/hr.

Although the drift was removed in our analysis, we always took data on the same

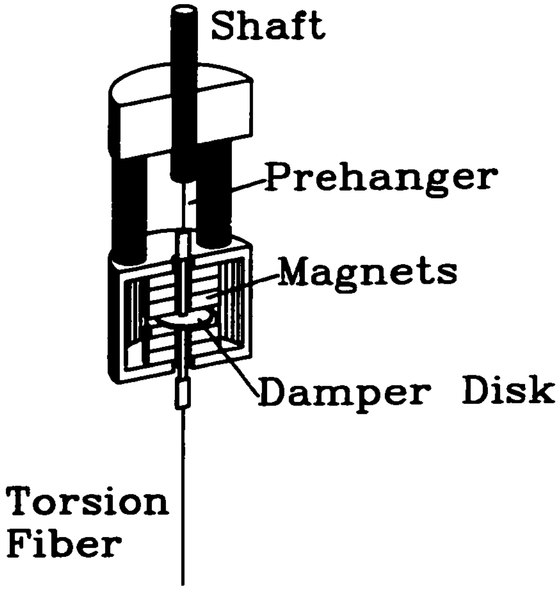

Figure 2.4: Prehanger and magnetic damper used to suppress the simple pendulum mode and tilt-twist feed through of the torsion fiber.

region of the detector to avoid local detector calibration anomalies; therefore, we did not want the fiber drift to move the laser beam out of position. We reduced the drift by heating the fiber. While the pendulum was suspended, we ran hot air ($\sim$70°C) through tubing attached to a massive copper 'shroud' surrounding the fiber in the vacuum chamber. We ran the hot air for 12-24 hrs. After cooling for an additional day, the drift was typically ≤ 1 μrad/hr.

2.3.5 Fiber Positioning Mechanism

It was essential to precisely position the pendulum relative to the attractor. The positioning mechanism, to which the suspension fiber was attached, was outside the vacuum chamber at the top of the instrument (see Figure 2.5). The mechanism was a 4-axis translation and rotation platform. Three electronically controlled micrometers (Newport Corporation model CMA-25PP) positioned 3 mutually perpendicular stages, X, Y, and Z. A rotation stage (Newport Corporation model URM80APE) controlled to equilibrium position of the torsion fiber and provided the ability to remove torsional energy from the pendulum.

The shaft which held the pendulum suspension was fed through the vacuum vessel via a compressed O-ring seal, and a welded bellows allowed horizontal and vertical translation. The full range of vertical translation was 25 mm, while the shroud limited horizontal travel to 6 mm.

Stage Alignment

The three translation stages were not absolutely mutually perpendicular. The horizontal stages were measured to be misaligned with local horizontal capacitively. The capacitance between the pendulum was recorded as the X and Y-stages were moved (see Figure 2.6). The misalignment (X-stage: 8 mrad, Y-stage: 2 mrad) was well within tolerable limits. The vertical separation values used in the data analysis were corrected for this misalignment based upon the capacitance measurements.

Calibration of Micrometers

The absolute calibration of the electronically controlled micrometers caused us much trouble. Initially we assumed that the specifications of the micrometers were correct. However, the Experiment I data did not agree well with Newtonian predictions. Experiment II was designed solely to confirm this discrepancy. We realized during Experiment II that the deviation was entirely due to a faulty micrometer calibration.

We measured the distance moved by each micrometer with precision mechanical counterparts. We compared the electronic and mechanical values and got a highly linear relationship. The results are summarized in Figure 2.7 and Table 2.1. The

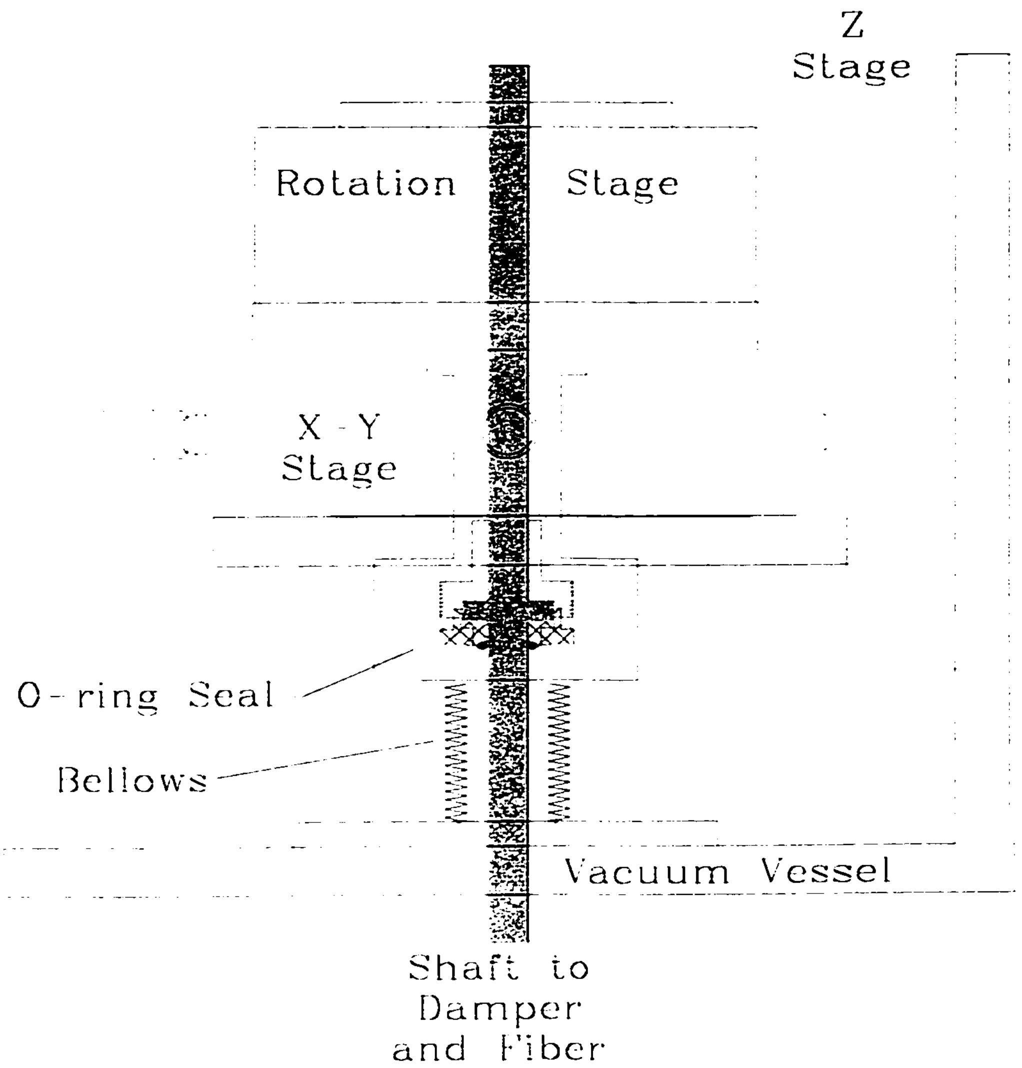

Figure 2.5: Schematic side view of the fiber positioner. The X, Y, and Z stages each contained remotely controlled micrometers. The bellows allowed horizontal and vertical translation, while the O-ring served as a vacuum rotation seal.

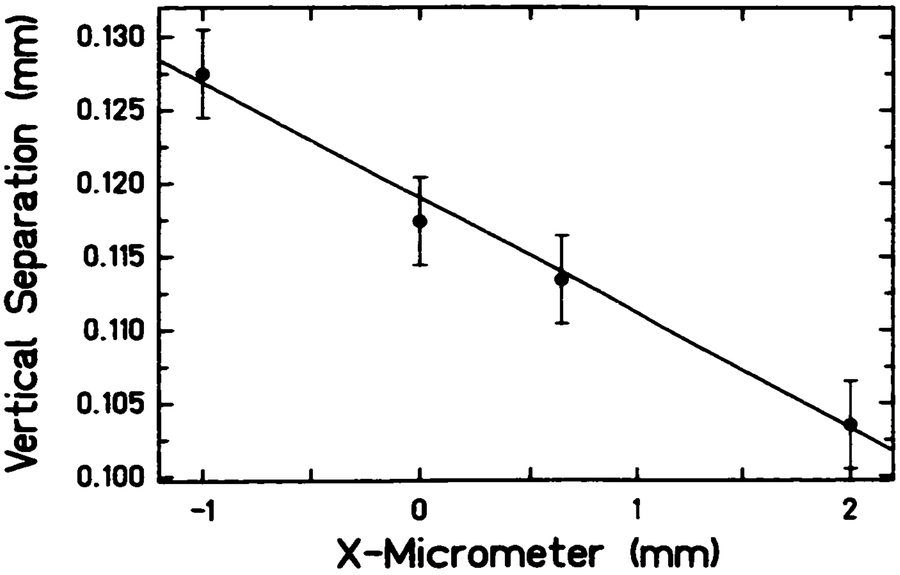

Figure 2.6: Dependence of the vertical separation on the horizontal position. The slope of the fit line shows the X stage to be tilted by 8 mrad from the horizontal.

positions values used in the analysis were corrected with the appropriate calibration.

2.4 The Rotating Attractor and Conducting Membrane

The rotating attractors for Experiments I and II consisted of two flat, coaxial copper disks. The upper disk was thinner and contained holes which, when properly rotated, aligned with those on the pendulum. The torque produced by these holes on the pendulum was defined as 'in-phase.' The lower disk contained 10 holes rotated by $\frac{\pi}{10}$ relative to those in the upper plate and were hence called 'out-of-phase' (the upper attractor disk in Experiment II also contained out-of-phase holes). The out-of-phase holes reduced the 10ω torque from Newtonian gravity, while leaving any 10ω torque from a short-range interaction intact. The 10ω Newtonian torque vanished for one

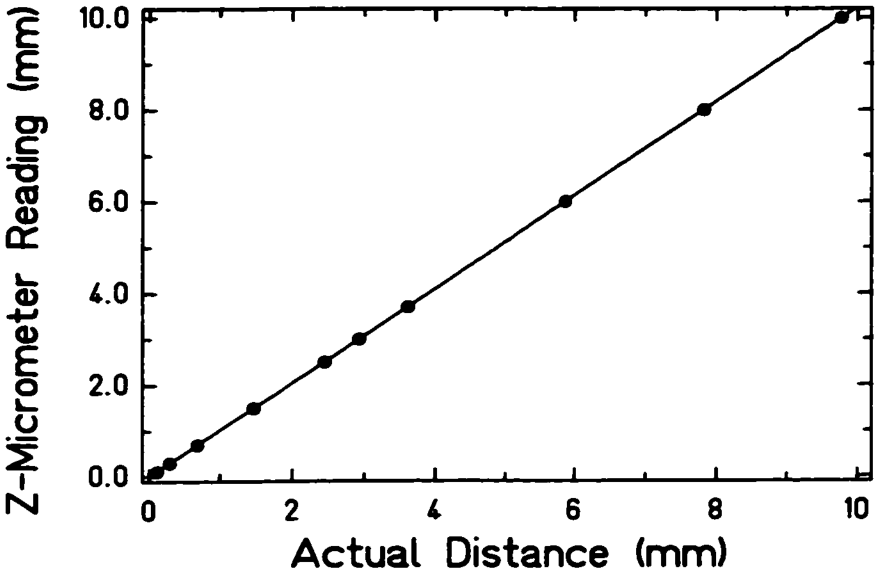

Figure 2.7: Calibration of the electronic Z-micrometer with a precision mechanical stage. The slope of the best fit line is 1.0230±0.0002, not the expected slope of 1.0000. The error bars are smaller than the size of the points.

Table 2.1: Results of measuring the displacement of the computer controlled micrometers with precision manual counterparts. The ratios reveal that the stages did not move as far as expected.

Micrometer	(Electronic Micrometer Reading)/(True Distance)
X	1.0239 ± 0.0002
Y	1.0248 ± 0.0002
Z	1.0230 ± 0.0002

particular vertical separation. The position of this cancelation was highly dependent upon the presence of an inverse-square law violation and provided the high sensitivity of our measurement.

2.4.1 The Active Disks

The disks for both experiments were made from high-purity copper and were lapped to a flatness of ±0.003 mm. The two sides of each disk were also parallel to < 30 μrad. The top surface of the upper disks was coated with gold. Tables 2.2 and 2.3 show the relevant dimensions of the disks for the two experiments. In the tables, all dimensions are average, R_c refers to the distance of the holes from the rotation axis, and the masses are given for an individual hole. The determination of the masses is discussed in Section 4.2.2.

When assembled, the angular misalignment of the two disks, measured using a microscope, was 0.00±0.01 degrees (0.13±0.01 degrees). The angular alignment was maintained with three pins that passed through holes in the upper and lower disks. The parallelism and flatness of the disks was inferred by measuring their individual thicknesses and then the total thickness when assembled. The gap between the plates was measured to be 10±10 μm (1.4±1.0 μm).

2.4.2 Conducting Membrane

The BeCu membrane between the pendulum and attractor prevented any electrostatic interaction between the pieces. The membrane was a 20-μm-thick, 11.4-cm-diameter foil, tightly stretched like a drum between two aluminum rings. The membrane and rings were assembled in a liquid nitrogen bath. After the unit warmed to room temperature, the differential thermal expansion between the BeCu and the aluminum rings created the high tension necessary to hold the foil flat. The tension was sufficient

Table 2.2: Dimensions of the attractor disks used in Experiment I. The upper disk holes are "in-phase," while those of the lower disk are "out-of-phase."

Dimension	Upper Disk	Lower Disk
Disk Diameter (mm)	99.846 ± 0.003	99.825 ± 0.003
Thickness (mm)	1.846 ± 0.005	7.825 ± 0.005
Hole Diameter (mm)	9.558 ± 0.003	12.715 ± 0.003
Hole Mass (g)	1.1770 ± 0.0004	8.8666 ± 0.0019
R_c (mm)	27.655 ± 0.005	27.665 ± 0.005

Table 2.3: Properties of the attractor disks used in Experiment II. The "In-Phase" and "Out-of-Phase" columns refer to the upper disk holes. The holes in the lower disk are out-of-phase.

Dimension	In-Phase	Out-of-Phase	Lower Disk
Disk Dia. (mm)	99.911 ± 0.003	99.911 ± 0.003	99.911 ± 0.003
Thickness (mm)	3.005 ± 0.002	3.005 ± 0.002	6.998 ± 0.002
Hole Dia. (mm)	6.386 ± 0.003	9.544 ± 0.003	15.939 ± 0.003
Hole Mass (g)	0.86228 ± 0.00004	1.92592 ± 0.00005	12.50984 ± 0.00006
R_c (mm)	26.685 ± 0.005	38.695 ± 0.005	36.665 ± 0.005

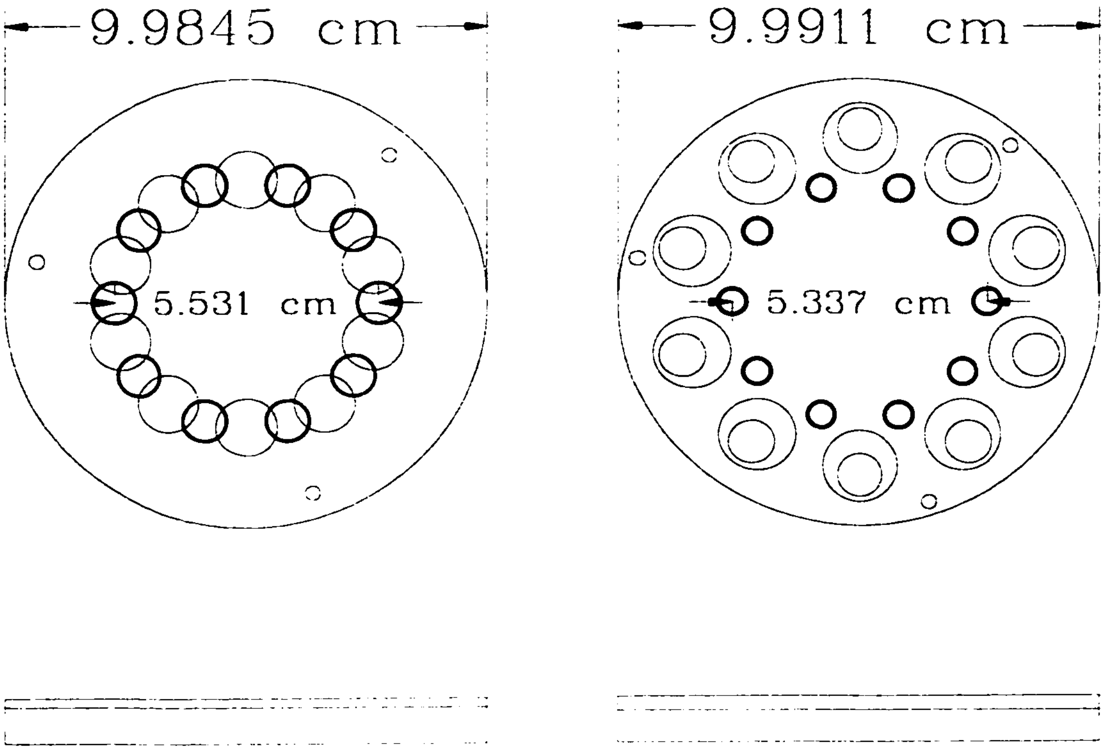

Figure 2.8: Top and side views of the attractor disks used in the two experiments. The disks from Experiment I are on the left. The blue circles represent the in-phase upper plate holes. The dark circles are the out-of-phase holes in the upper and lower attractor plates. The three small holes used to maintain the angular alignment of the plates are also shown.

to give a fundamental drum-head frequency of ~850 Hz to the membrane. This frequency was measured by sweeping a variable frequency acoustical source while watching the motion of small particles placed on the membrane. The frequency at which the particles first began to jiggle as the frequency was raised signified the resonance. Upon inspection with a microscope, the membrane was found to be flat to within ±15 μm.

2.4.3 Attractor Holder and Adjustment

The degree of parallelism of the attractor and pendulum was one factor that determined the minimum attainable separation, as well as the accuracy of the calculated torques. The alignment was accomplished in two steps. First, the attractor was made parallel to the conducting membrane. Second, the pendulum was made parallel to the membrane.

The attractor was held in a copper cup with three-fold symmetry. The symmetry was designed to allow for gravitational centering (see, for example, Ref. [28], pp. 71), but was ultimately not used as a more effective method was found. The cup was mounted to a shaft and bearing assembly (see Figure 2.10). The entire bearing assembly was mounted on 3 leveling screws that allowed us to achieve the desired level of parallelism. The leveling procedure is discussed in Section 3.2.2.

2.4.4 Rotation Drive and Angle Readout

The attractor drive motor was mounted on the outside of the vacuum vessel and a friction clutch transmitted the rotation to the attractor. Figure 2.10 shows the arrangement. The clutch surfaces were 2 sanded aluminum disks with mating conical flanges. A shaft passed through a bearing and a compressed O-ring vacuum seal to the motor. The drive motor was a 48 pole stepper motor with a 5000:1 reduction

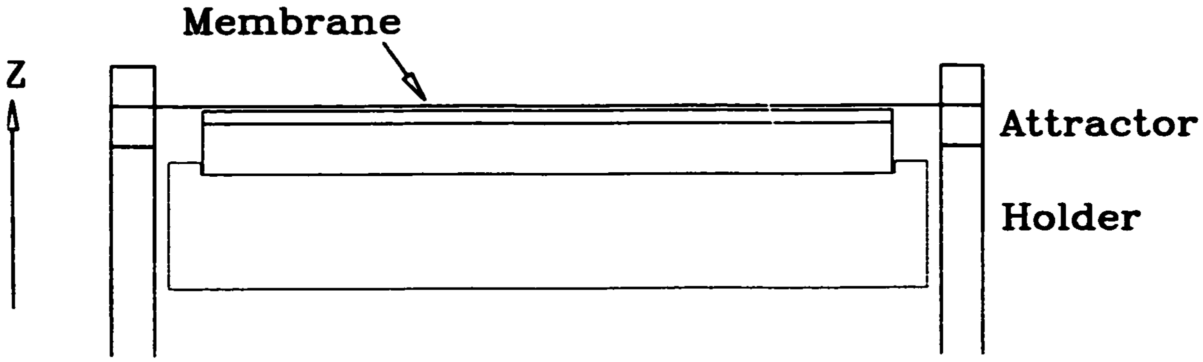

Figure 2.9: Side view of the attractor, its holder, and the conducting membrane. For a more detailed view of the attractor and holder, see Figure 2.10.

ratio (SAIA-Burgess model 276), giving 240,000 steps per attractor revolution.

The attractor angle, determined by counting the motor drive pulses, was checked every revolution by a LED/photodiode pair that was interrupted once per cycle by a tab on the friction clutch. The instant when the light became unobscured produced an index pulse read by our data taking computer. The index was constant to within 0.1 degrees during the course of a single run (~10 attractor cycles).

2.5 Autocollimator

The pendulum twist was measured by the autocollimator shown in Figure 2.11. The light from a 20 mW, 780 nm, actively stabilized laser diode (Sony SLD301), placed at the focus of a 30 cm lens, passed through a collimator to produce a 6-mm-diameter beam of parallel light. The parallel beam passed through an antireflective window in the vacuum vessel, bounced off two 45° mirrors, and then struck one of the pendulum mirrors. The light was reflected off the pendulum and into a 90° mirror mounted below the second 45° mirror. The light then returned to the pendulum and retraced its path to the autocollimator. A polarizing beamsplitter and 1/4-wave plate ensured

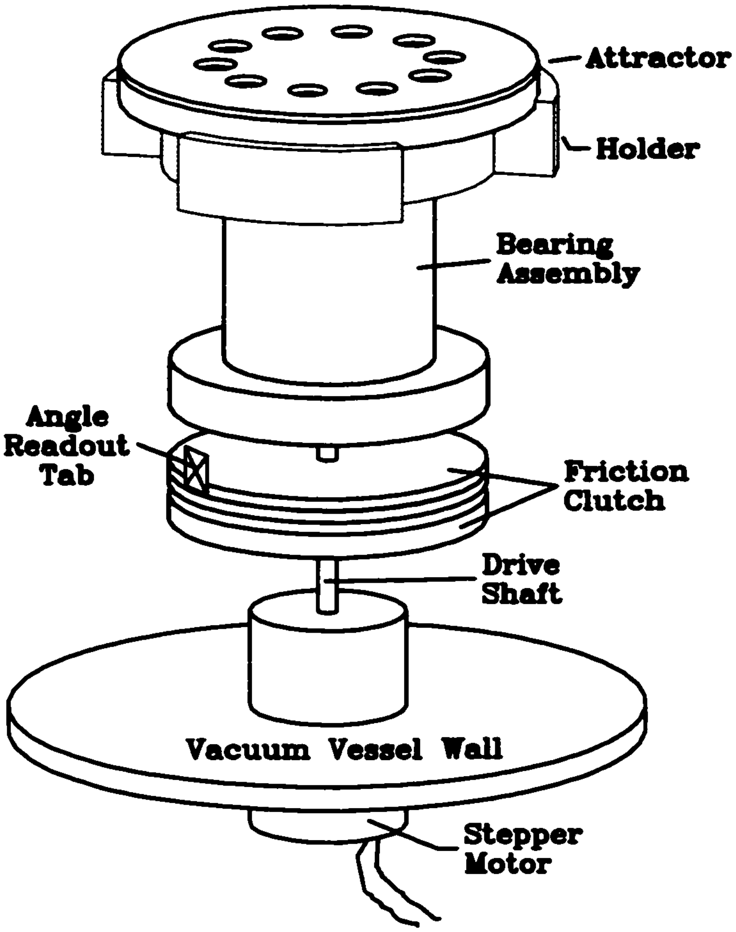

Figure 2.10: Schematic diagram of the attractor drive mechanism.

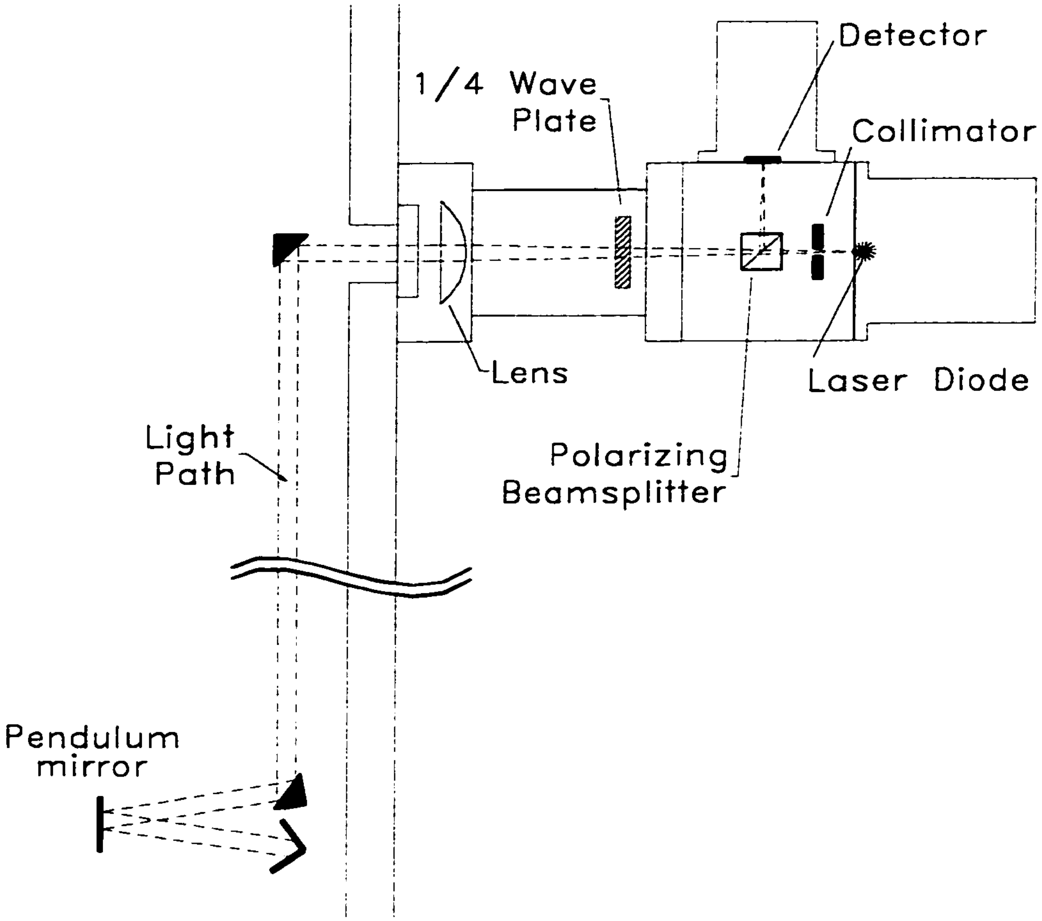

Figure 2.11: Schematic diagram of the autocollimator that measured the pendulum twist.

that no light bound for the detector returned to the laser diode.

The position-sensitive detector (United Detector Technology 1x3 mm model) was a 3 terminal analog resistive-division device. The light spot (focused to a diameter of about 0.1 mm at the detector location) released photoelectrons in the semiconductor strip. The resistance the electrons encountered was proportional to the distance from the light spot to the detector edge. Thus, the difference in currents, Δ received at the two ends of the detector located the light spot, while the sum of the currents from both sides of the detector, Σ, was nominally independent of the light spot position. We inferred the position from the ratio Δ/Σ (for details of the calibration, see Section 4.2.1). This normalization reduced any variations due to laser power fluctuations.

The laser beam was chopped with a TTL square wave at 141.7 Hz. The chop frequency was produced by a lock-in amplifier (Stanford Research Systems model SR830). Lock-in techniques were then used to measure the difference and sum currents through identical amplifiers sharing a common reference trigger. The reference phases of the Δ and Σ signals were adjusted at the lock-ins to maximize the signals. The lock-in output voltages were digitized and recorded by the data-taking computer (see Section 2.10).

2.6 Vacuum Vessel

The vacuum vessel was the one used in the Rot-Wash short-range equivalence principle test ([27], [28], and [29]). A small ion pump kept the pressure inside the chamber near 10^{-6} Torr. An ion pump was preferred because it produced no mechanical vibration of the vessel. Figure 2.12 shows a side view of the vacuum chamber. The entire vessel could be tilted with leveling screws for alignment purposes (see Section 3.3).

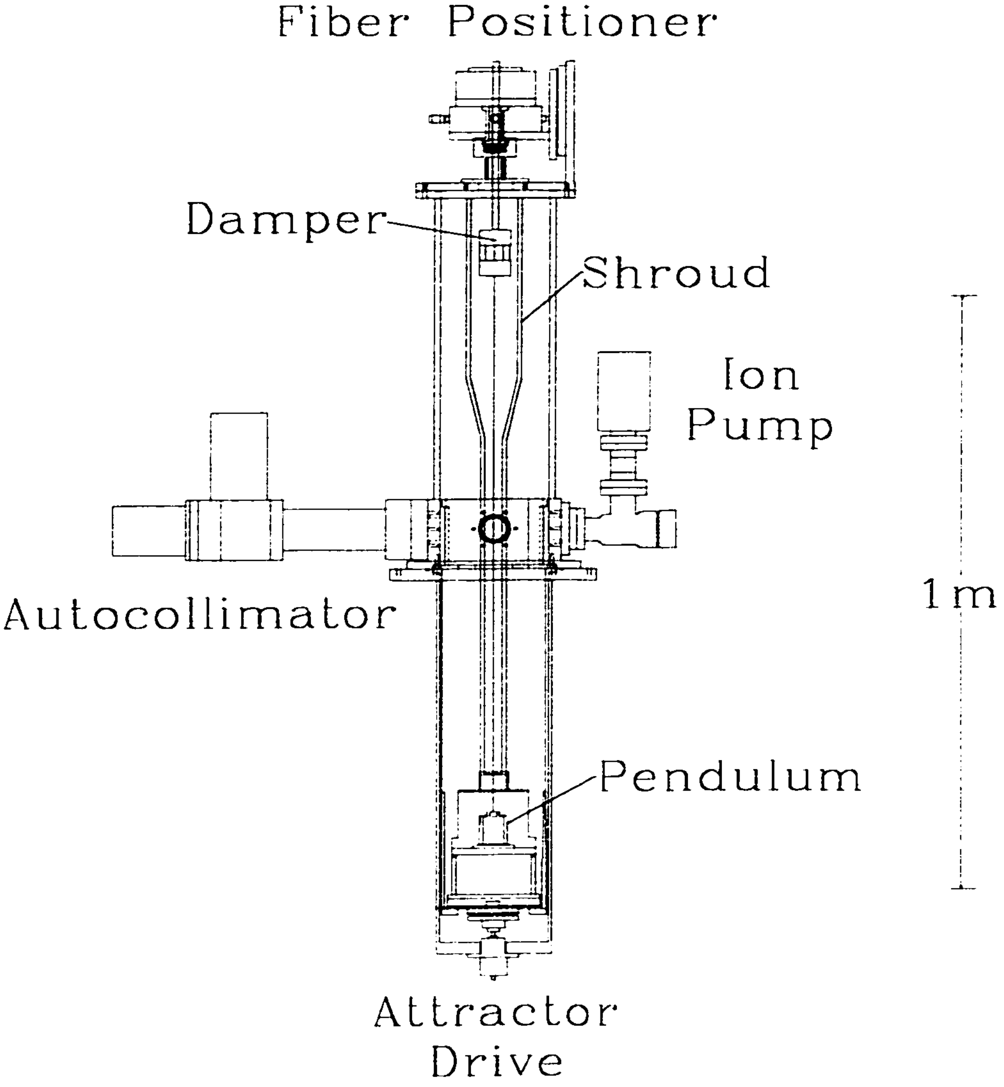

Figure 2.12: Schematic side-view of the vacuum vessel.

2.7 Environmental Monitors

2.7.1 Tilt

Two electronic tilt sensors (Applied Geomechanics Instruments model 755) were affixed to the top of the vacuum vessel. The two sensors were mounted at a relative angle of 120 degrees. The sensors were used in leveling procedures (Section 3.3) as well as determining systematic effects (Section 4.1.2).

2.7.2 Seismic

One vertical and one horizontal seismometer (Teledyne Geotech model S-500), mounted on the vacuum vessel support frame, monitored seismic disturbances during Experiment II.

2.7.3 Temperature

We used solid state temperature sensors (Analog Devices model AD590) that produced a current proportional to the absolute temperature to measure the temperature variations of the apparatus and the air around it. The currents were converted to voltages and fed into the data taking computer (see Section 2.10). The sensors produced 1 μA per degree Kelvin. Eight sensors were monitored, their locations are summarized in Table 2.4. All sensors were encased in small copper blocks to reduce the noise and increase the short-term stability of the readings. The sensors were used for evaluating systematic effects, as in Section 4.1.1, as well as diagnostic purposes.

Table 2.4: Placement of the temperature monitors.

Temperature Sensor	Location
T1	Bottom of vacuum vessel
T2	Top of vacuum vessel
T3	Autocollimator
T4	Bottom air
T5	Radiator water bath
T6	Middle air
T7	Top air
T8	Room air

2.8 Mechanical Support and Shielding

2.8.1 Supporting Structure

The vacuum vessel was placed on a kinematic mount that was directly attached to an unused cyclotron magnet in our laboratory. The magnet was less sensitive to building vibrations and sway because it had an independent foundation and a mass of 200 tons.

2.8.2 Thermal Shielding

The entire apparatus and sensitive electronics were enclosed in a thermally insulating box. The box walls, ceiling and floor were made of 5-cm-thick foam. An external device (Neslab model RTE-221) kept a constant temperature water supply circulating through a radiator/fan assembly inside the thermal enclosure. The variation of the air temperature inside the box was ≤ 30 mK/day.

2.8.3 Magnetic Shielding

A single layer of 0.76-mm-thick mu-metal surrounded the outside of the lower half of the vacuum chamber. This shielding reduced the ambient field by a factor of ~80. The constant residual field inside the chamber was <5 mG.

2.9 Calibration Turntable

The gravitational calibration, described in Section 4.2.1, required an external turntable surrounding the vacuum vessel. This turntable is depicted in Figure 2.14. The turntable was made from aluminum and driven by a motor identical to that which drove the attractor; it also had a similar angle index marker. The turntable sat on leveling screws which allowed for vertical positioning and alignment. The turntable plate had 6 evenly spaced holes sized to seat two 5.08 cm-diameter brass spheres used in the gravitational calibration. The distance between the centers of the spheres was 27.965±0.008 cm.

2.10 Data Acquisition and Sensor Calibration

Data was recorded by a 80286 computer with an Analogic LSDAS-16 interface card. The card contained 16 channels, each of which having 16-bit analog-to-digital converters that converted the input voltages to analog-to-digital units (ADU's). Outputs on the card allowed the user to control the attractor rotation speed. The acquisition software was written in Turbo Pascal. All sensors were recorded through this board, the temperature sensors being multiplexed. Table 2.5 lists the sensors normally recorded. Readings from the sensors were converted to physical units for diagnostic and systematic checks. All sensors had calibration coefficients, c_i, given by

$$V = c_0 + c_1(ADU) + c_2(ADU)^2, \tag{2.1}$$

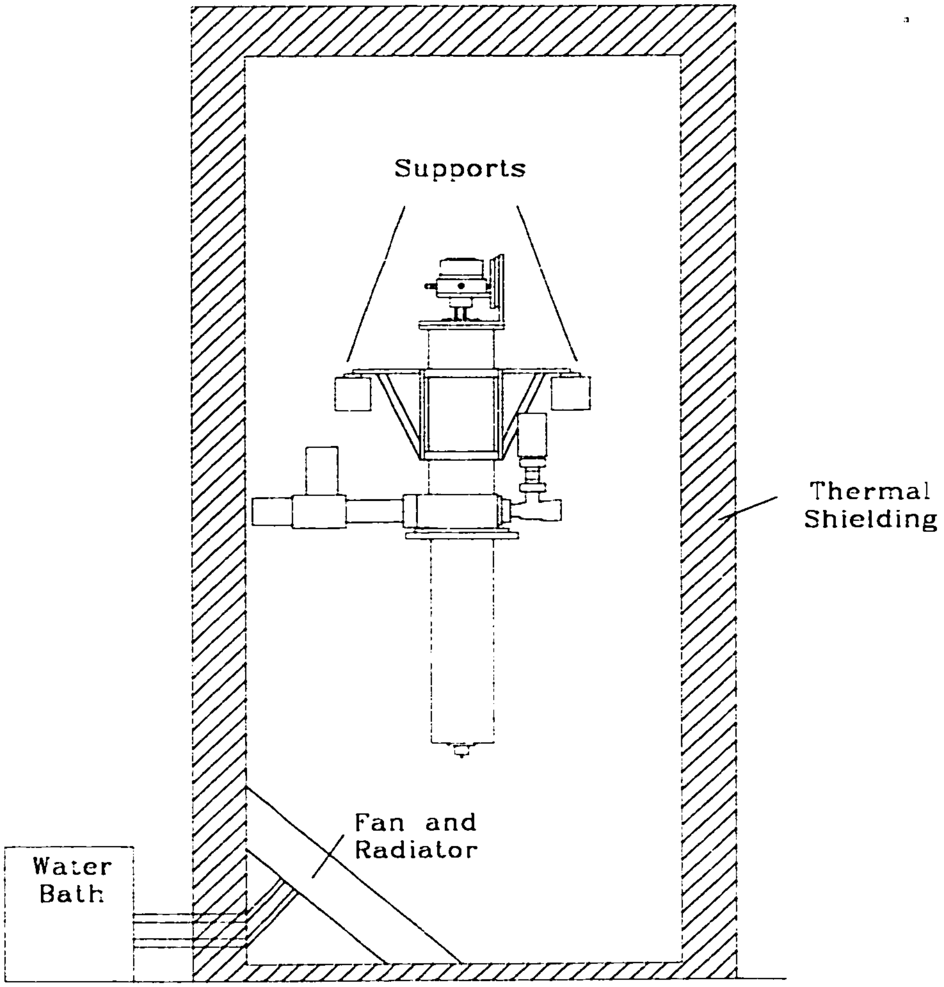

Figure 2.13: Diagram of the apparatus, thermal enclosure, and mounting system.

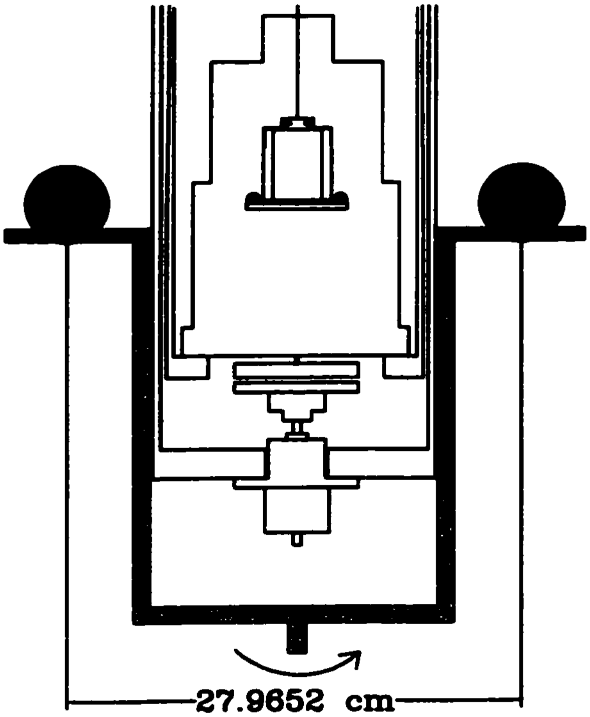

Figure 2.14: Schematic Diagram of the vacuum vessel with the external calibration turntable installed. The spheres used for the calibration are black, the turntable is gray.

Table 2.5: Sensors recorded by the data acquisition computer. *Refers to a sensor present only in Experiment II.

Sensor
Attractor Angle
Autocollimator Δ
Autocollimator Σ
Autocollimator Δ Quadrature
Autocollimator Σ Quadrature
Vacuum Chamber Pressure
Vertical Seismometer*
Horizontal Seismometer*
Temperatures (Multiplexed)

where V was the sensor value in physical units. The values of c_i were determined by producing a known change in the sensor values and measuring their response as recorded in ADU.

Data was taken at variable intervals, typically about once every 5-15 s. The data was stored on a floppy disk and the hard disk of the acquisition computer.

Chapter 3

ALIGNMENT AND POSITIONING

Because of the small distance scale associated with these experiments, very accurate alignment and positioning of the pendulum and attractor were required. This chapter describes the alignment and positioning processes.

3.1 Leveling the Pendulum Disk

3.1.1 Principle of the Technique

It is easy to see that the center of mass of a torsion balance must lie directly beneath the suspension point of a perfectly flexible fiber (neglecting the centripetal force of the rotating earth). In this case, "beneath" is defined by local vertical of the gravitational field in the laboratory. However, this does not require that the symmetry axis of the pendulum be parallel with local vertical, as shown in Figure 3.1. As we measured the torque produced around the fiber axis, it was desirable to align the pendulum ring perpendicular to local vertical and concentric to the torsion fiber (we kept the plane of the pendulum ring perpendicular to the vertical symmetry axis to within 0.2 mrad). This ensured that we measured the total torque about the symmetry axis and allowed us to obtain small pendulum-to-attractor spacings when the autocollimator light beam was on any of the pendulum mirrors.

To accomplish the leveling, we used the pendulum as one plate of a differential capacitor. The other two plates consisted of semi-circular copper pieces isolated by a thin gap. The pendulum was suspended above the plates with a vertical separation

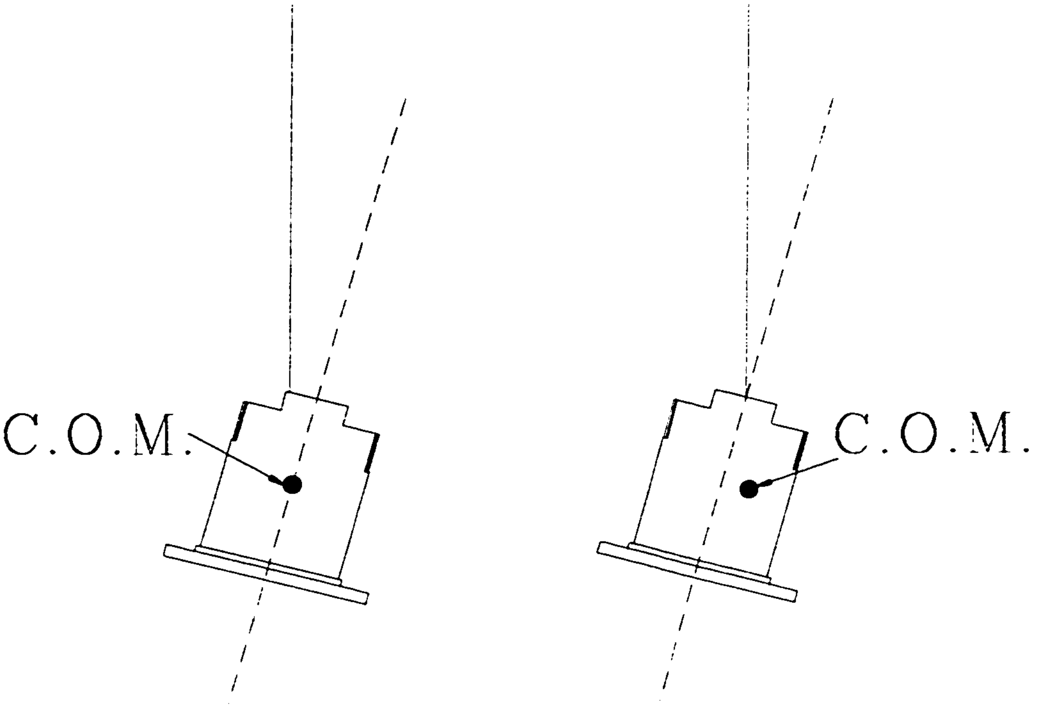

Figure 3.1: Two possible sources of pendulum tilt. The torsion fiber (parallel to local vertical) is shown as the solid line. On the left, the torsion fiber is not attached along the pendulum's symmetry axis (fine dotted line); whereas, on the right, the center of mass is misaligned with the symmetry axis.

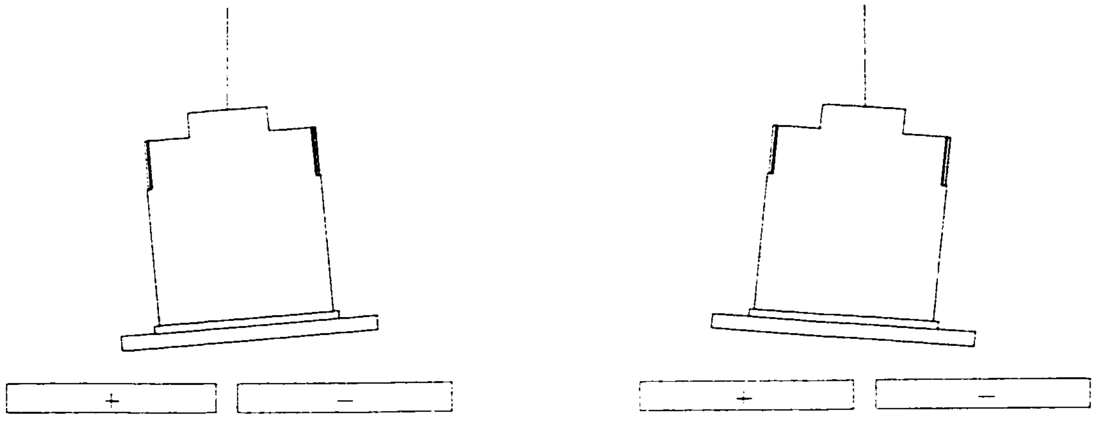

Figure 3.2: Schematic diagram of the leveling measurement. If the pendulum was tilted, a higher capacitance would have been registered by the "+" plate in the scenario on the left, and (as shown on the right) by the "−" plate after the upper fiber attachment was rotated by 180°.

of ∼ 1 mm and rotated at a uniform rate using the fiber positioner stage. If the pendulum disk were perfectly horizontal, the differential capacitance between the two sides would not change as the pendulum was rotated. However, if there was a tilt of the pendulum, the differential capacitance would vary periodically at the rotation frequency (see Figure 3.2). This 1ω signal was independent of any static tilt of the copper plates.

There were possible sources of a false signal in this measurement, however. If the fiber did not lie directly along the rotation axis of the stage, the center of the pendulum ring would move in a circle with respect to the copper plates and the "run-out" would have modulated the differential capacitance at the rotation frequency. Any periodic motion of the fiber support in the surrounding shroud could have produced a false effect as well. These modulations were not associated with the level of the pendulum and, therefore, needed to be eliminated. The next section describes our

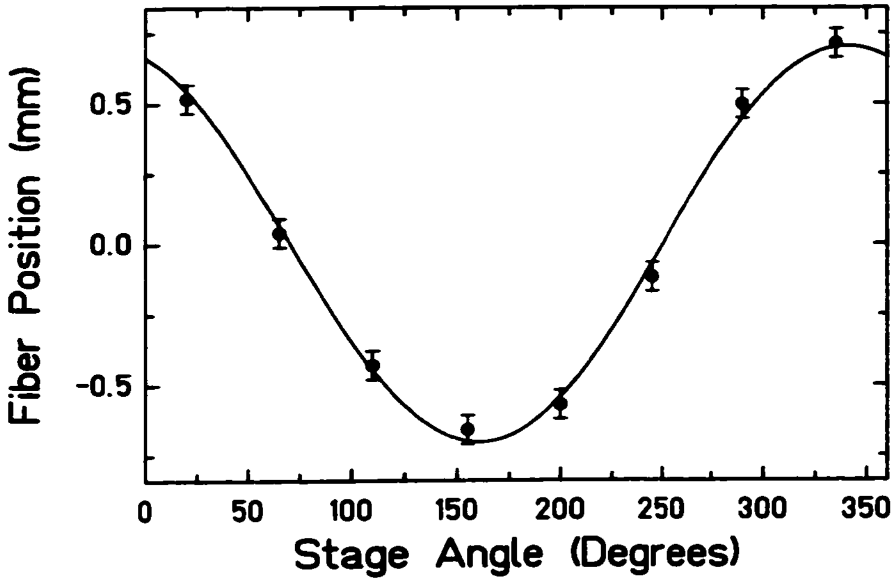

Figure 3.3: Measurements of the fiber position as a function of the upper rotation stage angle. The resulting fit yields a run-out of 0.71±0.03 mm.

effort to reduce the former of these spurious effects.

3.1.2 Correcting the Fiber Run-Out

We aligned the rotation axis with the fiber by moving the upper end of the fiber shaft so that its lower end, at the fiber attachment point, was positioned along the rotation axis (the shaft pivoted about the O-ring seal). Four positioning screws allowed adjustment of the shaft along two perpendicular axes. The fiber position was recorded optically with a theodolite.

We recorded eight fiber positions at evenly spaced intervals in one stage revolution. The resulting data were fit to a sinusoidal function, the amplitude of which was defined as the run-out. Figure 3.3 shows typical run-out data and the resulting best fit curve. We then reduced the run-out by adjusting the shaft screws. The process was iterative due to hysteresis in the adjusting process. The run-out amplitude was reduced to 74±23 μm (24±8 μm) for Experiment I (II). The effect of any residual run-out on the leveling is discussed in Section 3.1.3.

3.1.3 Differential Capacitance Measurement

We constructed a preamplifier that produced a bipolar voltage proportional to the differential capacitance. We recorded this voltage and the angle of the fiber positioner stage using our data acquisition computer. Figure 3.4 shows the voltage output for one revolution of the stage. The rotation period was 200 s, which was the period of the largest signal before adjustment. However, as the pendulum approached level, the modulation arising from each of the 10 holes passing over gap between the plates became the dominant harmonic component.

The pendulum was leveled by adjusting screws in the upper part of its frame to translate the center of mass and place the active ring in the horizontal plane. In Experiment I, the positioning was accomplished by turning screws that translated the fiber attachment point relative to the rest of the pendulum body. In the second experiment, small copper screws were driven along perpendicular axes to translate the center of mass (see Figure 2.2). The sensitivity of the adjustments was calculated by using precise models of the entire pendulum mass distribution and the known amount of screw translation per turn. For Experiment I (II), the pendulum plane was tilted by 8.85 mrad/turn (0.37 mrad/turn). Using one screw adjustment along each axis to calibrate the output voltage, we could converge on the desired orientation.

Each adjustment could change both the amplitude and phase of the observed differential capacitance modulation. Figure 3.4 shows the initial and final (level) signals for Experiment I; we also see the 10ω modulation arising from the holes. The final 1ω differential capacitance signal corresponded to a misalignment of 0.03±0.01 mrad

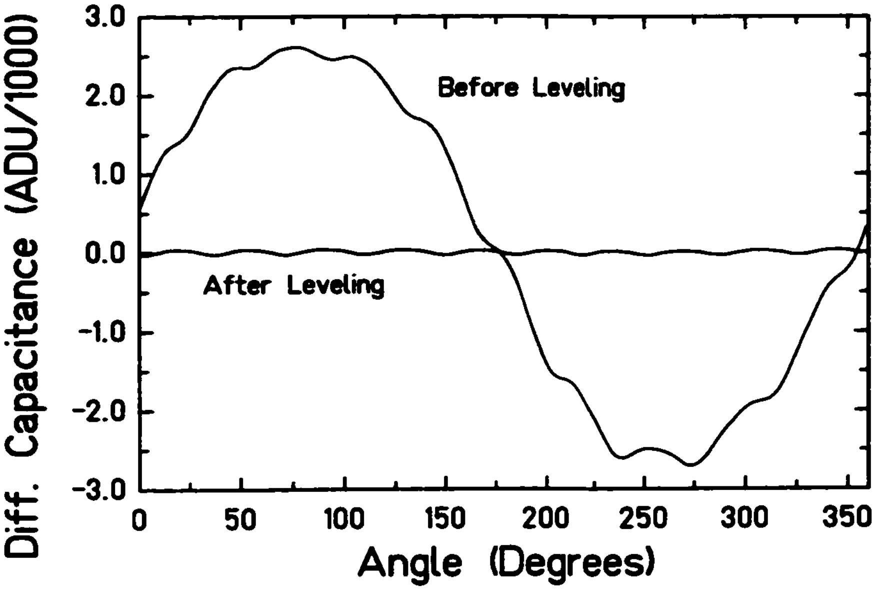

Figure 3.4: Differential capacitance for one revolution of the pendulum above the copper plates before and after leveling. The tilt signal occurs at 1ω; the 10ω ripple results from the ten holes passing over the gap between the plates of the capacitor. The 1ω amplitudes correspond to pendulum tilts of 7.52±0.06 mrad and 0.03±0.01 mrad for before and after leveling, respectively.

(0.12±0.01 mrad) of the pendulum plane to the horizontal.

The effect of any stray signal induced by the fiber run-out or stage and shaft motion was checked in the following manner. First, the pendulum was "parked" on the capacitor plates. The rotation stage was then turned through ~3 revolutions. Next, the pendulum was raised to the original height and left to unwind freely. With nothing but the pendulum's tilt to influence the differential capacitance, any difference in the peak-to-peak amplitude between the freely unwinding case versus that when the stage was rotating must have been due to a false effect. The observed difference in amplitude introduced an additional uncertainty of ±0.11 mrad (±0.01 mrad). Thus, we determined the tilt of the pendulum ring to be 0.03±0.11 mrad (0.12±0.01 mrad).

3.2 Aligning the Rotating Attractor

Alignment of the rotating attractor relative to the pendulum was crucial for obtaining the minimum possible pendulum-to-attractor separation. Precise alignment also ensured the calculation accurately described the properties of the attractor.

3.2.1 Reducing Attractor Rotation Imperfections

Any imperfections in the rotation of the attractor were not included in our calculation of the predicted harmonic torque components; therefore, we undertook efforts to reduce these effects to negligible levels. The attractor disks were very flat (±5 μm), but the holder and drive mechanism were less precise. We measured the wobble and vertical rumble (see Figure 3.5) with precise mechanical indicators. We found no measurable rumble within the ±3 μm measuring error. The wobble was adjusted by adding thin shims between the attractor and holder. The wobble amplitude was reduced to <0.2 mrad (0.05 mrad) by this method for Experiment I (II).

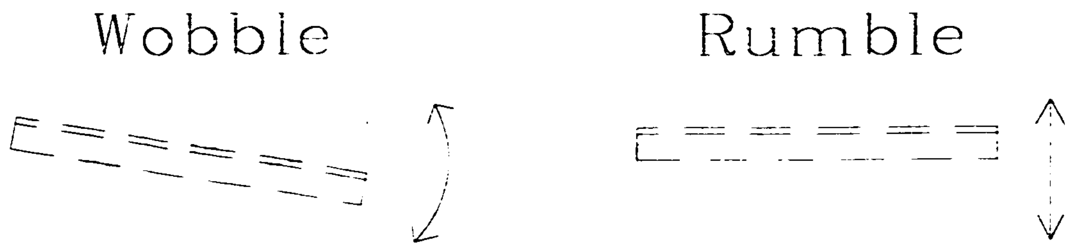

Figure 3.5: Depiction of the possible attractor rotation imperfections. Mechanical methods were used to reduce the wobble. Vertical rumble was too small to measure with our instruments.

3.2.2 Positioning the Attractor Relative to the Conducting Membrane

The attractor was positioned relative to the conducting membrane before the assembly was installed in the vacuum vessel. The bearing that supported the whole attractor rested on three leveling screws. We temporarily replaced the conducting membrane with a lapped plate containing a hole. A depth micrometer passed through this hole measured the distance to the attractor. By measuring the distance above each leveling screw and making iterative tilt adjustments, the attractor was made parallel to the membrane to within 0.1 mrad. The distance between the membrane and the upper surface of the attractor was 48±3 μm (54±3 μm) for Experiment I (II). The mechanical distance measurement was averaged with a capacitive measurement to obtain this value. Using the measured attractor dimensions, the capacitance value, 1.33±0.01 pF (1.19±0.01 pF), corresponded to a separation of 47±1 μm (51±1 μm). The mechanically measured distance was 48±3 μm (57±3 μm).

3.3 Aligning the Pendulum and Conducting Membrane

We measured the parallelism of the pendulum ring and the conducting membrane using a capacitive technique. The capacitance was measured by the low-noise, high-

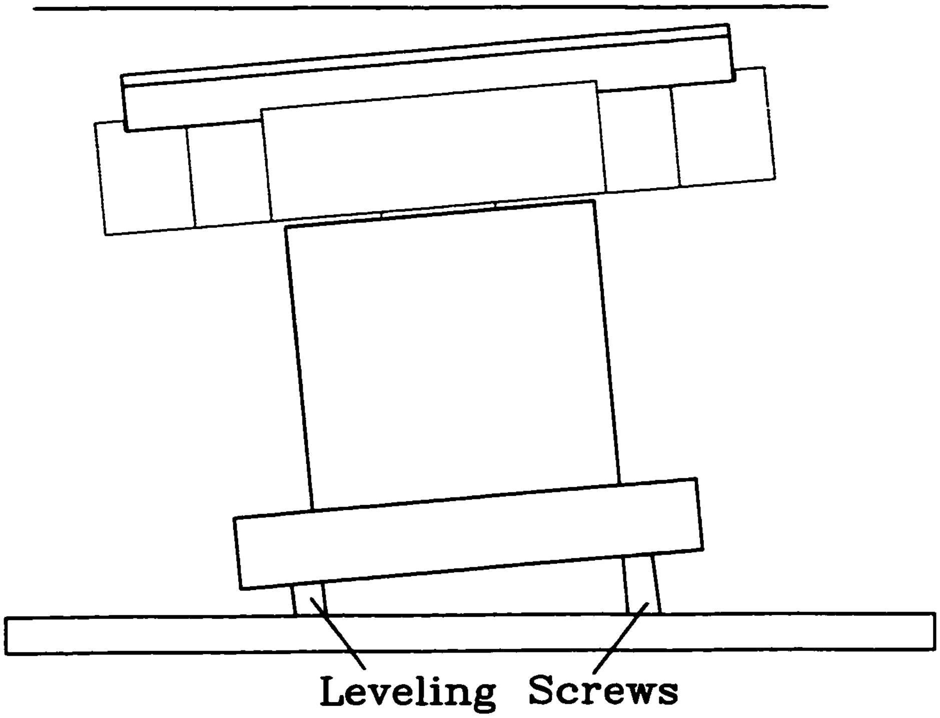

Figure 3.6: Leveling screws positioned the attractor relative to the conducting membrane. The attractor-to-membrane separation was measured both mechanically and capacitively.

sensitivity LCR meter (Stanford Research Systems model SR720) normally used to determine the pendulum-to-membrane separation (see Section 3.5). We tilted the entire apparatus and measured the pendulum-to-membrane capacitance. In the very good approximation that the tilting did not change the horizontal orientation of the pendulum, the minimum value of the capacitance occurred when the pendulum and membrane were parallel.

The vacuum vessel tilt was measured by the electronic tilt sensors described in Section 2.7.1. Capacitance values were read for several values of the tilt along two axes separated by 120°. The resulting points were fitted with a parabolic function. The values and best fit line for one scan are shown in Figure 3.7. The tilt of the apparatus was then adjusted to the capacitance minimum for each axis. The error on this procedure was ±18 μrad, determined by the accuracy of the tilt adjustment (±6 μrad) and the error on the fitted value of the minimum (±17 μrad).

3.4 Centering the Pendulum in the Horizontal Plane

The horizontal alignment of the pendulum ring and attractor disks (coaxiality) was measured gravitationally. The torque on the pendulum was a symmetric function about the alignment point. This was confirmed by detailed calculations (see Figure 3.8 and Chapter 5). We took data at offset points along the X and Y axes and used these points as part of the complete data set. The analysis left the alignment points, x_0 and y_0, as completely free parameters. The fit was able to resolve the true alignment to ±10 μm. Since the torque varied much less than our statistical noise over an offset range of ±100 μm, this alignment was of sufficient precision.

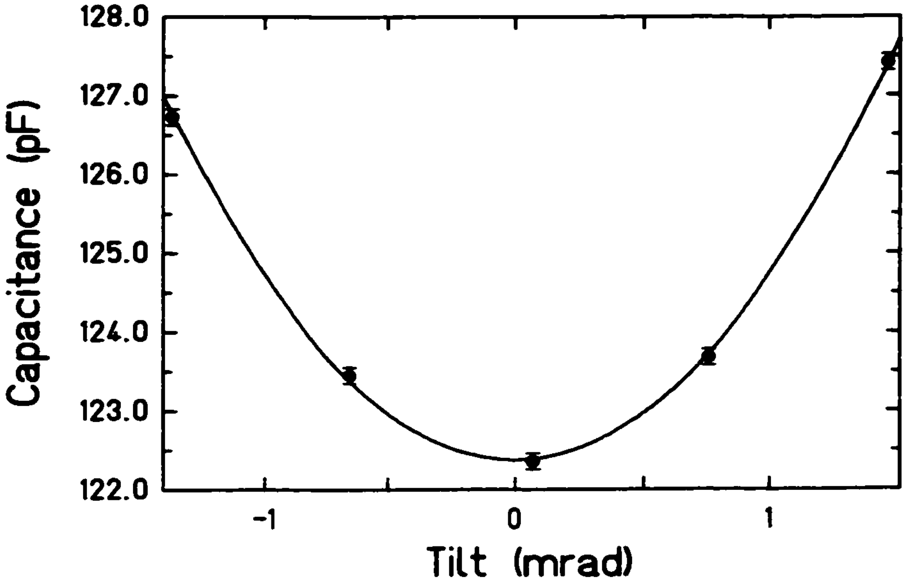

Figure 3.7: Data and parabolic fit for the pendulum-to-membrane alignment along one tilt axis. The capacitance is minimum when the pendulum and membrane are parallel. The error on the leveling, ±18 μrad, was determined by the error on the fitted minimum position and the accuracy to which the tilt could be adjusted.

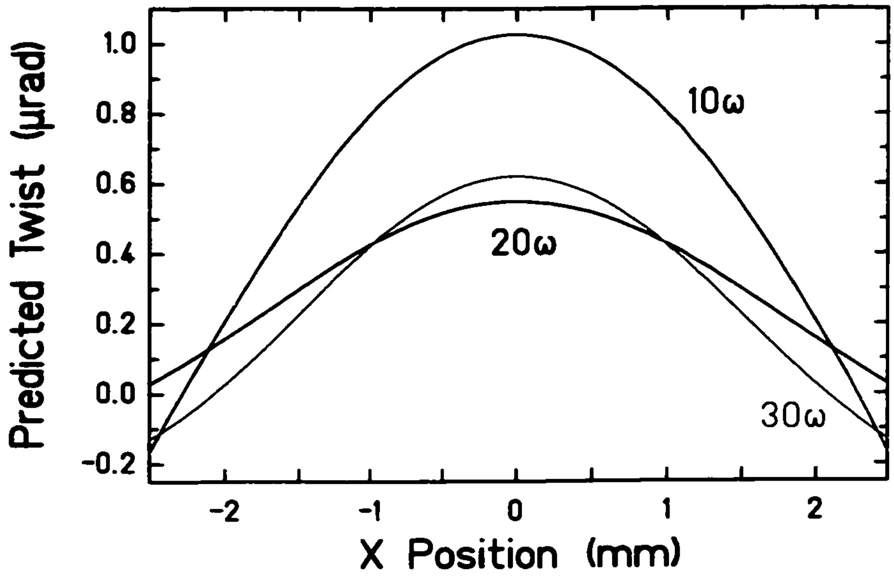

Figure 3.8: Predicted variation of the harmonic components of the torque with horizontal offset for a pendulum-to-attractor separation of 0.5 mm in Experiment I. All signals are symmetric about the alignment point (X=0).

3.5 Determining the Vertical Separation Between the Pendulum and Membrane

Knowledge of the pendulum-to-membrane separation was crucial in these experiments. The electronic micrometers were of sufficient accuracy (after accounting for the scale factors described in Section 2.3.5) and reproducibility to gauge the *relative* X, Y, and Z positions. To extract the absolute membrane position, as read by the Z-micrometer, we measured the capacitance as a function of separation (called a "z-scan"), and fitted the resulting points to the model described below.

3.5.1 Model Capacitance Function

The model we used was effectively that of a plane electrode parallel to an infinite plate and included a first-order edge correction. The form of the fitting function comes from [30] and is given by

$$C = \varepsilon_\circ \left[\frac{S}{(z - z_\circ)} + \frac{L}{\pi} \log \left(\frac{\sqrt{S}}{2\,(z - z_\circ)} \right) \right] + C_s, \tag{3.1}$$

where S is the effective area of the pendulum ring, z is the reading of the Z-micrometer, L is the effective total of all edge lengths on the pendulum ring, C_s is any stray capacitance independent of z, and $z_\circ$ is the Z-micrometer reading at vanishing pendulum-to-membrane separation. We expected that $S \approx \pi(R_o^2 - R_i^2 - 10R_h^2)$ and $L \approx 2\pi(R_o + R_i + 10R_h)$, where R_o is the outer radius of the pendulum ring, R_i its inner radius, and R_h is the radius of the holes.

3.5.2 Bounce

Due to the relatively long, thin torsion fiber, seismic vibrations excited its vertical "bounce" mode. Ultimately, this motion was a limiting factor in the minimum achievable separation.

We needed to account for this motion when determining the membrane position. The bounce amplitude was directly measurable as follows. The pendulum was raised until the mirror intersected only half of the autocollimator light beam. Thus, any vertical motion created a change in the total amount of light returned to the detector. By changing the height a known distance and looking at the corresponding change in the amount of returned light, we determined that

$$\frac{\Delta L}{\Delta z} = 220\ \mathrm{mV/mm}, \tag{3.2}$$

where ΔL and Δz are the change in returned light (as measured by a lock-in amplifier) and height, respectively. By monitoring the 11.5 Hz bounce oscillation of ΔL on a spectrum analyzer, we found the average bounce amplitude to be 13 μm, with a maximum value of 36 μm over the course of one day.

Bounce Correction

The act of moving the vertical stage during a z-scan excited the bounce mode. We modeled the bounce as a sinusoidal modulation of the pendulum-to-membrane separation. If the bounce had amplitude δ, equation 3.1 is modified to be

$$\begin{aligned} C \; = \; & \frac{\varepsilon_o S}{(z - z_o)\sqrt{1 - \left(\frac{\delta}{(z-z_o)}\right)^2}} \\ & + \frac{\varepsilon_o L}{\pi}\left[\log\left(\frac{\sqrt{S}}{(z - z_o)}\right) - \log\left(1 + \sqrt{1 - \left(\frac{\delta}{(z - z_o)}\right)^2}\right)\right] + C_s. \end{aligned} \tag{3.3}$$

We had the ability to vary δ in the fit. The extracted membrane position was independent of δ for values between 10 and 40 μm, the typical range of observed bounce amplitudes.

Table 3.1: Comparison of the expected and fitted parameters of Equation 3.3 for the z-scan of Figure 3.9 in Experiment I. The difference between the fitted effective area and circumference and the actual area and circumference of the ring reflects the approximate nature of the first-order fringing correction. The difference is not troubling because the location of the pole was well determined by the data.

Parameter	Expected Value	Fitted Value
S	14.85±0.20 cm^2	15.89±0.48 cm^2
L	64.43±0.19 cm	57.66±8.30 cm
z_0	N/A	0.978±0.003 mm
C_s	N/A	4.57±1.03 pF
δ	10-40 μm	15 μm (fixed)

3.5.3 Data and Results

One z-scan typically contained about 25 different vertical separations between $\sim 0.1 - 3$ mm (larger vertical separations gave no information about the membrane position). The data points and best fit line for one z-scan are shown in Figure 3.9. The fitted values of the parameters in Equation 3.3 are compared to their best estimates in Table 3.1. The error on the extracted membrane position from the fit was typically ±3 μm.

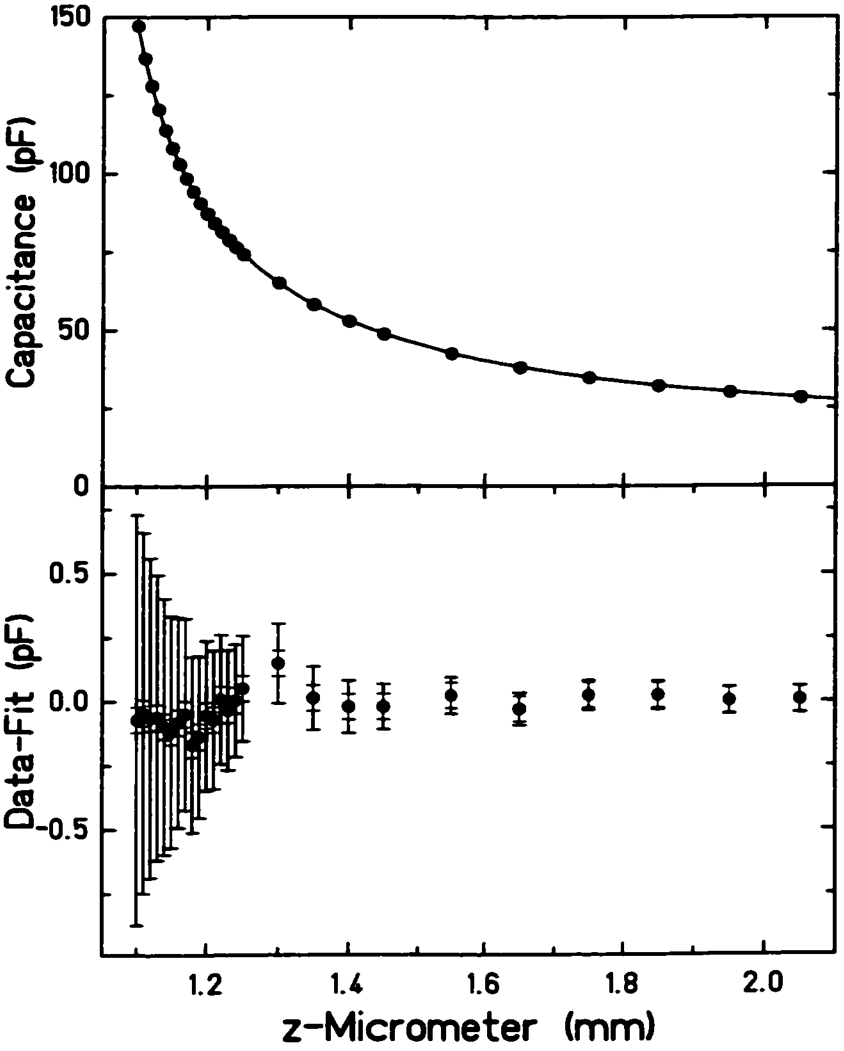

Figure 3.9: Z-scan data and residuals from Experiment I. The fit indicated the pendulum would touch the membrane at a Z-micrometer reading of 0.978±0.003 mm. The lower panel displays the fit residuals. The smaller set of error bars on the residuals represents the uncertainty in the capacitance values alone, while the larger ones include the effect of the uncertainty of the stage position (±1 μm).

Chapter 4

SYSTEMATIC ERRORS

Control of systematic effects is crucial when measuring the intrinsically weak properties of gravity. The great advantage of our technique over previous experiments was the separation of the attractor rotation frequency from the signal frequency. Many systematic effects varied once per attractor revolution. Since our signals of interest occured at frequencies of 10ω and higher, many systematic effects were reduced or completely eliminated. This chapter describes possible sources of systematic errors and their effect on our results. We classified the systematic errors into two categories: "false" effects and instrumental uncertainties.

4.1 False Effects

A false effect was any non-gravitational effect that would have produced a (real or apparent) coherent torque on the pendulum at our signal frequency. These effects included modulations of the apparatus temperature, apparatus tilt, or magnetic field at the signal frequency. Electrostatic or stray gravitational couplings could have polluted our signals as well. In general, we tested the sensitivity of our apparatus to individual false effects by exaggerating the driving force and measuring the pendulum's response. We report the systematic effect on the fundamental 10ω signal. Unless otherwise noted, the effect on the higher harmonics was negligible.

4.1.1 Thermal

Modulation of the Average Temperature

We measured the temperature-twist coupling by subjecting the apparatus to a known time-varying (1ω) temperature change and measuring the pendulum's response. We modulated the temperature at this low frequency to allow thermal equilibration of the large thermal mass of the apparatus. We used the three sensors attached to the vacuum vessel to quantify the temperature change. The radiator water bath had a 1ω temperature amplitude of 910±1 mK, while the average of the three sensors recorded a 123±0.5 mK 1ω temperature variation of the apparatus. The pendulum's temperature induced twist amplitude was 1.17±0.07 μrad, corresponding to a 9.51±0.57 μrad/K temperature feed through. The variations in the temperature at the fundamental 10ω frequency were analyzed and found to be ≤ 0.1 mK during normal data taking. Thus, the systematic error associated with temperature modulations was $\lesssim$1 nrad.

Temperature Gradients

If the attractor was at a slightly higher temperature than its surroundings, radiometer effects could conceivably have produced spurious signals. Molecules streaming from the attractor could have differentially heated the membrane. The molecules emitted from these rotating "hot spots" could have caused a torque on the pendulum at our signal frequency.

We can estimate the size of this effect by determining the characteristic length for thermal fluctuations in the membrane. The relationship for the heat propagation due to a time-varying temperature fluctuation $\phi(\vec{r},\ t)$ is

$$\frac{k}{\rho C_p}\nabla^2\phi(\vec{r},\ t) = \frac{\partial\phi(\vec{r},\ t)}{\partial t}, \tag{4.1}$$

where $k = 401$ W/(m·K) is the thermal conductivity of copper, $\rho \simeq 8900$ kg/m^3

is its density, and $C_P = 385$ J/(kg·K) is its heat capacity at constant pressure. We assume cylindrical symmetry and a sinusoidally varying temperature source along the z-axis of amplitude ϕ_o. If we assume $\phi(\vec{r},\, t) = \phi_o\phi(r)\cos(\omega t) = Re\,[\phi_o\phi(r)e^{i\omega t}]$, with $D = k/(\rho C_P)$ Equation 4.1 becomes

$$\frac{\partial^2}{\partial r^2}\phi(r) + \frac{1}{r}\frac{\partial}{\partial r}\phi(r) + \left(\frac{-i\omega}{D}\right)\phi(r) = 0. \tag{4.2}$$

The solution of this radial equation is the Bessel function $J_o\left((i-1)\sqrt{\frac{\omega}{2D}}\,r\right)$, so that the total solution is

$$\phi(\vec{r},\, t) = \mathrm{Re}\left[\phi_o\, J_o\left((i-1)\sqrt{\frac{\omega}{2D}}\,r\right)e^{i\omega t}\right]. \tag{4.3}$$

Since the characteristic length associated with fluctuations at this frequency, $\sqrt{\frac{2D}{\omega}} \approx$ 16 cm is much larger than the ~1 cm spacing between the holes, we expected a negligible temperature difference. In fact, at a distance of 1 cm from the "hot spot," the temperature of the membrane was within a part in 10^{-6} of the temperature of the "hot spot." So, according to this estimate, there was a negligible 10-fold temperature asymmetry in the membrane.

We checked for a temperature gradient effect by deliberately heating the attractor with two 5 W resistors attached to the attractor drive motor. Passing 0.6 A in series through the resistors increased the temperature of the motor mount by 4.8 °C. This was a five-fold increase over the temperature rise associated with turning on the motor. We compared the observed twist signals in this configuration to that of a normal, "cool" run. We found the 10ω signal unchanged by 17 ± 11 nrad out of a total signal of 1.435 μrad, consistent at the 2σ level with the predicted negligible size of this effect. Thermal expansion from the heating associated with turning on the motor could have affected the attractor-to-membrane distance. The attractor/membrane capacitance was unchanged within ±0.01 pF out of 1.33 pF when the motor was turned on, corresponding to a distance change of < 1 μm for Experiment I. We therefore assumed no systematic error associated with the thermal gradient produced by the motor.

4.1.2 Tilt

There are two principal effects we may attribute to tilt. The first concerns a modulation of the apparatus tilt at the signal frequency. Since a tilt of the fiber attachment produces a twist in the pendulum, any tilt at the signal frequency can cause a false signal.

We tilted the vacuum vessel by 1.02 ± 0.01 mrad and observed the pendulum equilibrium position to change by 16 ± 2 μrad, corresponding to a feed through of 0.016 ± 0.002. We analyzed the tilt recorded by the AGI's at the signal frequency during each data run. We found no resolved tilt signal periodic at 10ω. The value of the observed tilt modulation, ≤ 4.0 nrad, corresponded to a systematic tilt induced signal at 10ω of ≤ 0.06 nrad.

The second tilt effect arises if there is a static tilt between the pendulum and attractor. Our calculation of the predicted Newtonian and Yukawa interactions assumed that the plates were perfectly parallel. The tilt between the pendulum and attractor was < 0.2 mrad during normal data taking. We used the calculated gravitational signal to estimate the effect of a tilt. We denote the 10ω torque from an individual attractor hole at a pendulum-to-attractor separation of $z_\circ$ as $T_{10}(z_\circ)/10$. A tilt of size ψ between the pendulum and attractor changes the effective separation for each hole. If we choose the tilt axis to bisect two holes at a given instant in time, we may approximate the torque in the tilted configuration by

$$T_{10}^{tilt} \approx \sum_{j=0}^{9} \frac{T_{10}(z_\circ + r\sin(\psi)\sin((2j+1)\pi/10))}{10}, \tag{4.4}$$

where r is the radius of the holes from the rotation axis. We found the maximum difference for Experiment I (II) was

$$|T_{10}(z_\circ) - T_{10}^{tilt}| = 0.04 \text{ nrad } (0.05 \text{ nrad}) \tag{4.5}$$

for $\psi = 0.2$ mrad. To check the calculation we purposefully added a 1 mrad tilt for certain runs. We found the 10ω twist unchanged at a level of 21 ± 11 nrad out of a total signal of 8.459 μrad, confirming the calculation at the 2σ level. We adopted the values from Equation 4.5 as the systematic errors for this tilt effect.

4.1.3 Magnetic

A magnetization of the attractor could have interacted with a magnetic moment on the pendulum to produce a periodic torque. We measured the magnetic moment of the pendulum by applying a time-varying external magnetic field and observing its response. A coil placed outside the thermal shielding produced a horizontal 6.3 mG field at the pendulum location. We modulated this field at 10ω for both experiments and saw an induced 335 ± 79 nrad (252 ± 25 nrad for Experiment II) twist. By placing the coil at two locations rotated by a relative angle of 45° (a simpler 90° rotation was prohibited by the laboratory conditions), we found the pendulum to have a magnetic feed through of 57 nrad/mG (38 nrad/mG) for Experiment I (II). The amplitude of 10ω magnetic field variations at the site of the pendulum under normal operating conditions, as measured by a flux gate magnetometer, was ≤ 0.6 μG. Hence, the error associated with a magnetic coupling was ± 0.03 nrad (± 0.02 nrad), much smaller than the typical 8 nrad statistical error per data run.

4.1.4 Electrostatic

Electrostatic interactions between the pendulum and attractor were essentially eliminated by the presence of the conducting membrane. However, electrostatic potential wells on the surface of the membrane could have interacted with patch charges on the pendulum to change the properties of the resonance. These changes would have affected the corrections applied to the observed twist when extracting the torque (see Section 6.1.6), and could have wrongly biased the extracted twist signals.

We determined the effect of any such local electrostatic interaction by measuring the period of the free torsional oscillation for each run. The data for each run was fitted to extract the period. The presence of an electrostatic potential would have then appeared as a separation dependence of the torsion period. Figure 4.1 shows the torsion period as a function of separation for Experiment I. A small systematic variation in the values of the period seems to occur only at very close separations. The measured values were used in the data analysis. It should also be noted that *any* effect that changed the oscillator properties, such as residual gas damping, was eliminated by the period correction.

4.1.5 Gravitational Background

Our predictions of the Newtonian and Yukawa torques assumed that the entire torque was due to the holes in the pendulum ring and attractor disk. However, there could have been residual gravitational coupling between the mass distributions of the pendulum frame and attractor drive mechanism that could have produced spurious signals at 10ω, 20ω, etc. We designed the frame and drive mechanism to suppress any such couplings. The pendulum frame had two-fold (four-fold) rotational symmetry and the attractor drive was 3-fold symmetric. We therefore expected no torque from these components at any harmonic of interest.

We measured any residual torque at the signal frequencies in the following manner. We removed the attractor disks from their holder. Any 10ω torque in this configuration would have been a spurious effect. We found no resolved effect. We then replaced

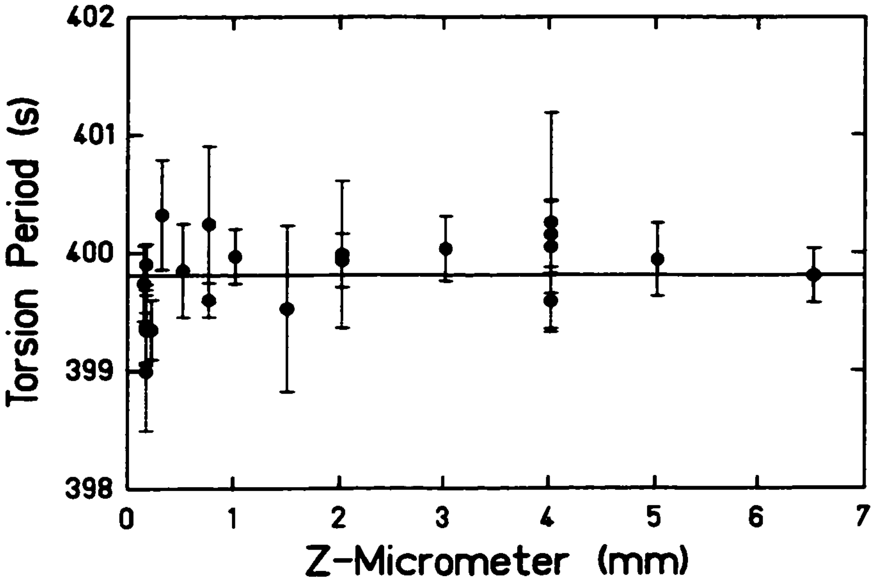

Figure 4.1: The torsion period as a function of the pendulum-to-membrane separation in Experiment I. The horizontal line depicts the mean of the scatter of the values. We see a small downward trend at close separations. The data analysis corrected for this effect.

Table 4.1: Observed residual harmonic components of the twist. "Frame on Attractor" refers to the configuration in which the pendulum ring was removed and the torque on the frame measured, while "Pendulum on Drive" refers to the torque on the complete pendulum produced by the attractor drive mechanism alone.

Expt.	Configuration	10ω (nrad)	20ω (nrad)	30ω (nrad)
I	Frame on Attractor	6.4 ± 6.7	1.0 ± 2.9	4.3 ± 8.2
I	Pendulum on Drive	19.6 ± 11.4	8.2 ± 9.6	3.4 ± 9.9
II	Frame on Attractor	33.1 ± 68.0	78.7 ± 83.4	N/A
II	Pendulum on Drive	3.5 ± 5.0	1.6 ± 3.4	N/A

the attractor in its original position and removed the pendulum ring from its frame. Any torque at our signal frequency in this configuration was due to imperfections of the frame. We also found no signal in this configuration. Table 4.1 summarizes the results. Because we did not expect (and did not observe) any gravitational background at our signal frequencies, we did not assign a systematic error for this effect.

4.1.6 Attractor Speed Dependence

We checked the validity of our analysis procedures, specifically the frequency dependent corrections (described in Section 6.1.6), by comparing data taken with different attractor rotation rates. These corrections depended on the measured values of the free oscillation period and amplitude decay time, attractor rotation rate, and electronic time constants. We used the measured values and uncertainties of these parameters when applying the corrections to each data run, and therefore expected no systematic variation of the extracted torque amplitudes with attractor speed. In Experiment I where the normal rotation period was $\tau_{att} = 17\tau_{\circ}$, we also took data with attractor periods of $7\tau_{\circ}$ and $43\tau_{\circ}$. The results are summarized in Table 4.2. We

Table 4.2: Comparison of the harmonic twist signals at different attractor rotation speeds in Experiment I. We saw no discernable systematic variation.

Attractor Speed	10ω (nrad)	20ω (nrad)	30ω (nrad)
$7\tau_o$	863.6 ± 10.7	421.5 ± 31.3	439.4 ± 38.8
$43\tau_o$	869.9 ± 9.9	428.5 ± 5.2	458.7 ± 13.9
Change	6.3 ± 14.6	7.0 ± 31.7	19.3 ± 41.2

Table 4.3: Contribution to the measured twist error from the false effects for which we assigned an uncertainty.

Effect	10ω Twist Error (nrad)
Temperature Modulation	$\lesssim 1$
Apparatus Tilt	≤ 0.06
Relative Tilt	≤ 0.05
Magnetic	≤ 0.03

found no measurable discrepancy, and therefore assigned no error from these corrections (except for that introduced from the measured errors of the period, decay time, etc).

4.1.7 False Effect Error Budget

Table 4.3 summarizes the twist produced by the false effects for which we assigned an uncertainty. We see that the sum of these effects is far smaller than our statistical noise, which was ~ 8 nrad per data point for a given value of the pendulum-to-attractor separation and offset.

4.2 Uncertainties in the Instrumental Parameters

Errors in the measurements of the instrumental parameters, such as the pendulum-to-attractor separation, calibration of the torque scale, and pendulum and attractor geometries could have biased our results. We measured the parameters and used the values and errors we obtained as constrained parameters in the analysis. In particular, the parameters were C (the overall torque-scale factor), R_1 (the relative torque-scale factor for the lower attractor disk holes), R_2 (the relative torque-scale factor for the upper disk out-of-phase holes in Experiment II), z_o (the vertical position reading at vanishing pendulum-to-attractor separation), δz (a gap between the upper and lower attractor disks), and ζ (the vertical position reading at vanishing pendulum-to-upper disk separation in Experiment I). Since the calculated torques (described in Chapter 5) were based on the central values of the measured masses of the holes, the ratios R_1 and R_2 were expected to be unity with uncertainties determined by the uncertainties in the measured hole masses.

4.2.1 Torque-Scale Calibration

Three methods were used to calibrate of the torque scale. The gravitational technique was by far the most sensitive and precise; whereas, the other methods yielded complementary information.

The torque on the pendulum was inferred from the twist angle, the relationship being

$$T = \kappa\theta, \tag{4.6}$$

where θ was the pendulum twist corrected for inertia and electronic averaging, and κ the torsional spring constant of the fiber. Thus, it was necessary to measure the angular deflection scale as well as the spring constant (or their product, as in the gravitational calibration) to determine the torque scale.

The calibration of the angular deflection scale involved converting the autocollimator Δ and Σ signals to the raw twist angle,

$$\theta_{raw} = c_0 + c_1\left(\frac{\Delta}{\Sigma}\right) + c_2\left(\frac{\Delta}{\Sigma}\right)^2 , \tag{4.7}$$

where c_i are the desired calibration coefficients.

The torsional spring constant, κ, was determined from the relationship $\kappa = I\omega_o^2$, where I is the rotational inertia of the pendulum and ω_o its resonant angular frequency. The measured value of $\omega_o = 15.720 \pm 0.002$ mrad/s (for Experiment I) and the calculated value $I = 128 \pm 1$ g-cm^2 yielded $\kappa = 0.0317 \pm 0.0002$ erg/rad. The value of I was calculated with a program that used a detailed model of the pendulum based on the measured dimensions and masses of the pieces. The values $\omega_o = 13.454 \pm 0.002$ mrad/s and $I = 175 \pm 1$ g-cm^2 from Experiment II yielded an identical result (we expected κ to be unchanged because the same torsion fiber was used for both experiments).

Detector Scan

The angular deflection scale was calibrated by translating the autocollimator laser beam across the detector, simulating a rotation of the pendulum. The beam was reflected from a corner mirror and the detector was then translated by a stage along its sensitive axis. Assuming the focal length of the autocollimator to be exactly 30 cm (the nominal value specified by the manufacturer of the lens), we determined $c_1 = 1.322 \pm 0.001$ mrad and $c_2 = -0.055 \pm 0.004$ mrad. However, these values served only as a starting point because this measurement was subject to uncertainties concerning its relationship to the real experimental setup, i.e., properties of the optical system actually used in the experiment.

Dynamic Calibration

In Experiment I we did not use the gravitational calibration; therefore, we used the fiber positioner rotation stage to routinely calibrate the angular deflection scale. Energy was first taken out of the pendulum's torsional mode so that it had a very small amplitude, typically ~5 μrad. The fiber positioner stage was then rotated by a known amount, typically 349 μrad. The pendulum's observed change in amplitude (evaluated using $c_1 = 1.322$ mrad and $c_2 = -0.055$ mrad) was then compared to the expected change to extract the calibration coefficients. Figure 4.2 shows the data from one such calibration. This test was dominated by the ± 8.5 μrad (2.5%) uncertainty in the rotation stage position (half of the minimum angular step size and resolution of the encoder). Thus, for Experiment I, we had a large error associated with the overall scale factor. The results of this calibration for each run in Experiment I are shown in Figure 4.3. The fitted (average) values of $c_1 = 1.358 \pm 0.005$ and $c_2 = -0.063 \pm 0.004$ corresponded to a torque scale factor of $C = 1.027 \pm 0.025$ (including the 2.5% stage uncertainty) relative to the assumed values.

Dynamic calibrations were also used to determine the free oscillation period, τ_o, and the exponential amplitude damping time, τ_d (used in the inertial corrections described in Section 6.1.6) for both experiments.

Gravitational Calibration

In Experiment II, we produced a known gravitational torque on the pendulum to precisely determine the $\kappa\,\theta$ product. Two aluminum, 0.7345±0.0001 g, 7.938±0.003-mm-diameter spheres were placed in diametrically opposed holes on the pendulum ring. This produced known q_{l2} gravitational multipole moments, where l is the multipole order. At the same time, two brass, 5.08±0.02-cm-diameter, 515.4326±0.0003 g spheres were placed on the external calibration turntable (see Section 2.9). These

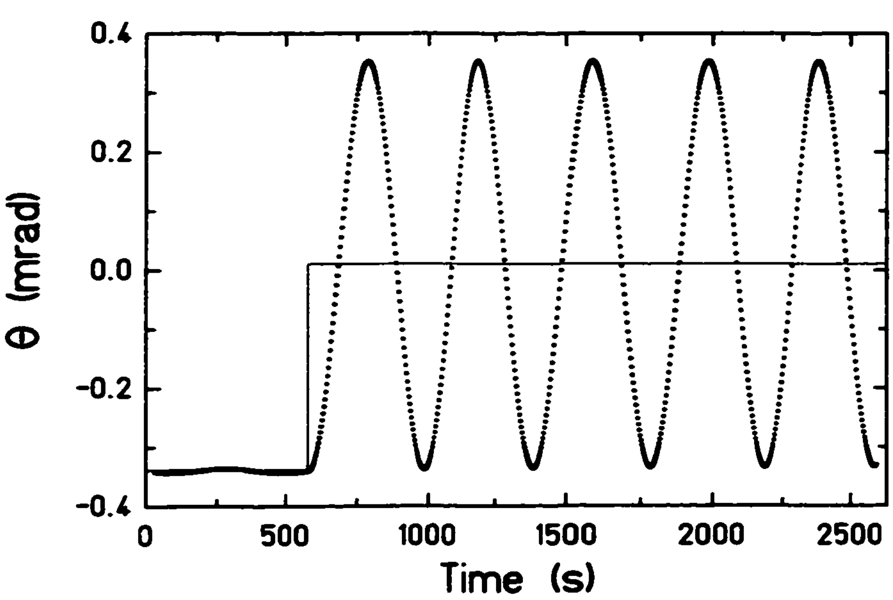

Figure 4.2: Dynamic calibration data. At t=580 s, the upper rotation stage changed the equilibrium position by 0.349 mrad. The solid line depicts the equilibrium position as a function of time.

spheres produced known Q_{l2} multipole fields. As the turntable was rotated at a frequency ω_c, it produced a $2\omega_c$ torque on the pendulum given by (see [28] pp. 11)

$$T_{tot} = 2\frac{8\pi G}{5}\sum_{l=2}^{8}\mathrm{Im}(q_{l2}\,Q_{l2}\,e^{2i\omega_c t}) + T_{stray} = T_{calc} + T_{stray}, \tag{4.8}$$

where T_{stray} was any residual $2\omega_c$ torque on the pendulum. The spheres produced a negligible torque for $l > 8$. The torque T_{calc} was calculated from the measured sphere properties to be $T_{calc} = (4.010 \pm 0.001) \times 10^{-7}$ dyne-cm. Figure 4.4 shows data for 3 revolutions of the calibration turntable. We clearly see the six characteristic oscillations of the $2\omega_c$ torque.

The torque prediction T_{calc} assumes that the rotation axis of the external turntable and the fiber are coaxial, and that the sphere centers aligned vertically. As this was not necessarily the case, we used multipole translation theorems to interpret our data

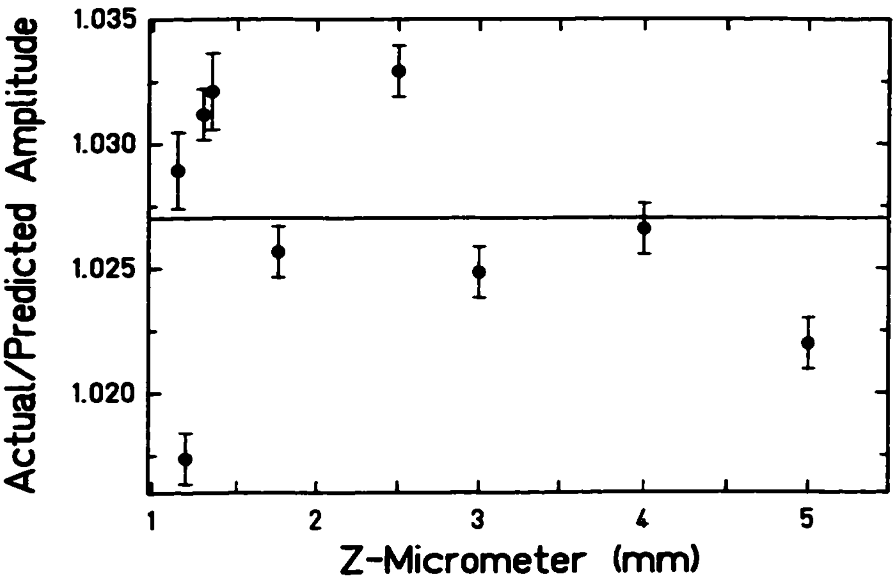

Figure 4.3: Values of the observed/predicted free oscillation amplitude after turning the rotation stage in the dynamic calibration as a function of vertical separation. The error bars do not include the ± 2.5% uncertainty in the stage position. The horizontal line is the average value.

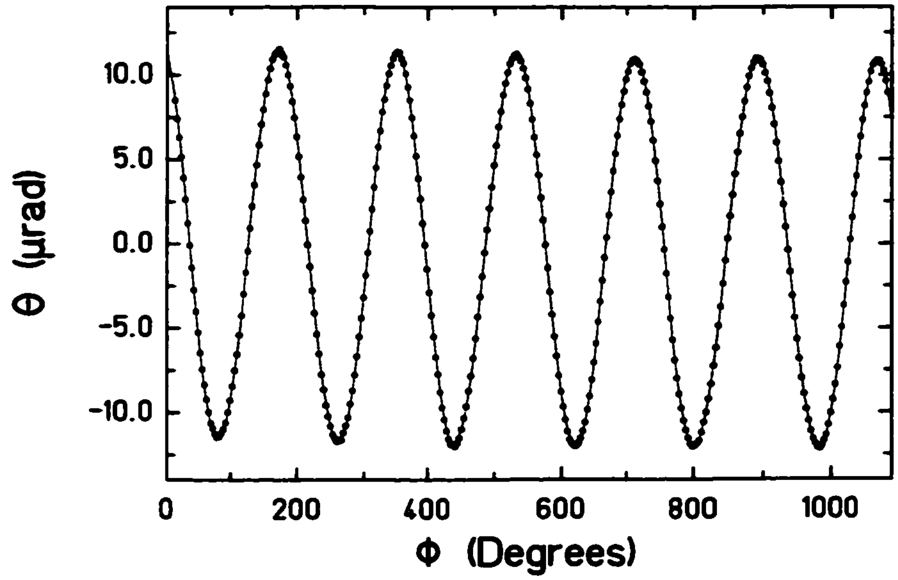

Figure 4.4: Data and fit for three revolutions of the calibration turntable. The $2\omega_c$ signal is dominant, as expected.

(see [28] pp. 13). The effect of horizontal misalignment was negligible. The vertical dependence of T_{calc} was symmetric about the alignment point. We took data at several vertical separations and horizontal offsets with the calibration setup.

The stray torque was determined by measuring the torque on the pendulum from the brass spheres when the pendulum spheres were removed (T^1_{stray}). We then measured T^2_{stray}, the torque produced on the pendulum and aluminum spheres when the brass spheres were removed. The measured torque to be compared to the multipole prediction was found using the relationship

$$T_{meas} = T_{tot} - T^1_{stray} - T^2_{stray}. \tag{4.9}$$

We assumed the values of $\kappa_o = 0.0317$, $c_1 = 1.322$, and $c_2 = -0.055$ and compared the observed angular deflection with the predicted torque. We adjusted the overall

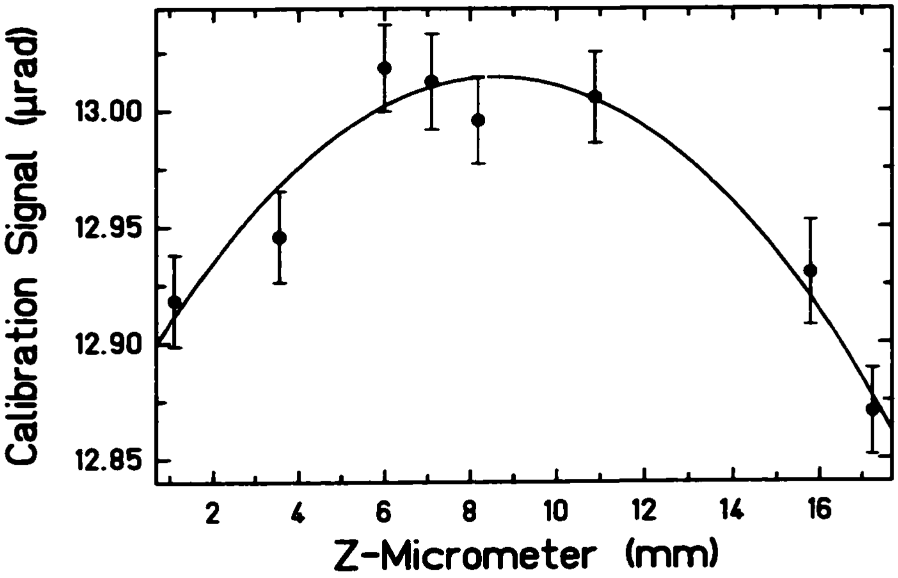

Figure 4.5: Calibration data as a function of vertical separation. The curve is a best fit to the data. The fit agrees well with the multipole prediction and yields an overall torque scale factor of $C = 1.0284 \pm 0.0005$ relative to the assumed values of κ_o, c_1, and c_2.

torque-scale factor, C, to satisfy the expression

$$C\,T_{calc} = T_{meas} = \kappa_o\,\theta. \tag{4.10}$$

We found $C = 1.0284 \pm 0.0005$. Figure 4.5 shows the observed signal as a function of vertical position and the best fit line based on the multipole prediction. This result was in agreement with the value $C = 1.027 \pm 0.025$ found for Experiment I.

Position Dependence of the Torque scale

In Experiment II, the calibration turntable was also used in each data run to test for a position dependence of the torque scale. The external spheres were placed on the turntable, but none on the pendulum. The q_{l4} multipole moments of the

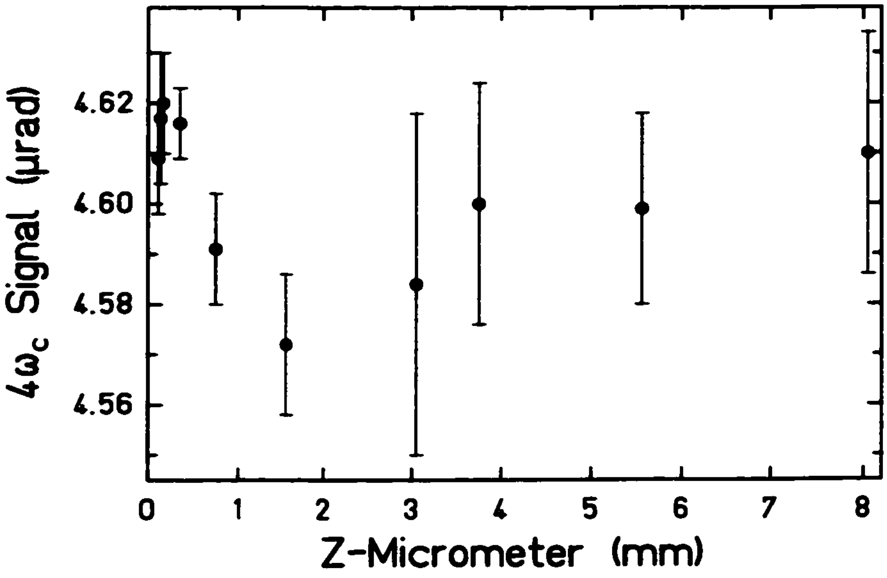

Figure 4.6: Measured size of the relative calibration signal as a function of vertical separation for Experiment II. We see there was a need to correct the data, especially at intermediate separations.

pendulum and Q_{l4} fields of the spheres interacted to produce a $4\omega_c$ torque. The calibration turntable was raised and lowered along with the pendulum to ensure the true torque was independent of vertical position. The observed twist due to this torque is shown in Figure 4.6 as a function of vertical position. We do see a small height dependence of the signal. This small deviation could have been caused by irregularities of the reflectivity or curvature of the pendulum mirror. The data for each point were corrected for this relative calibration change.

4.2.2 Missing Mass of the Holes

The missing mass of the holes determined the total torque on the pendulum. Uncertainty in this mass placed an additional uncertainty in the overall scale factor. In Experiment I, we inferred the missing mass by measuring the densities of the mate-

Table 4.4: Measured values of the parameters used to determine the missing mass of the holes in Experiment I from Eq. 4.11.

Value	Pendulum	Upper Att.	Lower Att.
M_1 (g)	9.7086 ± 0.0001	115.5455 ± 0.0003	451.8978 ± 0.0007
M_2 (g)	8.7124 ± 0.0001	106.1399 ± 0.0003	411.9664 ± 0.0007
R_h (mm)	4.7727 ± 0.0013	4.7790 ± 0.0013	6.3576 ± 0.0013
R_{add} (mm)	2.3901 ± 0.0013	4.7765 ± 0.0013	4.7701 ± 0.0013
N_{add}	10	8	8
M_h (g)	3.9721 ± 0.0040	11.7695 ± 0.0044	88.6657 ± 0.0188

rials and the hole dimensions. After we took all of the data for this experiment, we measured the masses, M_1, of the pendulum ring and the attractor disks. We then drilled ten additional holes in the pendulum ring and eight additional holes in each of the attractor disks. We measured the masses, M_2, of each of the pieces immediately following this operation, as well as the dimensions of the new holes. The total missing mass in the active holes of a given plate, M_h, was then determined from the relationship

$$M_h = (M_1 - M_2)\frac{V_h}{V_{add}} = (M_1 - M_2)\frac{10\,R_h^2}{N_{add}\,R_{add}^2}, \tag{4.11}$$

where $V_h = 10\pi R_h^2 t$ is the volume of the active holes (in a disk of thickness t), $V_{add} = N_{add}\pi R_{add}^2 t$ is the volume of the additional holes, and N_{add} is the number of additional holes in a given plate. Table 4.4 shows the measured values for these parameters. The fractional uncertainty of the product of the pendulum and upper disk hole masses must be incorporated into the total uncertainty of the torque scale. The relative scale factor , $R_l = 1.0000 \pm 0.0013$, represented the uncertainty in the ratio of the lower to upper hole masses.

A more direct technique was used to determine the missing mass of the holes in Experiment II. Each piece was weighed before the active holes were drilled (M_1) and then again immediately after drilling the holes (M_2). Since the upper plate had 2 sets of holes, the mass was measured after drilling each set. The attractor disks were then lapped to the final thickness. After lapping, the mass, M_3, was measured and once again after applying the gold layer (M_4). The pendulum was not lapped, hence, $M_3 = M_2$ for it. The resulting hole masses were

$$M_h = (M_1 - M_2)\frac{M_3}{M_2} + f_{Au}(M_4 - M_3), \tag{4.12}$$

where f_{Au} was a factor representing the fraction of the "area" of the holes which was covered with gold. Table 4.5 shows these measured values. For this experiment, the ratios $R_1 = 1.000000 \pm 0.000054$ and (lower/upper-inner) $R_2 = 1.000000 \pm 0.000048$ reflected the uncertainty in the torque scale (due the mass uncertainty alone) for the lower disk and upper disk out-of-phase holes, respectively.

4.2.3 Hole Placement

The calculated torques were based on the average values of the distance of the holes from the rotation axis and the angle between them. It was important to know whether there were any systematic deviations from the average values (for example, the holes could have been on an ellipse instead of a circle). Figures 4.7 and 4.8 show the radii and angles of the inner holes of the upper attractor disk in Experiment II, respectively. There are no systematic variations or outliers. The holes in each of the other disks (and pendulum rings) used in both experiments displayed similar behavior. The absence of any systematic variation in these parameters justified our use of their average values.

Table 4.5: Measured values of the parameters used to determine the missing mass of the holes in Experiment II from Eq. 4.12. The factor f_{Au} is negative for some hole sets because the gold deposited on the inner walls of the holes effectively reduced the "missing mass." The * indicates that, due to the machining sequence, the value of M_2 to be used in the ratio M_3/M_2 for the upper-inner set of holes should be the value of M_2 from the upper-outer column.

Value	Pendulum	Upper-Inner	Upper-Outer	Lower
M_1 (g)	19.0318±0.0001	219.0680±0.0003	210.0924±0.0003	497.4972±0.0004
M_2 (g)	16.3701±0.0001	210.0924±0.0003*	190.0470±0.0003	370.3206±0.0003
M_3 (g)	16.3701±0.0001	182.5952±0.0003	182.5952±0.0003	364.2692±0.0003
M_4 (g)	16.3808±0.0001	182.6066±0.0003	182.6066±0.0003	364.2692±0.0003
f_{Au}	0.00673	-0.07579	-0.01876	0.0000
M_h (g)	2.66177±0.00014	8.6228±0.0004	19.2592±0.0005	125.0984±0.0006

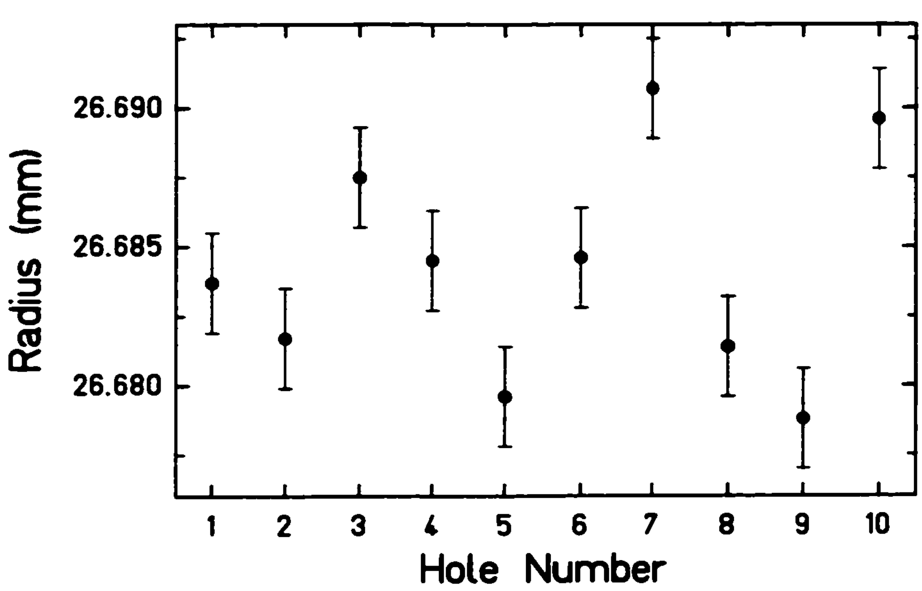

Figure 4.7: Radial position of the individual inner holes of the Experiment II upper attractor disk. There is no systematic variation.

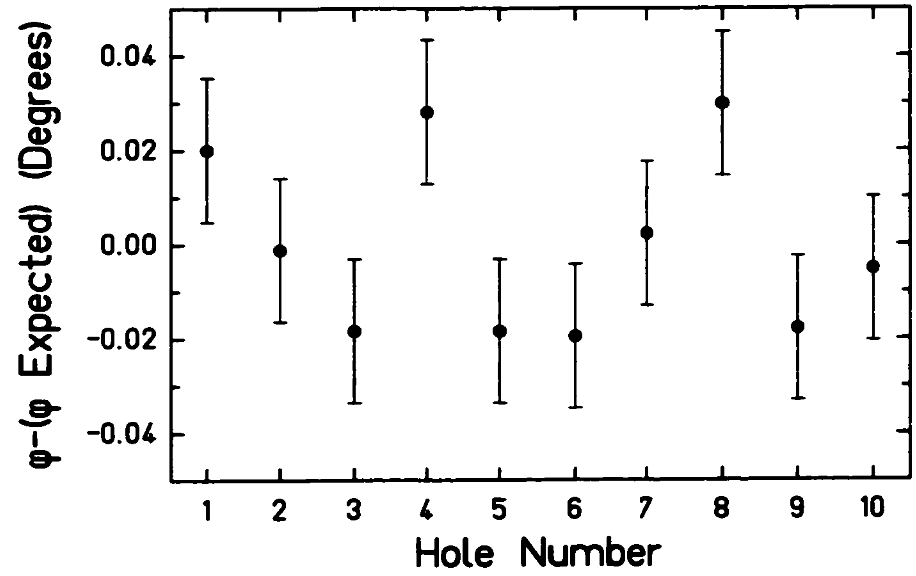

Figure 4.8: Residuals of the angle between the individual inner holes of the Experiment II upper attractor disk. Again, there is no systematic variation.

4.2.4 Attractor Disk Gap

If the attractor disks were not seated together, the wrong value of the distance to the lower plate would have been used in predicting the torque. We included this possible gap as a parameter in our final analysis; however, we needed to constrain such an imperfection to ensure the analysis was accurate.

The method was simple, we measured the thicknesses of the disks individually and the total thickness when the two were stacked with a precision micrometer. In Experiment I, the upper and lower disks had thicknesses of 1.846 ± 0.005 mm and 7.825 ± 0.005 mm, respectively. When the disks were stacked the combined thickness was 9.681 ± 0.007 mm; the difference was $\delta z = 0.010 \pm 0.010$ mm.

In Experiment II, we used the same technique, but we took many thickness measurements and used a micrometer of improved precision. We measured $\delta z = 0.0014 \pm 0.0010$ mm for these disks.

4.2.5 Pendulum-to-Attractor Separation

We assigned an error on the pendulum-to-attractor vertical separation (and horizontal offset) for each run using the techniques described in Sections 3.2.2, 3.4, and 3.5. We found the electronic micrometers to be reproducible within their ± 2 μm specification (after correcting for the calibration described in Section 2.3.5) by measuring their position with a precision mechanical counterpart (see Figure 2.7). The position of the conducting membrane as read on the micrometers was determined to within ± 3 μm capacitively, and the membrane-to-attractor separation was determined with the same tolerance. We therefore determined the position at which the pendulum would touch the attractor, z_o, within $\pm\sqrt{(0.002)^2 + (0.003)^2 + (0.003)^2} = \pm 0.005$ mm. We chose to scale the separation such that the measured value was $z_o = 0.000 \pm 0.005$ mm for each experiment. In Experiment I, certain runs used only the upper attractor disk.

Table 4.6: Measured values of the instrumental parameters, described in Section 4.2, for both experiments. The uncertainties in the values of C include the uncertainties in the hole masses of the pendulum and in-phase attractor holes, as well as torque-scale factor measurement. The ratios R_1 and R_2 reflect the uncertainty in the ratios of the out-of-phase to in-phase hole masses (the ratios are expected to be one because the calculation of the torques assumes the measured central values of the hole masses).

Parameter	Experiment I	Experiment II
C	1.027 ± 0.025	1.0284 ± 0.0005
R_1	1.0000 ± 0.0013	1.000000 ± 0.000054
R_2	N/A	1.000000 ± 0.000048
z_o	0.000 ± 0.005 mm	0.000 ± 0.005 mm
ζ	0.000 ± 0.030 mm	N/A
δz	0.010 ± 0.010 mm	0.0014 ± 0.0010 mm

The parameter ζ represented the vertical position at vanishing pendulum-to-upper-disk separation. Because the membrane-to-upper-disk distance was measured with a less precise micrometer, the error on ζ was ± 0.030 mm. We also scaled this parameter so that $\zeta = 0.00 \pm 0.030$ mm. We took the error of the horizontal offset positions to be the stage specification, ± 2 μm.

4.2.6 Summary

We performed independent measurements to constrain the values of the instrumental parameters necessary to compare the data to the predicted torques. Table 4.6 shows the results of these measurements. The parameters and their errors will be used in the analysis of Chapter 7.

Chapter 5

CALCULATION OF GRAVITATIONAL AND YUKAWA TORQUES

In this chapter we describe the process used to calculate the expected Newtonian and possible Yukawa torques on our pendulums. The majority of the information presented in this chapter was obtained from Ulrich Schmidt [31], who was primarily responsible for the calculations.

5.1 Introduction

If we choose a Cartesian coordinate system in which the torsion fiber lies along the $\hat{z}$ axis, the torque produced about the fiber axis due to an interaction between a point mass on the pendulum and an arbitrary mass distribution on the attractor is

$$T_z = x_p F_y^{pa} - y_p F_x^{pa}, \tag{5.1}$$

where $\vec{F}^{pa}$ is the total force on the pendulum point mass due to the attractor mass distribution, and x_p and y_p are the coordinates of the pendulum mass.

We modeled the holes as perfect cylinders with symmetry axes in the $\hat{z}$ direction. (The true force is, of course, due to the mass left after drilling the holes; however, we obtained the correct result by assuming the holes had a negative density and the positive density mass was cylindrically symmetric.) We see from Equation 5.1 that we only needed to calculate the horizontal components of the force between these cylinders. Cylindrical symmetry ensured that this force effectively acted on the symmetry axes of the holes; therefore, x_p and y_p could be taken to be the positions of the pendulum hole centers. Cylindrical symmetry allowed further simplification. Since we performed the calculations in a coordinate system in which one cylinder was at the origin, we chose to place the other along the $\hat{x}$ axis and needed to only calculate the $\hat{x}$ component of the force. Once this force was known as a function of vertical separation and horizontal offset, we performed the appropriate weighted sum over pendulum and attractor hole positions to obtain the total torque. The harmonic torque components were then extracted with Fourier analysis of the total torque.

5.2 General Approach

The total gravitational and Yukawa force between two extended bodies of (uniform) densities ρ_1 and ρ_2 is given by

$$\vec{F}_{12} = -G\rho_1\rho_2 \oint_{V1} \oint_{V2} dV_1\, dV_2\, \hat{R} \left[\frac{1}{R^2} + \frac{\alpha\, e^{-(R/\lambda)}}{R} \left(\frac{1}{\lambda} + \frac{1}{R} \right) \right], \qquad (5.2)$$

where the integrals extend over the volumes V_1 and V_2 of each interacting object and $R = |\vec{R}_2 - \vec{R}_1|$. The first term of the integrand represents the Newtonian contribution to the force. We performed separate calculations of the Newtonian and Yukawa forces.

As many of the six integrals as possible were done analytically, the remainder being done numerically. We found analytic solutions to four of the Newtonian integrals. The Yukawa integrand was separated into 9 geometrically distinct regions as described in Section 5.3.2; the total Yukawa force was the sum of these 9 terms. Three of these terms were numerically integrated over three dimensions, while the remaining 6 terms required a four-dimensional numerical integration. The integrations were done with the standard 'NIntegrate' function of *Mathematica*. This adaptive function approximated the integrands as polynomials and chose the integration step size to achieve the required precision and accuracy. The output of this function provided error messages if the desired levels were not attainable.

These calculations were difficult because of the high precision needed for the harmonic torque components. The maximum possible 10ω twist amplitude (for Experiment I) was 34 μrad (upper plate only with a pendulum-to-attractor vertical separation of 0.22 mm). The statistical noise on the 10ω signal was typically about 8 nrad; therfore, we wanted the computed Newtonian torque components to have a maximum error of <1 nrad. We thus needed to calculate the Newtonian torques to a fractional precision of better than $\sim 3 \times 10^{-5}$. A comparable precision for the Yukawa torques was obtained.

Such high-precision numerical integrations required long computing times. The following sections describe the strategies we used to perform the calculations in a reasonable amount of time (on the order of weeks).

5.3 Form of the Force Integrals

5.3.1 Newtonian Interaction

For the hole arrangement shown in Figure 5.1, all four X and Z integrals can be done analytically. The resulting function is the force per unit (thickness)^2 between two infinitely thin, rectangular sheets that lie parallel to the X-Z plane. This function must then be numerically integrated over the extents of both cylinders in the Y direction to obtain the total force.

If the sheets have the dimensions shown in the upper panel of Figure 5.1, the resulting force per unit (thickness)^2 in the X direction is

$$\left|\mathcal{F}_x^G(Y_1, Y_2, x, z)\right| = \left|\sum_{i=1}^{4}\sum_{j=1}^{4} s_i\, s_j\, f_G(X_i,\, R_i,\, Z_j)\right|, \tag{5.3}$$

where $R_i = \sqrt{X_i^2 + \Delta y^2 + Z_j^2}$, $\Delta y = Y_2 - Y_1$ and

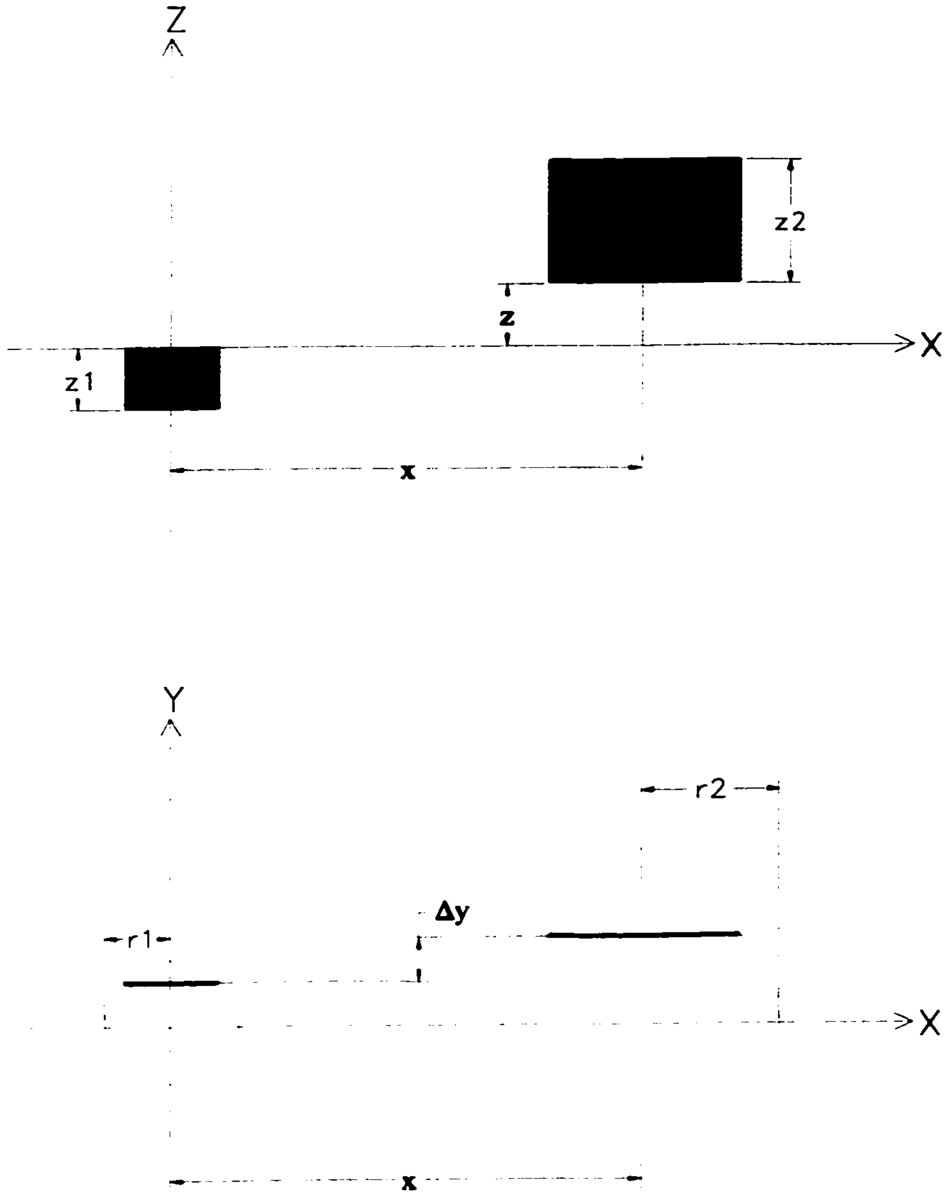

Figure 5.1: Diagram of the coordinate system used to calculate the horizontal component of the force between two cylinders. Top: Side view of the X-Z plane showing two rectangular sheets representing cross sections of the cylinders. Bottom: Top view of the X-Y plane showing that the sheets are inside the cylinders at different values of Y.

Table 5.1: Values of the parameters used to evaluate the Newtonian integrand of Equation 5.3.

i, j	s_i	s_j	X_i	Z_j
1	$+$	$+$	$x - \sqrt{r_2^2 - Y_2^2} - \sqrt{r_1^2 - Y_1^2}$	z
2	$-$	$-$	$x - \sqrt{r_2^2 - Y_2^2} + \sqrt{r_1^2 - Y_1^2}$	$z + z_1$
3	$-$	$-$	$x + \sqrt{r_2^2 - Y_2^2} - \sqrt{r_1^2 - Y_1^2}$	$z + z_2$
4	$+$	$+$	$x + \sqrt{r_2^2 - Y_2^2} + \sqrt{r_1^2 - Y_1^2}$	$z + z_2 + z_1$

$$\begin{aligned} f_G(X, R, Z) &= \frac{-G\rho_1\rho_2}{2} \times \qquad (5.4) \\ &\left[X\,R + \Delta y^2 \ln(X+R) + Z^2 \ln(R-X) + X\,Z \ln\left(\frac{R-Z}{R+Z}\right)\right. \\ &\left. +\Delta y\,Z\left(\tan^{-1}\left[\frac{\Delta y^2 + Z^2 + R\,Z}{X\,\Delta y}\right] - \tan^{-1}\left[\frac{\Delta y^2 + Z^2 - R\,Z}{X\,\Delta y}\right]\right)\right]. \end{aligned}$$

The ith and jth values of the parameters are given in Table 5.1. To obtain the total force between the two cylinders, the function $\mathcal{F}_x^G$ (with 96 terms) must be numerically integrated over the Y_1 and Y_2 dimensions of the cylinders. Due to reflection symmetry about the X-Z plane, we only need to integrate one half of one cylinder and multiply the result by two. Using Equations 5.3 and 5.5, the total force is

$$|F_x^G(x, z)| = 2\int_{-r_2}^{r_2}\int_0^{r_1} \left|\mathcal{F}_x^G(Y_1, Y_2, x, z)\right|\, dY_1 dY_2. \qquad (5.5)$$

We increased the precision of the calculation by approximating the square root terms in the integrand with

$$R = Z\sqrt{1+\epsilon} \approx Z\left(1 + \frac{\epsilon}{2} + \frac{\epsilon^2}{8} + \frac{\epsilon^3}{16}\right), \qquad (5.6)$$

where $\epsilon = ((X_2 - X_1)^2 + (Y_2 - Y_1)^2)/(Z_2 - Z_1)^2$. We also used the approximation

$$\ln\left(\frac{R-Z}{R+Z}\right) \approx \ln\left(\frac{\epsilon - \epsilon^2/4 + \epsilon^3/8}{4 + \epsilon - \epsilon^2/4 + \epsilon^3/8}\right). \qquad (5.7)$$

Both approximations were used with $\epsilon < 10^{-4}$.

We checked the error of the approximations in Equations 5.6 and 5.7 by evaluating the integrand, $\mathcal{F}_x^G(Y_1, Y_2, x, 0.1\ \mathrm{mm})$, for 10^5 random combinations of Y_1, Y_2, and x for each attractor hole set. We compared each value with a 30-digit precision evaluation of the integrand (calculated with standard *Mathematica* functions). We found a fractional maximum deviation of 10^{-12} between our approximated integrand and the 30-digit precision calculation. This difference was sufficiently small to ensure that the final fractional precision of 10^{-6} was attainable.

With these approximations the calculations were still slow, typically taking ~ 30 s per integration for a given vertical separation and horizontal offset. We increased the speed dramatically by implementing a simple coordinate transformation. We transformed the Y coordinates of the two holes trigonometrically, $Y_i \rightarrow r_i \sin(\theta_i)$. This transformation converted the integrand to a function that was easier to approximate with polynomials, and thereby increasing the calculation speed. With this transformation, Equation 5.5 becomes

$$|F_x^G(x,z)| = 2\int_{-\pi/2}^{\pi/2}\int_0^{\pi/2} |\mathcal{F}_x^G(\theta_1, \theta_2, x, z)|\, r_1\cos(\theta_1) r_2 \cos(\theta_2)\, d\theta_1 d\theta_2. \tag{5.8}$$

In Figure 5.2 we see the integrand (with $Y_1 = 0$) and a 5^{th} order polynomial approximation obtained from 7 equally spaced sample points between $Y_2 = -r_2$ and $Y_2 = r_2$. The blue and green curves are the integrand and its polynomial approximation without the trigonometric substitution, respectively. There is a 2.3% difference between the area under these two curves. The red and black curves are the integrand and approximation after the coordinate transformation. In this example, there is only a 0.3% error (of course many more points were used to achieve the required precision of the Newtonian force). The trigonometric substitution improved the precision by almost a factor of ten for the same number of sample points. The time to perform the complete integration between a pendulum and upper attractor hole pair (with

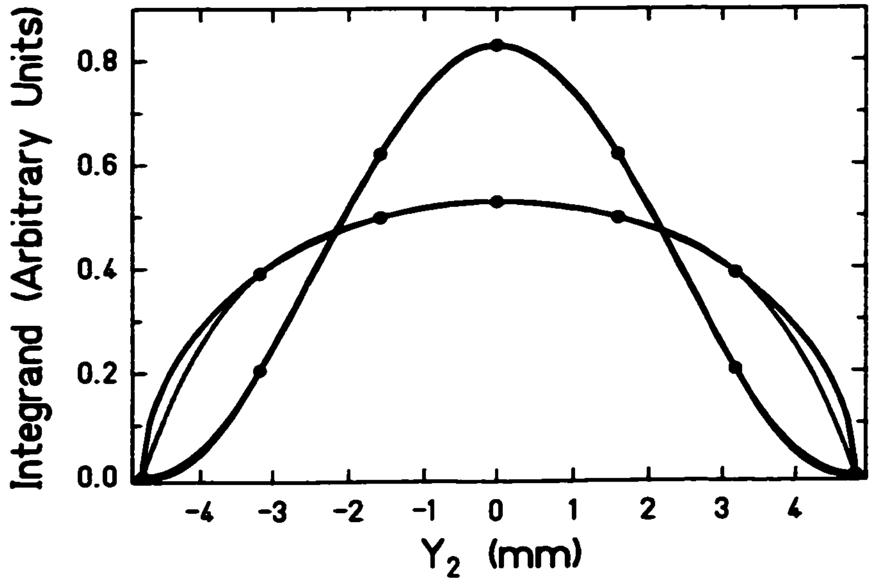

Figure 5.2: Values of the Newtonian integrand, $\mathcal{F}_x^G(0, Y_2, 10\text{ mm}, 0.1\text{ mm})$, as a function of the position Y_2. The radius of cylinder '2' is $r_2 = 4.7625$ mm. The blue curve is a precise evaluation of the integrand without the trigonometric substitution. The green curve is a 5^{th} order polynomial approximation obtained from 7 sample points; there is a 2.3% error between the areas under the two curves. The black and red curves are the integrand and approximation after the coordinate transformation, $Y_2 \rightarrow r_2 \sin(\theta_2)$, respectively. The error for the same number of sample points is now only 0.3%.

x=10 mm, z=0.1 mm, and a 400 MHz, Pentium III processor) in Experiment I was 22.4 s without the transformation and 8.2 s with it, an improvement by a factor of almost three. At this improved speed we were able to calculate the complete Newtonian force database in about 3 days with a fractional precision of 10^{-6} for each integration.

In Experiment I, the Newtonian force between a pendulum and attractor hole pair was calculated for 248 points between x=0.1 mm and 60 mm for each of 27 values of the vertical separation in the range $0.1 \leq z \leq 20$ mm for the upper disk (only 20 values in the range $0.1 \leq z \leq 10.5$ mm were used for the lower disk). For all three hole sizes of the Experiment II attractor, the force was calculated for 327 values in the range $0 \leq x \leq 85$ mm for 22 values of z between 0.1 mm and 12.5 mm.

5.3.2 Yukawa Interaction

To simplify the Yukawa calculations we made additional coordinate transformations. We denote the Yukawa integrand of Equation 5.2 as $\alpha f_Y(X, Y, Z, \lambda)$ and note that the force only depends upon the difference of the coordinates ($X = X_2 - X_1$, etc.). The first transformation of the X variables is $x_d = X_2 - X_1$ and $x_s = X_1 + X_2$. Since the integrand is independent of x_s, the X integrations now become

$$\int_{X_{1_{min}}}^{X_{1_{max}}} \int_{X_{2_{min}}}^{X_{2_{max}}} f_Y(X, Y, Z, \lambda)\, dX_1\, dX_2 = \frac{1}{2} \int_{x_{d_{min}}}^{x_{d_{max}}} g(x_d)\, f_Y(x_d, Y, Z, \lambda)\, dx_d. \tag{5.9}$$

If we define the quantities

$$\begin{aligned}
x_{dd} &\equiv \min(X_{1_{max}} - X_{1_{min}}, X_{2_{max}} - X_{2_{min}}) \\
x_{d_1} &\equiv X_{2_{min}} - X_{1_{max}} \\
x_{d_2} &\equiv x_{d_1} + x_{dd} \\
x_{d_3} &\equiv x_{d_4} - x_{dd} \\
x_{d_4} &\equiv X_{2_{max}} - X_{1_{min}},
\end{aligned} \tag{5.10}$$

we obtain three conditions on the function $g(x_d)$:

$$\begin{aligned}
g(x_d) &= 2(x_d - x_{d_1}) \quad \text{for} \quad x_{d_1} \leq x_d \leq x_{d_2} \\
g(x_d) &= 2(x_{d_2} - x_{d_1}) \quad \text{for} \quad x_{d_2} \leq x_d \leq x_{d_3} \\
g(x_d) &= 2(x_{d_4} - x_d) \quad \text{for} \quad x_{d_3} \leq x_d \leq x_{d_4}.
\end{aligned} \tag{5.11}$$

We analytically evaluated the term in which $g(x_d)$ is independent of x_d to obtain

$$\begin{aligned}\int_{X_{1_{min}}}^{X_{1_{max}}}\int_{X_{2_{min}}}^{X_{2_{max}}} f_Y(x_d, Y, Z, \lambda)\, dX_1\, dX_2 \;&=\; \int_{x_{d_1}}^{x_{d_2}} (x_d - x_{d_1}) f_Y(x_d, Y, Z, \lambda)\, dx_d \\ &+ \int_{x_{d_3}}^{x_{d_4}} (x_{d_4} - x_d) f_Y(x_d, Y, Z, \lambda)\, dx_d \;+\; x_{dd}\, \frac{\mathrm{e}^{-R/\lambda}}{R}\bigg|_{x_{d_2}}^{x_{d_3}},\end{aligned} \tag{5.12}$$

where $R = \sqrt{x_d^2 + Y^2 + Z^2}$. To avoid poles in the integration when $x_d - x_{d_1} = 0$ and $x_{d_4} = x_d = 0$, we again transformed the variables in the remaining integrals so that they are dimensionless and are integrated over the region 0→1:

$$\begin{aligned}\int_{X_{1_{min}}}^{X_{1_{max}}}\int_{X_{2_{min}}}^{X_{2_{max}}} f_Y(x_d, Y, Z, \lambda)\, dX_1\, dX_2 \;&=\; x_{dd}^2 \int_0^1 [q\, f_Y(x_{dd}\, q + x_{d_1}, Y, Z, \lambda) \\ &+ (1-q) f_Y(x_{dd}\, q + x_{d_3}, Y, Z, \lambda)\,]\; dq \;+\; x_{dd}\, \frac{\mathrm{e}^{-R/\lambda}}{R}\bigg|_{x_{d_2}}^{x_{d_3}},\end{aligned} \tag{5.13}$$

We performed the analogous transformations for the Z coordinates as well ($z_d = Z_2 - Z_1$ and $z_s = Z_1 + Z_2$). The z_s integral can be done analytically; however, the z_d integration must be done numerically for every term. We thus obtained nine terms corresponding to three regions in X and three in Z. The numerical integration is performed over a different number of dimensions depending on the region; one-third of the numerical integrations are done in three dimensions, while the remaining terms require a four-dimensional numerical integration.

The Yukawa force was calculated as a function of x and z for 24 values of λ between 0.02 – 10 mm. Since the absolute Yukawa torque on the pendulum was proportional to α, the uncertainty in the calculated Yukawa torques places a systematic uncertainty on the fitted values of α. We required (and obtained) a fractional precision of 10^{-4} for all calculated Yukawa force values. The fractional uncertainty in α from the fitting process (see Chapter 7) was > 0.4 for all 24 values of λ for both experiments. Therefore, the systematic uncertainty from the calculation was negligible.

5.4 Interpolation of the Force Databases

After obtaining the values of the Newtonian and Yukawa forces on a grid of points $(x(i), z(i), \lambda)$, the values were interpolated in the horizontal direction (for each fixed value of z) to create the functions $f^{z}_{int}(x)$. We used cubic spline interpolation (see, for example, Ref. [32], pp. 113) to achieve the required precision. A plot of the interpolated Newtonian force between one pendulum hole and one upper attractor hole (of Experiment I) as a function of x is shown in Figure 5.3. The lower panel of this figure shows the fractional error on the force. The error was estimated by calculating the 4th order term

$$f^{z}_{err}(x) = \frac{1}{24}\left(\frac{\Delta x}{2}\right)^4 \left.\frac{\partial^4 f^{z}_{int}(x)}{\partial x^4}\right|_{\bar{x}}, \tag{5.14}$$

where $\Delta x = x(i+1) - x(i)$ and $\bar{x} = (x(i) + x(i+1))/2$. The fractional error on the Newtonian (Yukawa) force interpolation never exceeded 2×10^{-7} (1×10^{-5}), so the error on the force introduced by the interpolation was not significant when compared to the 10^{-6} (10^{-4}) fractional error of the integration.

5.5 Calculation of the Harmonic Torque Components

We calculated the torque by summing the contributions of the pendulum and attractor holes. For the arrangement shown in Figure 5.4, the torque about the torsion fiber axis from the interaction between the (red) pendulum hole and the (blue) attractor hole is

$$T_1(\phi_a, \phi_p, \rho_{off}, z) = r_p F(x,z) \left(\frac{r_a \sin(\phi_a) + \rho_{off}\sin(\phi_p)}{x}\right), \tag{5.15}$$

where

$$x = \sqrt{(r_a \sin(\phi_a) + \rho_{off}\sin(\phi_p))^2 + (r_a\cos(\phi_a) + \rho_{off}\cos(\phi_p) - r_p)^2}, \tag{5.16}$$

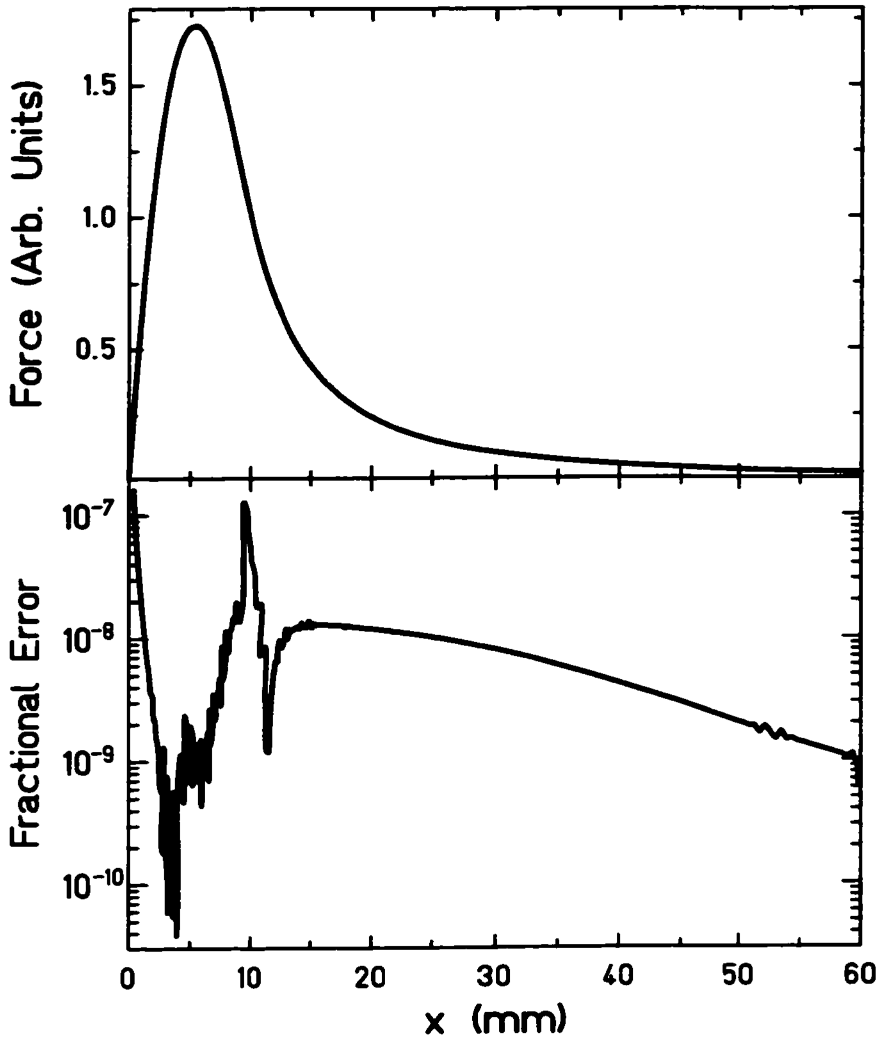

Figure 5.3: Top: Interpolated Newtonian force ($f^{0.1}_{int}(x)$) as a function of horizontal offset, x, between a pendulum and upper attractor hole pair from Experiment I at a vertical separation of $z = 0.1$ mm. Bottom: The fractional error function $f^{0.1}_{err}(x)/f^{0.1}_{int}(x)$. The fractional error is never more than 2×10^{-7} (by symmetry, $f^{z}_{int}(0) = 0$).

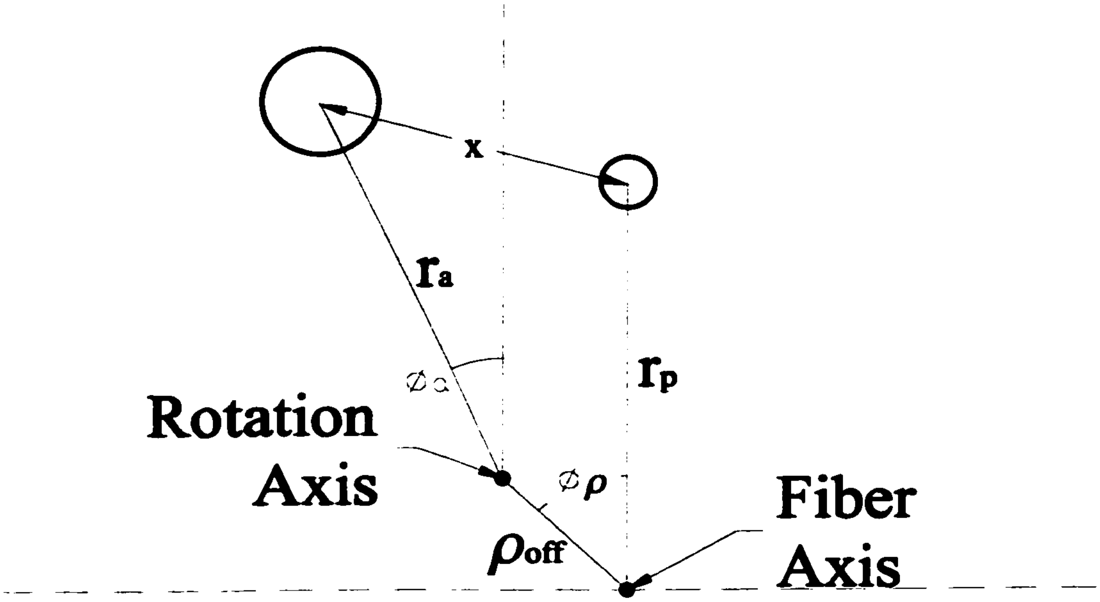

Figure 5.4: Depiction of the geometry used to calculate the torque on the pendulum. The attractor hole is blue while that of the pendulum is red.

r_p is the horizontal distance of the pendulum hole center from the torsion fiber, r_a is the horizontal distance of the attractor hole center from the rotation axis, ρ_{off} is the horizontal offset between the fiber and rotation axes, ϕ_a is the attractor hole angle (relative to the position in which there is no torque about the fiber axis), $F(x, z)$ is the total horizontal force on the hole (Newtonian plus Yukawa), and ϕ_ρ represents the direction of the horizontal displacement. To calculate the total torque on the pendulum from one complete set of attractor holes as a function of attractor rotation angle, ϕ, we let $\phi_a = \phi_\text{o} + \phi$. We must include 100 terms, the torque from each of the 10 attractor holes on the 10 pendulum holes:

$$T(\phi, \rho_{off}, \phi_\rho, z) = \sum_{i=0}^{9} \sum_{j=0}^{9} T_1(\phi + \phi_\text{o} + i\,\pi/5,\ \phi_\rho - j\,\pi/5,\ \rho_{off},\ z). \qquad (5.17)$$

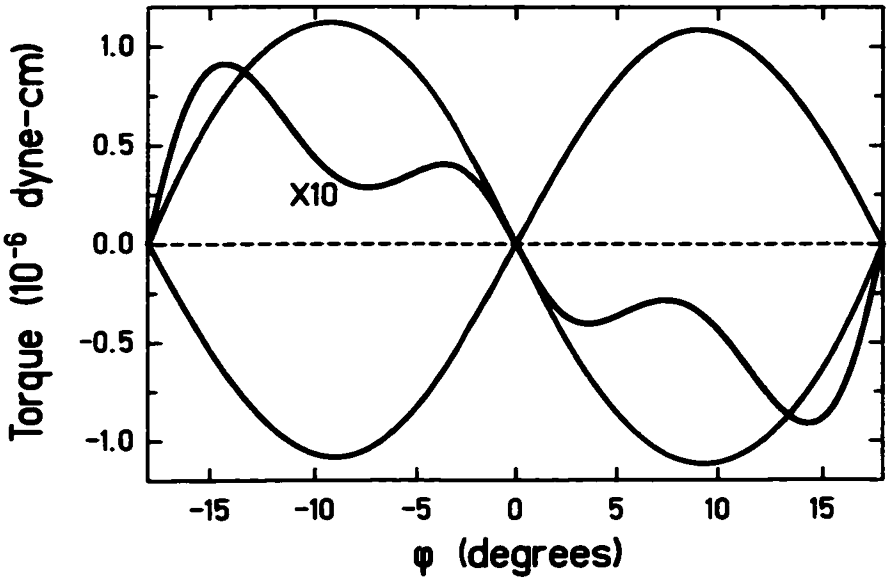

Figure 5.5: Calculated total Newtonian torque on the Experiment I pendulum due to the attractor as a function of attractor rotation angle ($z = 0.1$ mm). The red curve is the torque from the upper disk, the blue is from the lower. The black curve is the total torque, magnified by a factor of ten for clarity. The horizontal axis spans $2\pi/10$, we clearly see the 10ω signal as well as the higher harmonics.

We performed the calculation for offset angles $\phi_\rho = 0$ and $\phi_\rho = \pi/2$ and found the results identical to within 10^{-11} dyne-cm. Therefore, without loss of generality, we fixed $\phi_\rho = 0$.

Because of the tenfold rotational symmetry of the attractor, we needed to only calculate the torque for attractor angles ranging between 0 and $2\pi/10$ to extract the harmonic components. Figure 5.5 shows the calculated torque due to the upper and lower disks for attractor angles between $-\pi/10$ and $\pi/10$ for a vertical separation of $z = 0.1$ mm in Experiment I. The integrands had units of mm^5, so the conversion factors, $G\,\rho_1\,\rho_2$, used the values shown in Table 5.2 with $G = 6.672 \times 10^{-13}$ cm^8/(g·s^2·mm^5).

Table 5.2: Parameters used to convert the calculated torque to physical units with the conversion factor $G\,\rho_1\,\rho_2$. The volumes are calculated with the hole parameters described in Chapter 2, the masses are taken from Tables 4.4 and 4.5, and the densities, ρ, are calculated from the relationship $\rho = M_h/V_h$. The difference in density for the two attractor disks in Experiment I is due to the fact that the disks were made from separate pieces of stock.

	Experiment I			Experiment II			
	Pend.	Upper	Lower	Pend.	Inner	Outer	Lower
M_h (g)	0.39721	1.17695	8.86657	0.266177	0.86228	1.92592	12.50984
V_h (cm^3)	0.14323	0.132451	0.99362	0.095087	0.0962481	0.214979	1.396323
ρ (g/cm^3)	2.7732	8.88592	8.92350	2.7993	8.95893	8.95866	8.95913

The harmonic amplitude of the torque with frequency $n\omega$ is given by the Fourier amplitude

$$a_n(\rho_{off}, z) = 10 \cdot \frac{2}{\pi} \int_0^{\pi/10} T(\phi, \rho_{off}, 0, z) \sin(n\,\phi)\, d\phi. \tag{5.18}$$

The factor of 2 arises because we chose the phase such that the torque was an odd function about $\phi = 0$. Therefore, we needed to only calculate the harmonic amplitudes in the range $0 \leq \phi \leq \pi/10$. We approximated this integral with a 32-point, third-order Fourier sine transform. We verified the precision of the Fourier amplitudes by performing the transform with 64 points instead of 32 and found the fractional precision to be better than 10^{-6} (10^{-5}) for the Newtonian (Yukawa) amplitudes. We extracted the harmonic components of the torque for 20 different values of horizontal offset between $0 \leq \rho_{off} \leq 2$ mm for each value of z used in the force calculations for each hole set.

5.6 *Generation of the Interpolated Torque Functions*

Once we obtained the values of the harmonic torque coefficients, we used a cubic spline interpolation to generate fully analytic, two-dimensional functions for the harmonic torque amplitudes from each set of holes in the attractor disks for all signal frequencies of interest. The interpolating functions of the 10ω torque from both attractor disks of Experiment I as a function of vertical separation (no horizontal offset), as well as their sum are shown in the top panel of Figure 5.6. The bottom panel shows the error of the function, estimated analogously to Equation 5.14. We see that the error is below our required level of 3×10^{-11} dyne-cm over the region where we took data ($z = 0.2 - 7$ mm for the lower plate and $z = 0.2 - 10.8$ mm for the upper plate). The fractional error imposed from the Yukawa interpolation was $< 10^{-5}$.

For Experiment I, we generated three interpolating functions $T^{G}_{(up,\ I)}(n, \rho_{off}, z)$ for n=10, 20, and 30 that described the Newtonian torques from the upper attractor disk. Another three functions, $T^{G}_{(low,\ I)}(n, \rho_{off}, z)$, described the torque from the lower disk. The parameter z for the lower disk included the offset arising from the upper disk thickness. We also generated the Yukawa torque functions $T^{Y}_{(up,\ I)}(n, \rho_{off}, z, \lambda)$ and $T^{Y}_{(low,\ I)}(n, \rho_{off}, z, \lambda)$. The calculated Yukawa torques assumed $\alpha = 1$.

For Experiment II, we generated a total of six functions corresponding to n=10 and 20 for the three sets of attractor holes. The functions $T^{G}_{(upin,\ II)}(n, \rho_{off}, z)$ were the interpolating functions describing the in-phase torques from the inner ring of holes in the upper attractor disk, while $T^{G}_{(upout,\ II)}(n, \rho_{off}, z)$ and $T^{G}_{(low,\ II)}(n, \rho_{off}, z)$ were the torque functions due to the upper-disk, out-of-phase holes and the lower disk respectively. The corresponding Yukawa torque functions were $T^{Y}_{(upin,\ II)}(n, \rho_{off}, z, \lambda)$, $T^{Y}_{(upout,\ II)}(n, \rho_{off}, z, \lambda)$, and $T^{Y}_{(low,\ II)}(n, \rho_{off}, z, \lambda)$. The data were compared to these functions as described in Chapter 7.

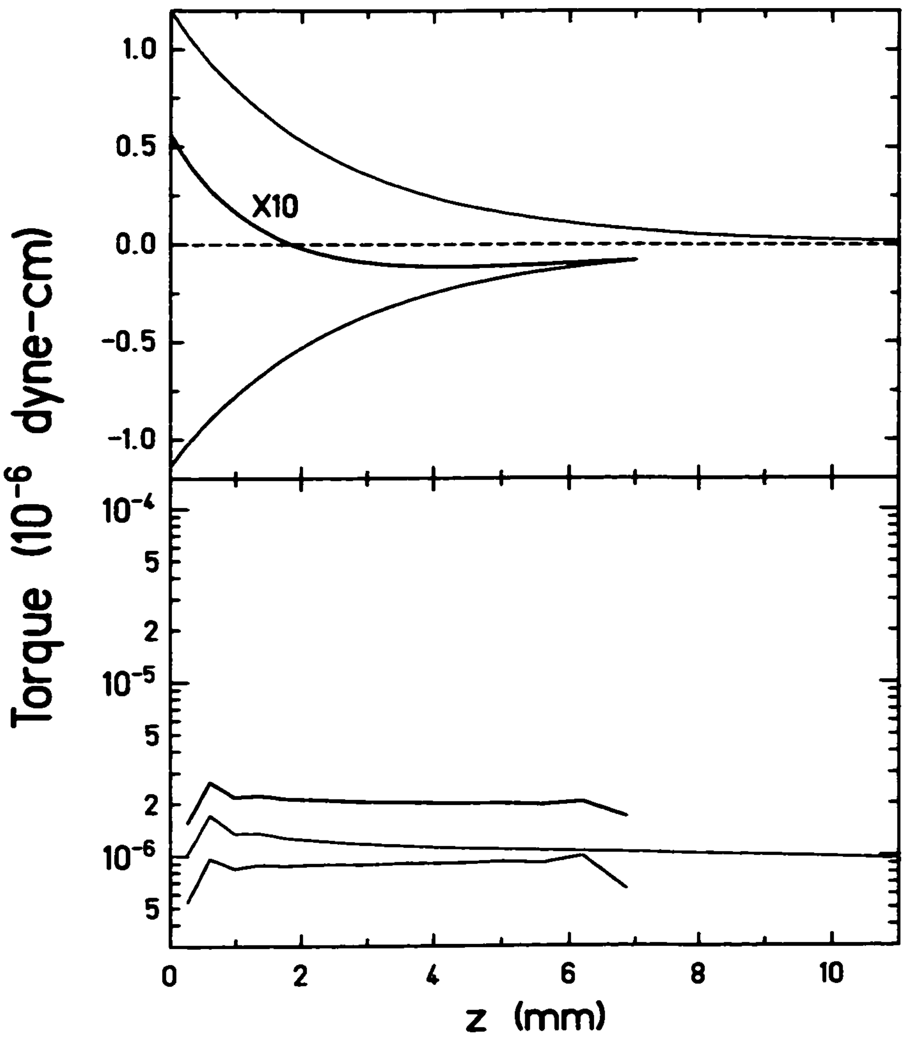

Figure 5.6: Top: Predicted 10ω torques for Experiment I. The red curve is the torque from the upper disk, the blue is that due to the lower disk, and the black is the total torque (exaggerated by a factor of 10). Bottom: Error on the interpolated torque. We see the error is below the required 3×10^{-11} dyne-cm level over the entire range of vertical separations covered by our data (data was taken with the lower disk only up to a vertical separation of ~7 mm).

Table 5.3: Error budget for the calculation of the Newtonian torques. We see that the sum of all the errors is below the required level of 3×10^{-11} dyne-cm. The fractional errors of the top three sources were converted to absolute errors by assuming the error was applied to the maximum torque.

Source	Error
Force Calculation	1×10^{-12} dyne-cm
Force Interpolation	$\lesssim 2 \times 10^{-13}$ dyne-cm
Fourier Analysis	$\lesssim 1 \times 10^{-12}$ dyne-cm
Torque Interpolation	$\lesssim 2 \times 10^{-11}$ dyne-cm
Total	$\sim 2 \times 10^{-11}$ dyne-cm

5.7 Torque Calculation Error Budget

For the Newtonian torques, we required an absolute error of $\lesssim 3 \times 10^{-11}$ dyne-cm (this was true for each experiment). The contributions to the calculation error for the Newtonian torques are shown in Table 5.3. The sum of the errors is less than the required 3×10^{-11} dyne-cm. The contributions to the fractional error of the Yukawa torques are shown in Table 5.4. The sum of these contributions is also well below the $> 40\%$ fractional error on the fitted values of α (see Chapter 7).

Table 5.4: Error budget for the calculation of the Yukawa torques. All values are fractional. We see that the sum of all the errors is well below the $> 40\%$ error on the fitted values of α.

Source	Error
Force Calculation	1×10^{-4}
Force Interpolation	$\lesssim 1 \times 10^{-5}$
Fourier Analysis	$\lesssim 1 \times 10^{-5}$
Torque Interpolation	$\lesssim 1 \times 10^{-5}$
Total	$\sim 1 \times 10^{-4}$

Chapter 6

DATA ANALYSIS: EXTRACTING THE PENDULUM TORQUES

This chapter describes the analysis procedures we used to extract the signal torques from the observed pendulum twist. The harmonic components of the torque are used in the following chapter to constrain violations of the inverse-square law.

6.1 Analysis Procedures

Each data run (about one day in length) was characterized by a definite vertical separation and horizontal offset. Data points were recorded 32 (68) times per free torsional oscillation in Experiment I (II), corresponding to sampling interval of ~ 11 s (7 s). The pendulum's average period of free oscillations was $\tau_\circ = 399.7$ s (467.0 s). The resonance was sharp, the quality factor, $Q = \pi\tau_d/\tau_\circ$, being about 1500. We rotated the attractor at a period of $\tau_{att} = 17\tau_\circ$ ($15\tau_\circ$), making the fundamental 10ω signal occur once every 1.7 (1.5) torsion cycles, while the 20ω signal had a period of $1.7\tau_\circ/2$ ($1.5\tau_\circ/2$), etc. These frequencies were sufficiently far from the resonance to not excite torsional motion. The fundamental signal was also of high enough frequency to suppress the 1/f noise arising from internal friction in the torsion fiber. The twist from the higher harmonics was suppressed by the pendulum inertia; therefore, we only included signals up to 30ω (20ω) in our analysis (higher harmonics were attenuated below the noise level).

We fitted the autocollimator output with harmonic and polynomial terms to ex-

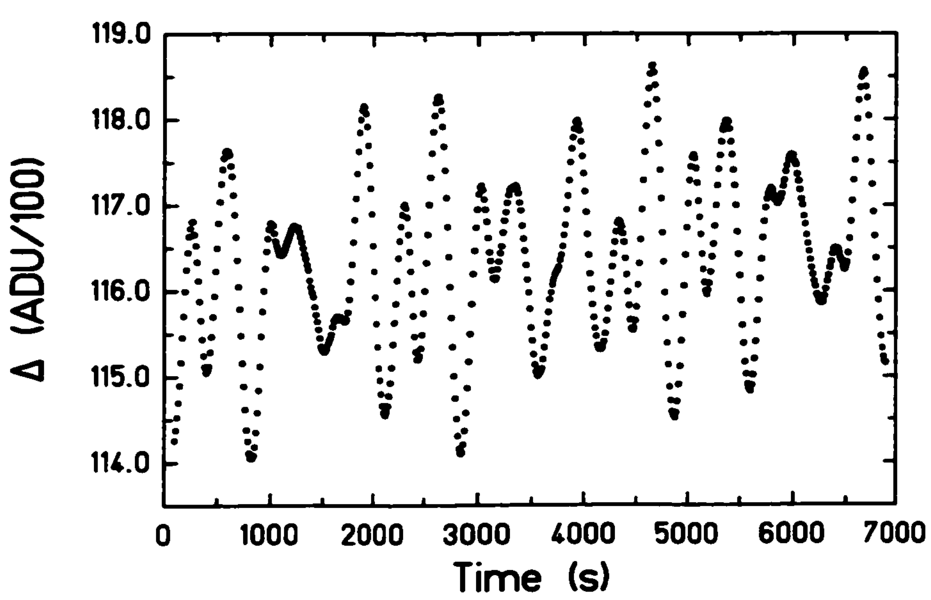

Figure 6.1: Raw Δ autocollimator signal for one complete revolution of the attractor in Experiment I at a vertical pendulum-to-attractor separation of 237 μm. The vertical axis has units of ADU, set by the analog-to-digital conversion electronics. The beating of the various harmonic components, along with the fiber drift, is evident in the data.

tract the pendulum twist (as well as the fiber drift). We then removed bad sections of data and applied frequency-dependent corrections (see Section 6.1.6) based on known mechanical and electronic properties of the system, thus converting the observed twist to the true torque.

6.1.1 Raw Data

All data points were recorded in ADUs and converted to physical units in the analysis, as described in Sections 4.2.1 and 2.10. We called the unconverted data "raw." A sample of raw Δ autocollimator data is shown in Figure 6.1.

6.1.2 Torsion Filtering and Period Correction

The free torsional motion was the dominant harmonic component of the pendulum's twist. Since this motion did not provide information about an inverse-square law violation, we applied a digital filter to suppress the free oscillations before proceeding with the analysis.

This "notch" filter averaged two data points separated by one half of a torsional period, and assigned the average value to their midpoint. For maximum effectiveness of the filter, the torsion period had to be known precisely. We fitted the torsion period for each run (see Figure 4.1) and filtered using the result. The filter linearly interpolated the raw values when a data point did not lie at the exact required time. Thus, the filtered twist for time t was given by

$$\theta_f(t) = \frac{1}{2}\left[\theta_{raw}\left(t - \frac{\tau_\circ}{4}\right) + \theta_{raw}\left(t + \frac{\tau_\circ}{4}\right)\right], \tag{6.1}$$

where θ_{raw} is the interpolated value of the twist and $\tau_\circ$ now refers to the fitted period. Figure 6.2 shows the data of Figure 6.1 after the application of this filter.

6.1.3 Cutting and Fitting of Data

Each data run was subdivided into separate "cuts" that contained exactly two oscillations of the 10ω signal (72° of attractor rotation). For each cut the filtered twist was fitted as a function of attractor angle ϕ with

$$\theta_{fit}(\phi) = \sum_n [b_n \sin(n\phi) + c_n \cos(n\phi)] + \sum_{m=0}^{2} d_m P_m, \tag{6.2}$$

where the first sum ran over n =1, 3, 10, 20, 30 (the n =30 term was not used in Experiment II). The floating b_n and c_n coefficients for the n = 10, 20, and 30 terms yielded the desired harmonic components of the torque. The small n =1 and n =3 terms were fixed by fitting data covering one complete revolution of the attractor.

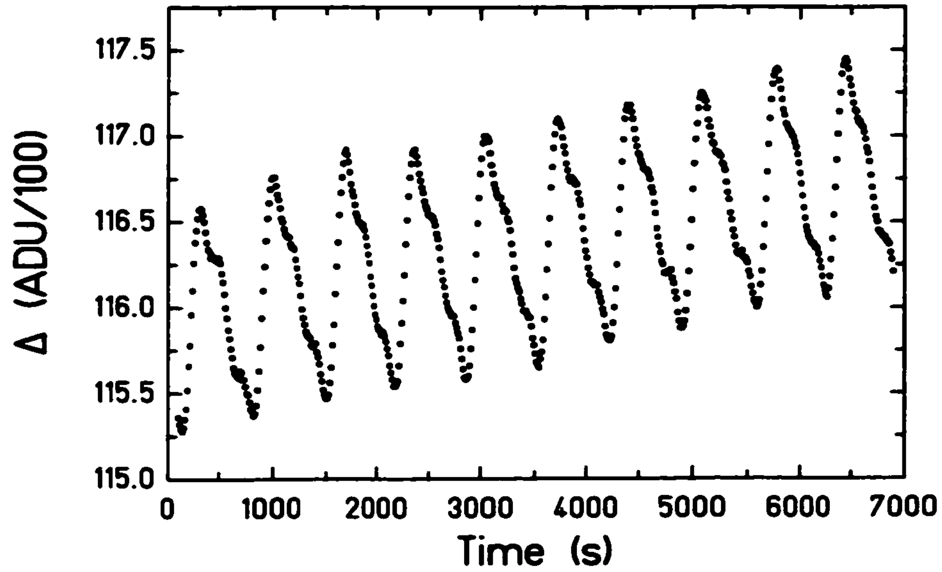

Figure 6.2: The data of Figure 6.1 after applying the notch filter of Equation 6.1.

(The $n = 3$ coefficients accounted for the three-fold symmetry of the attractor drive system while the $n = 1$ coefficients were typically consistent with zero and were used to diagnose any effect periodic at the attractor rotation frequency.) The d_m coefficients of the Legendre polynomials, P_m, accounted for the fiber drift. Figure 6.3 shows the filtered data with the corresponding fit and residuals for one cut. We see that the fit describes the data well. Figure 6.4 shows the data and fit for a complete attractor revolution. The ten oscillations of the fundamental are clearly apparent.

The top panel of Figure 6.5 shows a Fourier spectrum of the pendulum twist from an Experiment I data run. We see the harmonic peaks as well as the torsional mode (this data has not been passed through the torsion filter). The effect of the pendulum as a low-pass filter is seen by the drop in the noise floor above the resonance at 17ω. The smooth curve shows the thermal noise prediction [33] from damping internal to the torsion fiber and a 'white' digitizing noise floor. The spectrum follows the curve

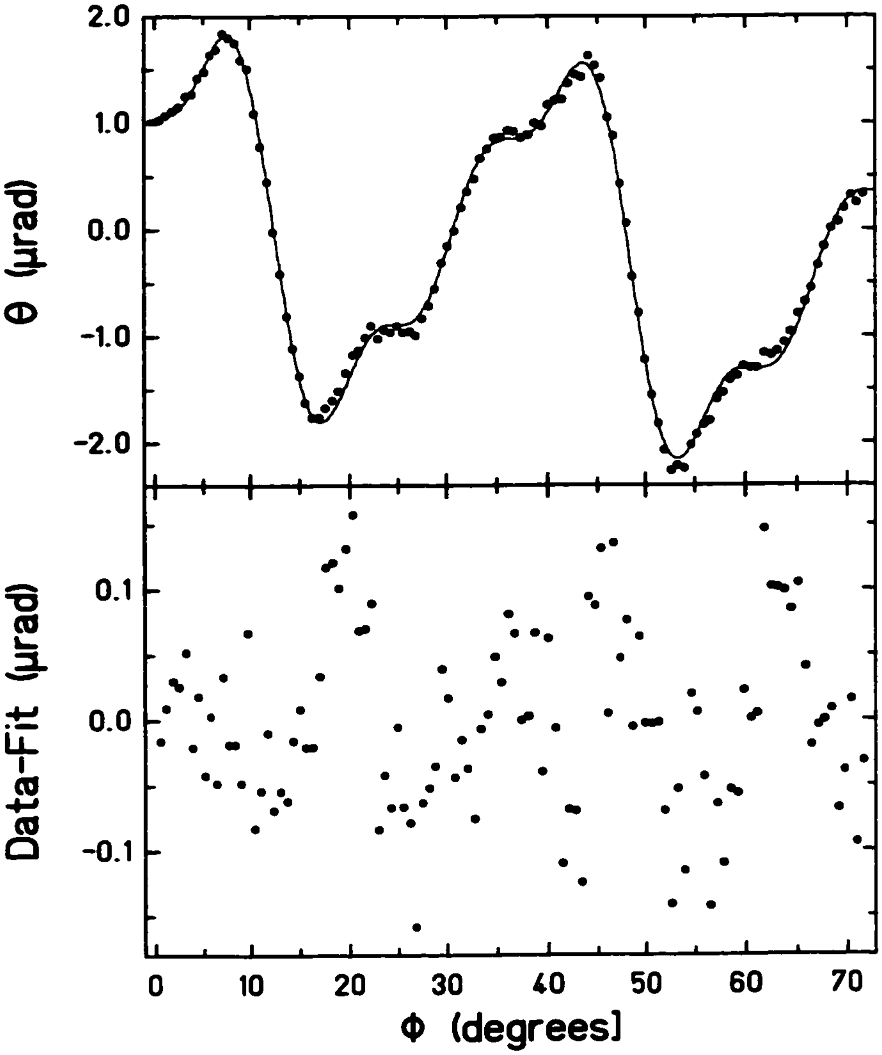

Figure 6.3: Data for one cut at a pendulum-to-attractor separation of 237 μm from Experiment I. The fit is shown as the solid line. The bottom panel displays the fit residuals. We clearly see the two cycles of the 10ω signal, as well as the smaller contributions of the higher harmonics.

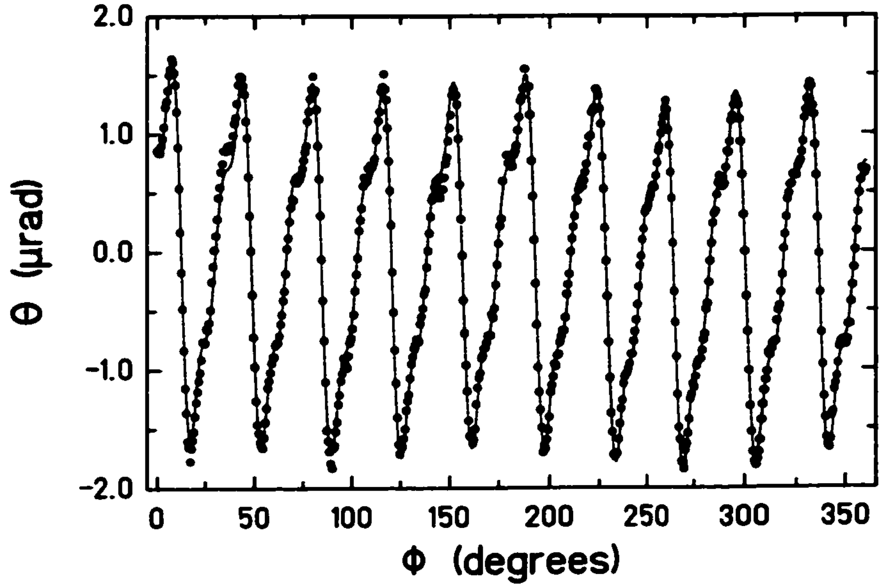

Figure 6.4: Data and fit for one complete attractor revolution (five cuts) at a vertical separation of 237 μm in Experiment I. The ten oscillations arise from the tenfold rotational symmetry of the instrument. The asymmetric shape of the oscillations is due to the higher harmonics; the 10ω frequency is below the pendulum's resonance, while the harmonics lie above it. The resulting phase shifts account for the asymmetric shape.

well, indicating that we were operating near the thermal limit. It is interesting to note that velocity damping (from residual gas, for example) is negligible as it would produce a white as opposed to 1/f background at low frequencies. The bottom panel displays the spectrum when the pendulum's position was held fixed. We see that the angle readout noise was well below the total noise level of an actual data run. We were therefore limited by "torque noise" associated with actual movement of the pendulum.

6.1.4 Rejecting Bad Cuts

Selection criteria were used to determine whether an individual cut was included in the final analysis. Sources of bad cuts included seismic disturbances, ion pump pressure spikes, and spontaneous unwinding of the torsion fiber ("fiber quakes"). These disturbances caused three visible effects upon which we based our rejection criteria. The disturbances could be recognized by a change in the free oscillation amplitude or phase, a high χ^2 value of the fit, or direct observation of an abnormal sensor value.

We measured the free oscillation amplitude for each cut. We then monitored the difference in this amplitude (and phase) between adjacent cuts. We called any difference a "jump" in the free oscillation amplitude. If the jumps of size J were distributed as a gaussian about some mean, nonzero value, the jump distribution would have the form (for M independent gaussian noise sources)

$$N(J) = \sum_{i=1}^{M} N_i \left(\frac{J\, e^{(-J^2/\sigma_i^2)}}{\sigma_i} \right), \tag{6.3}$$

where N_i are normalization constants, and σ_i represent the widths of the distributions. This is the polar form of a gaussian distribution. Jumps well described by this function must come from a stochastic background source, such as random seismic disturbances.

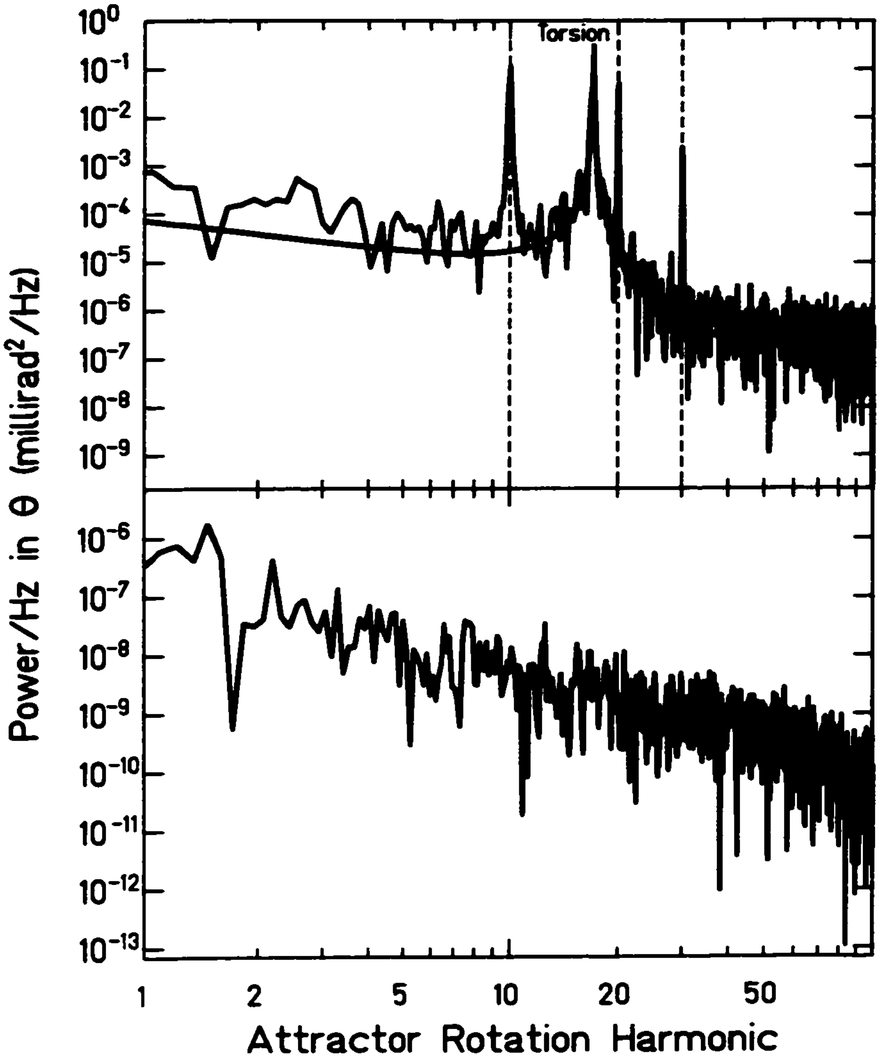

Figure 6.5: Top: Fourier spectrum of the pendulum twist from an Experiment I data run. The horizontal axis is displayed in units of attractor rotation harmonic. The 10ω, 20ω, and 30ω signals are easily recognizable. The free torsional motion at 17ω is also apparent. The smooth curve shows the predicted thermal noise plus a white digitizing noise floor. Bottom: spectral density recorded with the pendulum held stationary. We see the noise level associated with the optical readout is much lower than the "torque noise." The stationary data was taken using a lock-in scale that increased the sensitivity by a factor of 20; hence, wee see that the noise floor at high frequencies is lower by a factor of $\gtrsim 400$ for this data.

The sum indicates the possibility of several such stochastic sources such as separate vertical and horizontal seismic processes. We fitted our measured jump distribution using Equation 6.3 with $M = 2$ ($M = 1$ yielded a poor fit) and let the parameters σ_i and N_i float freely. The jumps were separated into 30 bins; the fit included all but the last bin of data and was in excellent agreement, with a χ^2 per degree of freedom of 0.47 (0.53) for Experiment I (II). The data and fit for the entire Experiment I data set are shown in Figure 6.6. We were interested in removing cuts with large jumps not describable by stochastic processes. We manually chose a cut rejection level by inspecting the point at which the fit began to deviate significantly from the data. Our level of 2.4 μrad is shown by the vertical dotted line in Figure 6.6; cuts with larger associated jumps were not included in the final analysis. The cut rejection level, using the same analysis, for Experiment II was 1.2 μrad. This decrease represented the fact that the magnetic damper/prehanger assembly in Experiment I was not functioning properly; thus, larger seismically induced jumps were present.

Our next rejection criterion was the χ^2 distribution of the individual cuts. It should be noted that the χ^2 values for the fits of the individual cuts had an arbitrary normalization set by assuming an error of ±1 ADU on every recorded point. Again, if our noise was gaussian, we would expect the χ^2 values to be distributed as [32]

$$N(\chi^2) \approx \sum_{i=1}^{M} N_i \left(\frac{(\chi^2)^{(\delta_i/2-1)}\, e^{(-\chi^2/2)}}{(2^{\delta_i/2})\, \Gamma(\frac{\delta_i}{2})} \right), \tag{6.4}$$

where δ_i are the degrees of freedom of the distributions, Γ is the gamma function, and again, N_i are normalization constants. Once more we fit 29 bins of data with $M = 2$, and left N_i and δ_i completely free. We used $M = 2$ to approximate the effect of the jump distribution on the χ^2 distribution (a large jump in a cut will result in a large value of χ^2 for that cut). The fit was again good, with a χ^2 per degree of freedom of 0.94 (1.34) for Experiment I (II). The rejection level was selected to reject

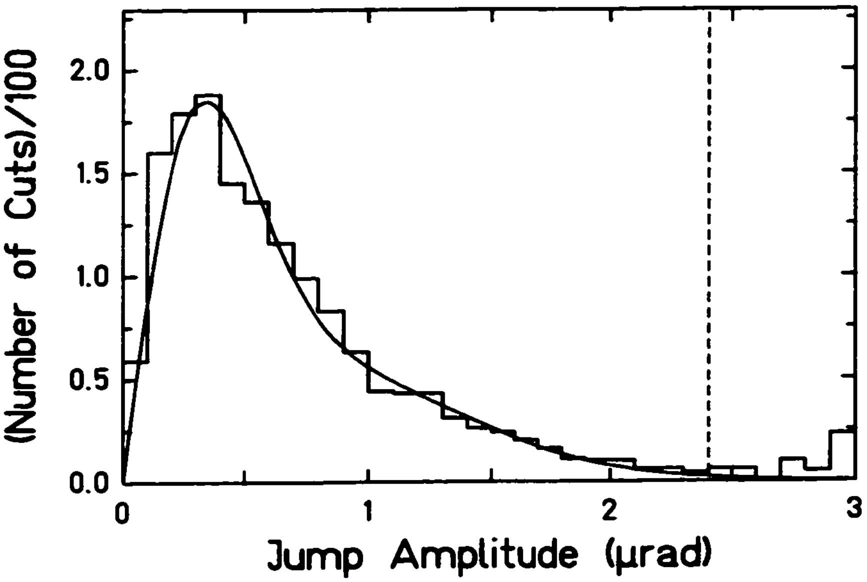

Figure 6.6: Distribution of jumps in the free oscillation amplitude between adjacent cuts for Experiment I. The curve is a good fit to the assumption that the jump size is gaussianly distributed with two independent sources. The vertical dashed line represents the cut rejection level we used. Larger jumps are due to non-random events such as small earthquakes, pressure spikes, or spontaneous unwinding of the torsion fiber. Note that in thermal equilibrium the mean free oscillation amplitude is $\theta_m = \sqrt{k_B T/\kappa} = 1.1$ μrad, where k_B is Boltzmann's constant.

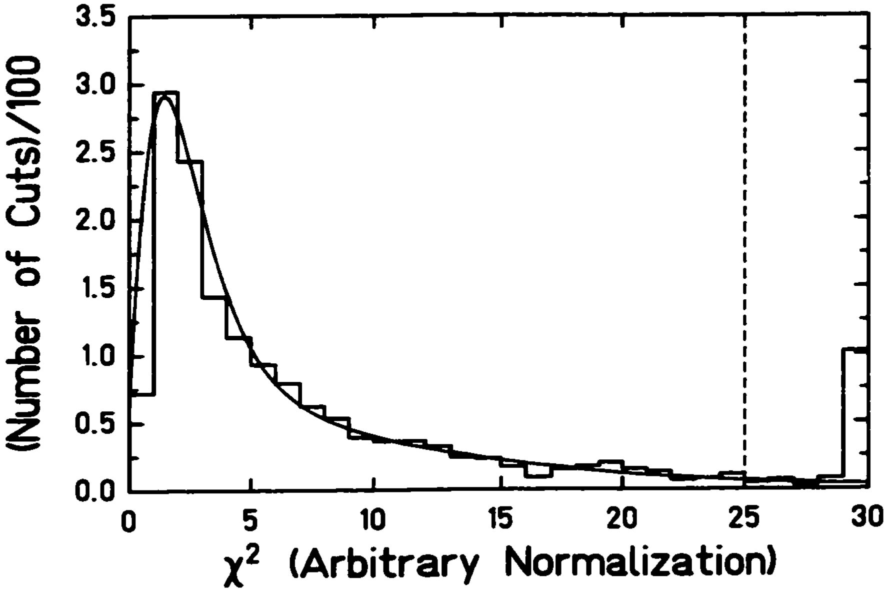

Figure 6.7: Distribution of χ^2 values for all 1599 cuts in Experiment I. The curve is a fit to the function given in Equation 6.4 with $M = 2$. The quality of the fit indicates that the noise was white for the included data. The dashed vertical line is the cut rejection level.

any cut with a χ^2 greater than 25 (14). The χ^2 distribution and fit for Experiment I are shown in Figure 6.7.

The final rejection criterion was a direct observation of an abrupt disturbance of a sensor. Since many disturbances would cause an associated jump in the free oscillation amplitude or bad χ^2 value, this criterion was mostly a consistency check. The only observable sensor irregularities were spikes in the vacuum chamber pressure; the pendulum was often torsionally excited when there was a large ion pump pressure spike (see Figure 6.8). We rejected any cut that contained pressure values greater than the mean value plus ten times the standard deviation for that run.

In summary, the jump and χ^2 criteria ensured that the included cuts had gaussianly distributed noise. The ion pump spike test was a consistency check that also

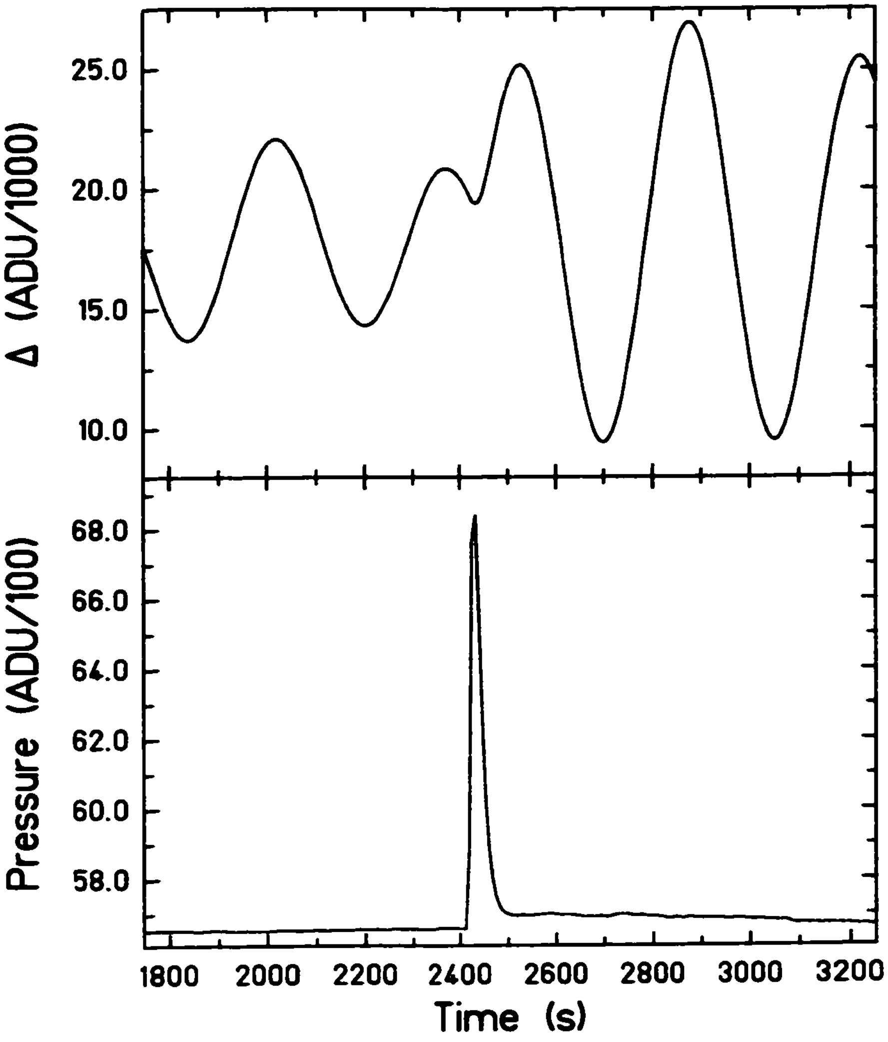

Figure 6.8: The effect of a pressure spike on the pendulum twist. The upper panel shows the pendulum twist, the lower the simultaneous value of the pressure. At the time of the spike we see a sudden excitation of the pendulum amplitude.

allowed for direct removal of certain cuts if the other procedures failed. In Experiment I (II), we rejected 227 (26) out of a total of 1599 (676) cuts.

6.1.5 Combining "Good" Data

The cuts which survived the rejection criteria were treated as equivalent within a run so that for an individual run with N cuts, the mean twist coefficients and their uncertainties were

$$\bar{b}_n = \frac{1}{N}\sum_{i=1}^{N} b_n(i) \tag{6.5}$$

$$\sigma_{b_n} = \sqrt{\frac{1}{N(N-1)}\sum_{i=1}^{N}(b_n(i) - \bar{b}_n)^2}, \tag{6.6}$$

where these equations apply to all coefficients b_n and c_n of Equation 6.2. Figure 6.9 shows the distribution of b_{10} coefficients for a single run. The mean and uncertainty are shown by the dotted and solid lines, respectively.

6.1.6 Frequency Response and Averaging Corrections

To extract the torque from the observed twist of Equation 6.2 we applied frequency-dependent corrections based on the mechanical resonance of the pendulum, electronic time constants, and attenuation from the torsion filter. These corrections were applied to the mean values and uncertainties of the coefficients determined by Equations 6.5 and 6.6 for each run.

The differential equation describing the twist of the pendulum subjected to a driving torque T is

$$I\ddot{\theta} + 2I\gamma\dot{\theta} + \kappa\theta = T, \tag{6.7}$$

where I is the pendulum's moment of inertia about the fiber axis, κ is the torsion

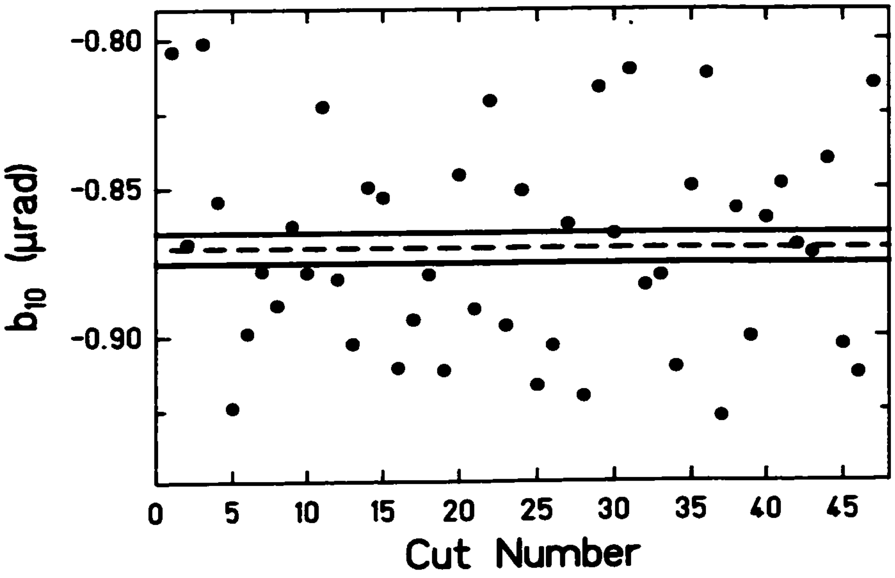

Figure 6.9: Values of b_{10} for 47 cuts within one data run. The horizontal lines represent the mean (dotted) and uncertainty (solid) as defined by Equations 6.5 and 6.6.

constant,[1] θ is the twist angle, and $\gamma = 1/\tau_d$ is the inverse of the exponential decay time of the pendulum amplitude. If we have a periodic driving torque given by $T = T_o e^{i\omega t}$, the steady-state solution is

$$\theta(t) = \left(\frac{\omega_0^2}{\omega_0^2 - \omega^2 + 2i\omega\gamma}\right)\frac{T_0}{\kappa}e^{i\omega t}, \tag{6.8}$$

where $\omega_0 = \sqrt{\kappa/I}$ is the resonant angular frequency. Equation 6.8 can be written as an amplitude correction, A_p, and phase shift, Φ_p, applied to the motion of a inertia-less pendulum ($\theta = \frac{T}{\kappa}$) as

$$\theta(t) = A_p\left[\frac{T_0}{\kappa}\sin(\omega t + \Phi_p)\right], \tag{6.9}$$

---

[1] It has since been noted that κ should be replaced by $\kappa(1 + i\phi)$ to account for damping internal to the torsion fiber. However, for our analysis the effect was negligible.

where

$$A_p = \left[\left(1 - \frac{\omega^2}{\omega_0^2}\right)^2 + \left(\frac{2\gamma\omega}{\omega_0^2}\right)^2\right]^{-\frac{1}{2}} \tag{6.10}$$

$$\Phi_p = \tan^{-1}\left(\frac{-2\gamma\omega}{\omega_0^2 - \omega^2}\right). \tag{6.11}$$

This correction was applied only to the pendulum twist, not to the other sensors.

The next correction was due to the torsion filter described in Section 6.1.2. Consider its effect on a sinusoidally varying twist of period $\mathcal{T}$, amplitude A, and phase ϕ:

$$\theta_f(t) = \frac{1}{2}\left[A\sin\left(\frac{2\pi}{\mathcal{T}}t + \phi - \frac{\pi\tau_0}{2\mathcal{T}}\right) + A\sin\left(\frac{2\pi}{\mathcal{T}}t + \phi + \frac{\pi\tau_0}{2\mathcal{T}}\right)\right], \tag{6.12}$$

which simplifies to

$$\theta_f(t) = A\left[\cos\left(\frac{\pi\tau_0}{2\mathcal{T}}\right)\right]\sin\left(\frac{2\pi}{\mathcal{T}}t + \phi\right). \tag{6.13}$$

So we see the filter reduces the amplitude by a factor

$$A_f = \cos\left(\frac{\pi\tau_0}{2\mathcal{T}}\right), \tag{6.14}$$

without introducing a phase shift, $\Phi_f = 0$.

The 2-pole filters on the Δ and Σ lock-in amplifiers also attenuated and phase shifted the signal. The amplifiers averaged the twist over the measured time constant $t_c = 10.0966 \pm 0.0002$ s. This time constant was measured by producing a step pulse at the lock-in amplifier input and measuring the exponential decay of its output. According to the derivation in [34], this averaging induces amplitude and phase factors

$$A_l = \frac{1}{1 + (\frac{2\pi}{\mathcal{T}}t_c)^2} \tag{6.15}$$

$$\Phi_l = -2\tan^{-1}\left(\frac{2\pi}{\mathcal{T}}t_c\right). \tag{6.16}$$

The true torque on the pendulum may now be related to the fitted values:

$$T = \kappa\theta_{cor} = \frac{\kappa\theta_{fit}}{A_p \cdot A_f \cdot A_l} \tag{6.17}$$

with a phase of

$$\phi = \phi_{fit} - \Phi_p - \Phi_l. \tag{6.18}$$

These expressions may be simplified and put in terms of the fitted coefficients b_n and c_n to get the amplitudes of the harmonic components of the torque

$$|T_n| = \kappa_\circ \left| (\tilde{b}_n + i\tilde{c}_n) \frac{(\omega_\circ^2 - n^2\omega^2 + 2i\gamma n\omega)}{\omega_\circ^2} \right| \times \sec\left(\frac{\pi n\omega}{2\omega_\circ}\right), \tag{6.19}$$

where $\tilde{b}_n$ and $\tilde{c}_n$ refer to the coefficients corrected for the lock-in averaging, and we took $\kappa_\circ = 0.0317$ erg/rad.

6.2 Experiment I Data

The data from Experiment I contained 27 runs, each of which contained at least 36 cuts. The data was collected over a period of $\sim$45 days. Several runs were taken with the upper attractor disk alone. Due to the holder design, these single-disk runs all had vertical separations > 8 mm. We fitted only the 10ω component for these runs due to the negligible size of the higher harmonics.

6.2.1 On-Center Runs

The full range of vertical separations was 218 μm to 10.78 mm, including the upper-disk-only runs. The measured harmonic components of the torque as a function of separation are shown in Table 6.1. Because the phase of the signals should be invariant under vertical translation, we chose the phase such that each torque harmonic was described by a single coefficient (b_{10} for example). Thus, the sign change of T_{10} at a separation of $\sim$2 mm represents a complete phase reversal (for T_{10} this corresponds to a phase change of $\pi/10$). At this point the torque from the lower attractor plate overcomes that of the upper (remember that the lower holes are relatively out of phase).

Table 6.1: Harmonic torque components from the on-center data in Experiment I. All torques have units of 10^{-9} dyne-cm, and the (*) refers to upper-disk-only runs for which we fitted only the 10ω component.

Separation (mm)	T_{10}	T_{20}	T_{30}
0.218	54.968 ± 0.545	24.274 ± 0.416	29.662 ± 0.330
0.237	54.623 ± 0.254	23.613 ± 0.170	28.876 ± 0.249
0.384	46.192 ± 0.333	20.649 ± 0.272	24.230 ± 0.374
0.579	38.529 ± 0.466	17.276 ± 0.323	18.970 ± 0.269
1.068	21.114 ± 0.432	10.844 ± 0.327	10.902 ± 0.348
1.557	10.035 ± 0.544	6.625 ± 0.448	6.262 ± 0.487
2.045	1.285 ± 0.312	4.196 ± 0.218	3.959 ± 0.365
3.023	-7.725 ± 0.419	2.339 ± 0.236	1.437 ± 0.388
4.000	-10.016 ± 0.364	0.609 ± 0.332	0.463 ± 0.343
4.978	-10.636 ± 0.269	0.676 ± 0.290	-0.179 ± 0.482
6.444	-9.362 ± 0.433	0.568 ± 0.300	0.007 ± 0.430
8.137*	52.046 ± 0.489	N/A	N/A
8.137*	51.650 ± 0.682	N/A	N/A
8.137*	51.469 ± 0.482	N/A	N/A
8.821*	39.605 ± 0.600	N/A	N/A
8.821*	39.537 ± 0.683	N/A	N/A
10.776*	18.873 ± 0.259	N/A	N/A
10.776*	18.389 ± 0.428	N/A	N/A

Table 6.2: Harmonic torque components for all off-center runs in Experiment I. The labels X and Y refer to positions along the two perpendicular stage axes. Again, all torques are in units of 10^{-9} dyne-cm.

X (mm)	Y (mm)	T_{10}	T_{20}	T_{30}
Vertical Separation = 237 μm				
0.938	-0.035	45.497 ± 0.244	18.699 ± 0.169	19.932 ± 0.303
-1.015	-0.035	44.242 ± 0.708	18.489 ± 0.467	18.989 ± 0.326
-0.038	0.941	45.792 ± 0.488	18.395 ± 0.340	19.906 ± 0.367
-0.038	-0.523	51.648 ± 0.269	22.289 ± 0.279	26.106 ± 0.272
Vertical Separation = 2.045 mm				
1.451	-0.017	-4.038 ± 0.395	2.838 ± 0.409	1.082 ± 0.413
Vertical Separation = 4.000 mm				
1.451	-0.017	-12.028 ± 0.826	-0.617 ± 4.701	3.280 ± 3.299
-1.479	-0.017	-11.865 ± 0.385	2.211 ± 1.633	-1.246 ± 2.190
-0.014	1.447	-11.061 ± 0.466	-5.129 ± 4.263	0.189 ± 1.969
-0.014	-0.748	-10.789 ± 0.236	1.814 ± 1.613	1.087 ± 1.776

6.2.2 Centering Runs

Several runs were taken at varying horizontal offset to determine the unknown alignment point. The data from the centering runs is shown in Table 6.2.

6.3 Experiment II Data

The data for Experiment II contained 17 runs, each of which contained at least 19 cuts. Six of these runs were used for horizontal centering, but we did not use them to constrain a violation of the inverse-square law because the relative calibration setup

Table 6.3: Harmonic torque components for the on-center data runs of Experiment II in units of 10^{-9} dyne-cm.

Separation (mm)	T_{10}	T_{20}
0.138	323.762 ± 3.122	103.686 ± 0.762
0.138	322.974 ± 0.851	103.798 ± 0.303
0.163	317.619 ± 1.030	101.686 ± 0.343
0.192	310.960 ± 0.851	99.579 ± 0.301
0.373	272.348 ± 0.549	86.484 ± 0.227
0.764	203.144 ± 0.580	63.667 ± 0.261
1.546	103.529 ± 0.384	34.667 ± 0.214
3.012	10.092 ± 0.214	10.966 ± 0.169
3.696	-9.933 ± 0.135	6.787 ± 0.159
5.456	-29.174 ± 0.167	1.890 ± 0.099
7.899	-25.729 ± 0.204	0.579 ± 0.111

was not operated for these runs. The entire data set was collected over a period of ~ 30 days.

6.3.1 On-Center Runs

The full range of vertical separations was 138 μm to 7.90 mm. The measured harmonic components of the torque as a function of separation are shown in Table 6.3. Again, we see the phase reversal of T_{10}, now at a separation of ~ 3.3 mm.

Table 6.4: Harmonic torque components for the off-center data runs of Experiment II in units of 10^{-9} dyne-cm.

Vertical Separation = 217 μm

X (mm)	Y (mm)	T_{10}	T_{20}
-0.156	-0.205	304.668 ± 0.143	97.073 ± 0.092
1.797	-0.205	210.352 ± 0.150	54.799 ± 0.134
-2.110	-0.205	173.220 ± 0.166	40.058 ± 0.119
-0.156	-1.961	189.899 ± 0.236	46.151 ± 0.166
-0.156	1.747	215.697 ± 0.192	56.313 ± 0.129
0.000	0.000	305.669 ± 0.532	97.853 ± 0.259

6.3.2 Centering Runs

As in Experiment I, several runs were taken at varying horizontal offsets to determine the unknown alignment point to within the acceptable ±100 μm region. The data from a set of centering runs with a vertical pendulum-to-attractor separation of 217 μm is shown in Table 6.4.

Chapter 7

RESULTS: CONSTRAINTS ON YUKAWA INTERACTIONS

We constrained violations of the inverse-square law by comparing the measured torques, described in the previous chapter, to predictions, described in Chapter 5, of the expected Newtonian and possible Yukawa torques. The predicted torques, of course, were functions of the instrumental parameters such as the missing mass of the holes, the pendulum-to-attractor vertical separation, etc. The complete data sets for each experiment were fitted to these functions using a χ^2 minimization.

7.1 Instrumental Parameter Values

All of the instrumental parameters except for the horizontal center positions, x_0 and y_0, were taken, with their errors, from independent measurements described in Chapter 4. The measured error associated with each parameter was taken into account as a constraint in the χ^2 minimization. The superscripts 'I' and 'II' are used to distinguish parameters that had different values for the two data sets.

7.2 Comparison of Data Sets to the Newtonian Predictions

To compare our data with the prediction of Newtonian gravity, we fitted the data without including the Yukawa parameters; that is, we fixed $\alpha = 0$.

7.2.1 Experiment I

The fitting function we used to compare the data (we denote the separate runs by the index i) with the calculated torque predictions for Experiment I had the form (with $\rho^I(i) = \sqrt{(x(i) - x_o^I)^2 + (y(i) - y_o^I)^2}$)

$$\begin{aligned} T_n^I(i) \;=\; & C^I\,[T^G_{(up,I)}(n,\ \rho^I(i),\ z(i) - z_o^I) \\ & + R_1^I\,T^G_{(low,I)}(n,\ \rho^I(i),\ z(i) - z_o^I + \delta z^I) \\ & + \alpha(T^Y_{(up,I)}(n,\ \rho^I(i),\ z(i) - z_o^I,\ \lambda) \\ & + R_1^I\,T^Y_{(low,I)}(n,\ \rho^I(i),\ z(i) - z_o^I + \delta z^I,\ \lambda))], \end{aligned} \tag{7.1}$$

where n is the attractor rotation harmonic, C^I represents the overall torque scale factor, R_1^I is the relative torque scale factor for the lower disk, $(x(i), y(i), z(i))$ are the coordinates of the pendulum relative to the attractor for a single run, x_o^I and y_o^I are the horizontal alignment points, z_o^I is the value of z at vanishing pendulum-to-attractor separation, δz^I is the gap between the upper and lower attractor disks, T^G and T^Y are the calculated torque functions of Chapter 5, and, again, we set $\alpha = 0$ for the Newtonian fit. These parameters were determined by the methods described in Chapter 4 (see Table 4.6). The upper-disk-only runs were fitted simultaneously with

$$T_n^{up}(i) = C^I[T^G_{(up,I)}(n,\ \rho^I(i),\ z(i) - \zeta^I) + \alpha\,T^Y_{(up,I)}(n,\ \rho^I(i),\ z(i) - \zeta^I,\ \lambda)], \tag{7.2}$$

where ζ^I is a separate parameter representing the z position at vanishing pendulum-to-upper disk separation. The fit for Newtonian gravity alone was good, having $\chi^2/\nu = 0.77$ ($\nu = 65$ and $P(\chi^2,\ \nu) = 0.91$), and the best fit values of the parameters were all within 2 standard deviations of their measured values. Table 7.1 displays the measured and fitted values of the parameters. Figure 7.1 shows the Newtonian fit to the runs with a horizontal offset at a vertical separation of 237 μm, and the top

Table 7.1: Comparison of the measured and fitted experimental parameters for Experiment I. The uncertainty on C^I reflects the uncertainty in the hole masses and the overall scale factor.

Parameter	Measured Value	Fitted Value
C^I	1.027 ± 0.025	1.063 ± 0.005
R_1^I	1.0000 ± 0.0013	0.9996 ± 0.0013
$x_\circ^I$	N/A	-0.015 ± 0.009 mm
$y_\circ^I$	N/A	-0.018 ± 0.012 mm
$z_\circ^I$	0.000 ± 0.005 mm	0.000 ± 0.004 mm
δz^I	0.010 ± 0.010 mm	0.017 ± 0.003 mm
ζ^I	0.000 ± 0.030 mm	0.032 ± 0.015 mm

panel of Figure 7.2 shows the data and Newtonian fit for all of the on-center runs. The bottom panel of Figure 7.2 shows the residuals of the Newtonian fit and the effect a Yukawa interaction with $\alpha = 3$ and $\lambda = 0.250$ mm would have on the T_{10} component. The data is inconsistent with such a deviation.

7.2.2 Experiment II

The fitting function for the Experiment II data set had a similar form (with $\rho^{II}(i) = \sqrt{(x(i) - x_\circ^{II})^2 + (y(i) - y_\circ^{II})^2}$):

$$\begin{aligned} T_n^{II}(i) \;=\; & C^{II}\,[T^G_{(upin,II)}(n,\ \rho^{II}(i),\ z(i) - z_\circ^{II}) \\ & + R_1^{II}\,T^G_{(upout,II)}(n,\ \rho^{II}(i),\ z(i) - z_\circ^{II}) \\ & + R_2^{II}\,T^G_{(low,II)}(n,\ \rho^{II}(i),\ z(i) - z_\circ^{II} + \delta z^{II}) \\ & + \alpha\,(T^Y_{(upin,II)}(n,\ \rho^{II}(i),\ z(i) - z_\circ^{II},\ \lambda) \\ & + R_1^{II}\,T^Y_{(upout,II)}(n,\ \rho^{II}(i),\ z(i) - z_\circ^{II},\ \lambda) \\ & + R_2^{II}\,T^Y_{(low,II)}(n,\ \rho^{II}(i),\ z(i) - z_\circ^{II} + \delta z^{II},\ \lambda))], \end{aligned} \tag{7.3}$$

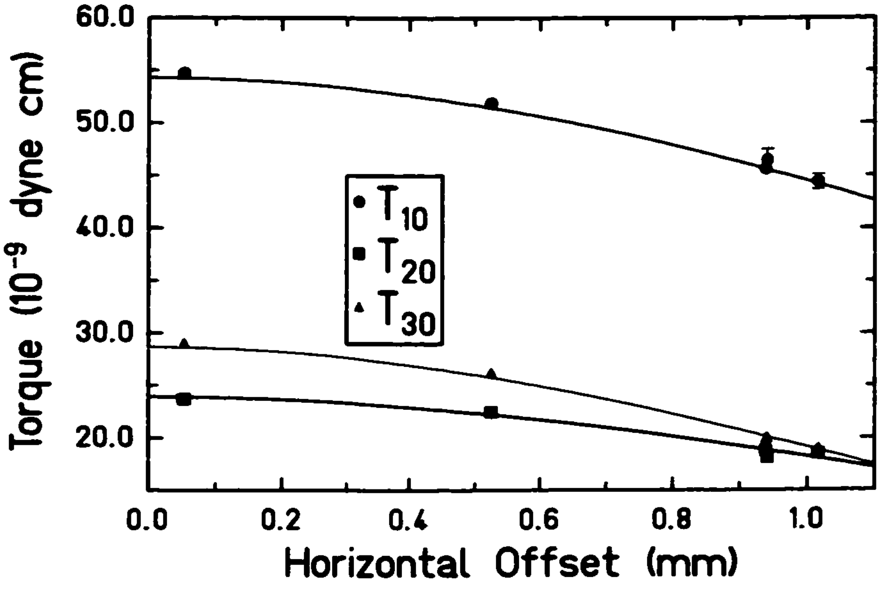

Figure 7.1: Centering data with Newtonian fit for Experiment I. For clarity, we show only the magnitude of the offset.

where the superscripts, II, indicate quantities specific to Experiment II. The Newtonian fit for this data set was also good, the $\chi^2/\nu = 1.27$ ($\nu = 22$ and $P(\chi^2, \nu) = 0.18$), and the fitted values of the parameters were all again within 2 standard deviations of their measured values. Table 7.2 displays the measured and fitted values of these parameters. Figure 7.3 shows the Newtonian fit to the offset runs at a vertical separation of 218 μm and Figure 7.4 shows the data and Newtonian fit and residuals for all 11 on-center runs with the same Yukawa prediction as in Figure 7.2.

7.2.3 Combined Data from Experiments I and II

We fitted both data sets simultaneously with a function consisting of the sum of the Experiment I and Experiment II functions. The combined fit to Newtonian gravity had $\chi^2/\nu = 0.90$ ($\nu = 87$ and $P(\chi^2, \nu) = 0.73$). The values of the fitted and measured

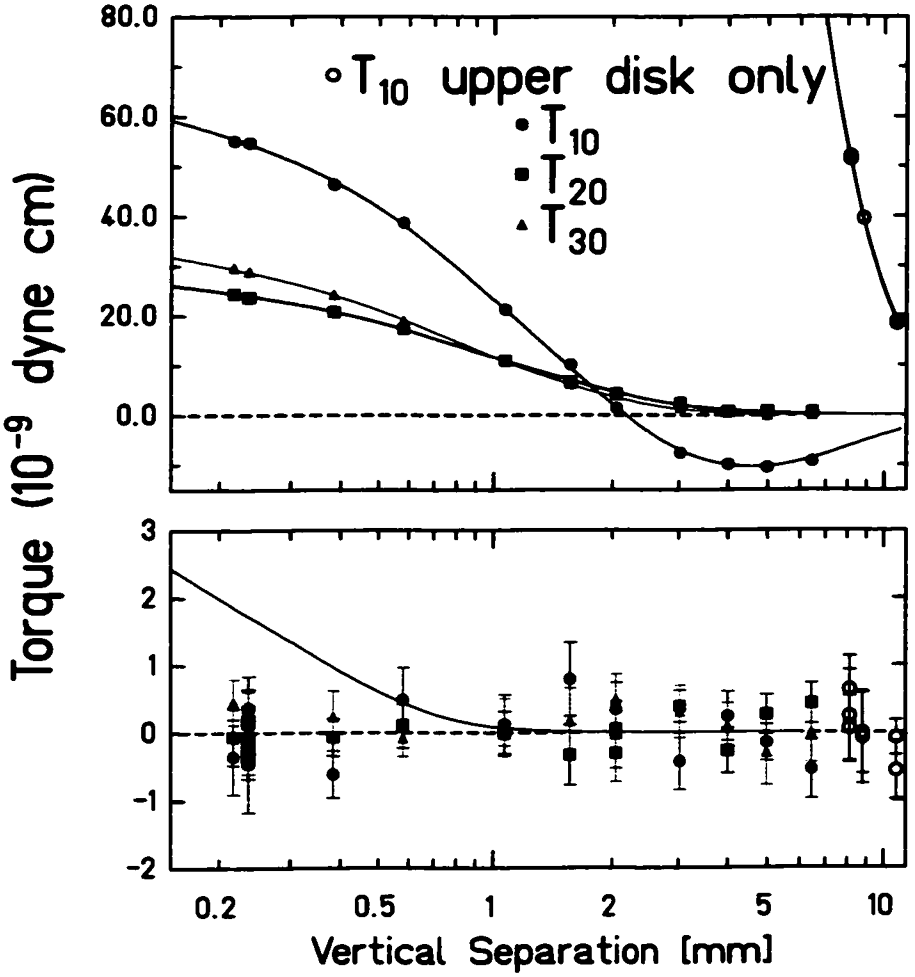

Figure 7.2: Top: data and Newtonian fit for on-center data from Experiment I. The fit agrees well with the data, and all fitted instrumental parameters also agree with their measured values. The lower panel displays the Newtonian residuals; the solid curve shows the effect on T_{10} of a Yukawa interaction of strength α=3 and range λ=0.25 mm. The data is clearly inconsistent with such an interaction.

Table 7.2: Comparison of the measured and fitted experimental parameters for Experiment II.

Parameter	Measured Value	Fitted Value
C^{II}	1.0284 ± 0.0005	1.0283 ± 0.0005
R_1^{II}	1.000000 ± 0.000054	1.000000 ± 0.000054
R_2^{II}	1.000000 ± 0.000048	1.000000 ± 0.000048
x_0^{II}	N/A	0.014 ± 0.008 mm
y_0^{II}	N/A	0.012 ± 0.008 mm
z_o^{II}	0.000 ± 0.005 mm	-0.001 ± 0.002 mm
δz^{II}	0.0014 ± 0.0010 mm	0.0010 ± 0.0010 mm

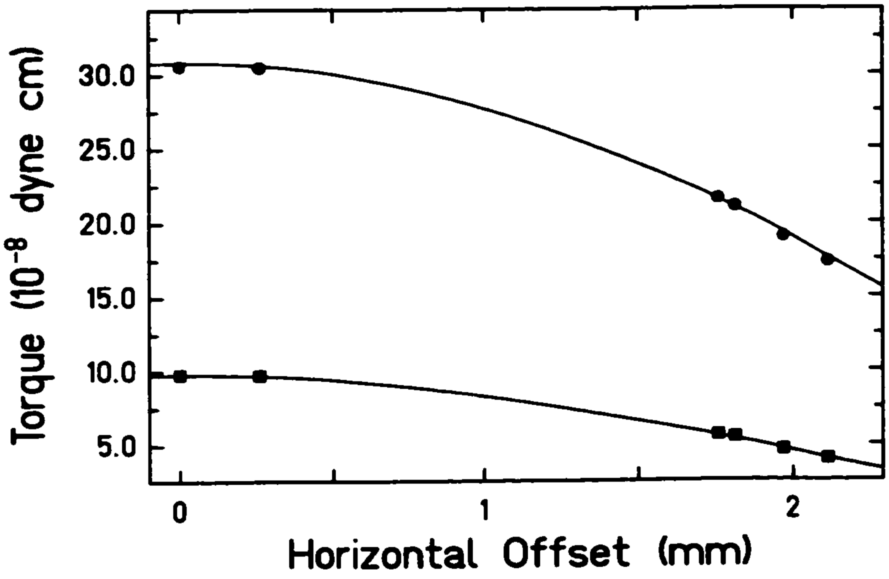

Figure 7.3: Data and Newtonian best fit line for the offset runs in Experiment II. This data was not used to constrain an ISL violation. The circles represent 10ω components, while the squares are the 20ω torque. The horizontal axis is the magnitude of the offset.

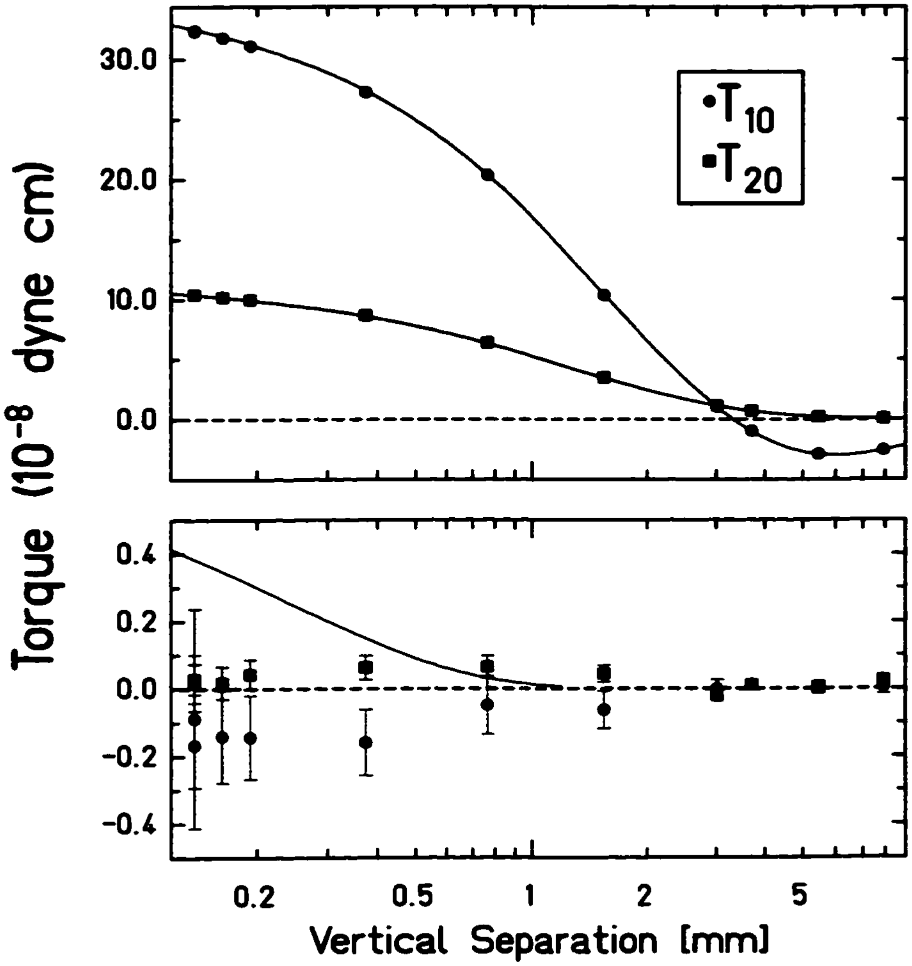

Figure 7.4: Top: on-center data and Newtonian best fit line for Experiment II. Bottom: Newtonian residuals and effect on T_{10} of a Yukawa interaction with $\alpha = 3$ and $\lambda = 0.250$ mm. The error bars increase at small separations (large signals) due to the fractional uncertainty in the measured value of the free torsion period.

Table 7.3: Comparison of the measured and fitted experimental parameters for the combined data set.

Parameter	Measured Value	Fitted Value
C^I	1.027 ± 0.025	1.063 ± 0.005
R_1^I	1.0000 ± 0.0013	0.9996 ± 0.0013
x_0^I	N/A	-0.015 ± 0.009 mm
y_0^I	N/A	-0.018 ± 0.012 mm
z_o^I	0.000 ± .005 mm	0.000 ± 0.004 mm
δz^I	0.010 ± 0.010 mm	0.017 ± 0.003 mm
ζ^I	0.000 ± 0.030 mm	0.032 ± 0.015 mm
C^{II}	1.0284 ± 0.0005	1.0283 ± 0.0005
R_1^{II}	1.000000 ± 0.000054	1.000000 ± 0.000054
R_2^{II}	1.000000 ± 0.000048	1.000000 ± 0.000048
x_0^{II}	N/A	0.014 ± 0.008 mm
y_0^{II}	N/A	0.012 ± 0.008 mm
z_o^{II}	0.000 ± 0.005 mm	-0.001 ± 0.002 mm
δz^{II}	0.0014 ± 0.0010 mm	0.0009 ± 0.0010 mm

parameters for the combined data set are shown in Table 7.3.

7.3 Generation of Constraints

To generate the constraints on a violation of the gravitational ISL, we used the full fitting functions including the Yukawa terms. We generated constraints for each experiment individually as well for the combined data set.

7.3.1 Technique

We fitted the data for each experiment, as well as the combined set, for 24 fixed values of λ between 0.020 mm and 10.0 mm. We extracted from each fit the central value α_λ and its 1-σ uncertainty, $\delta\alpha_\lambda$. We then used these values to establish 95% confidence intervals on the allowed values of α, $-\alpha$, and $|\alpha|$. The 95% confidence upper limit on α for each Yukawa range was $\alpha_\lambda + 2\delta\alpha_\lambda$, while the lower limit was $\alpha_\lambda - 2\delta\alpha_\lambda$. To determine the one-sided constraints on $|\alpha|$, we integrated the normal distribution with mean α_λ and width $\delta\alpha_\lambda$, $N(\alpha_\lambda,\ \delta\alpha_\lambda)$, and used as our constraints the value of α'_λ which satisfied the condition

$$\int_{-\infty}^{-\alpha'_\lambda} N(\alpha_\lambda, \delta\alpha_\lambda) + \int_{\alpha'_\lambda}^{\infty} N(\alpha_\lambda, \delta\alpha_\lambda) = 0.05. \qquad (7.4)$$

7.3.2 Constraints on a Yukawa Violation of the ISL

Tables 7.4, 7.5, and 7.6 show the 95% confidence intervals for the 24 different values of λ for each data set, including the combined set. Figure 7.5 (7.6) displays the constraint for Experiment I (II). The combined result is shown in Figure 7.7. These results (which include the Experiment II data) improved upon previous experiments by a factor of up to $\sim 10^4$ and improve substantially upon the overly conservative analysis of the Experiment I data reported in Ref. [35]. In the final chapter, we discuss the implications of these constraints on the various theoretical scenarios described in Chapter 1.

Table 7.4: 95% confidence level constraints from Experiment I.

λ (mm)	α	$-\alpha$	$\lvert\alpha\rvert$
0.020	7.78×10^{7}	7.63×10^{7}	7.71×10^{7}
0.025	1.29×10^{6}	8.26×10^{5}	1.15×10^{6}
0.032	1.06×10^{5}	6.49×10^{4}	9.42×10^{5}
0.040	1.24×10^{4}	7.48×10^{3}	1.10×10^{4}
0.050	1.23×10^{3}	2.18×10^{3}	1.94×10^{3}
0.063	3.46×10^{2}	3.41×10^{2}	3.43×10^{2}
0.080	9.20×10^{1}	6.20×10^{1}	8.25×10^{1}
0.100	2.55×10^{1}	1.87×10^{1}	2.31×10^{1}
0.126	8.02	6.51	7.42
0.158	2.79	2.53	2.67
0.199	1.06	1.06	1.06
0.250	4.27×10^{-1}	4.75×10^{-1}	4.54×10^{-1}
0.314	1.85×10^{-1}	2.23×10^{-1}	2.07×10^{-1}
0.395	8.59×10^{-2}	1.09×10^{-1}	1.00×10^{-1}
0.546	3.39×10^{-2}	4.39×10^{-2}	4.01×10^{-2}
0.754	1.68×10^{-2}	2.04×10^{-2}	1.89×10^{-2}
1.042	1.08×10^{-2}	1.16×10^{-2}	1.12×10^{-2}
1.439	9.34×10^{-3}	8.51×10^{-3}	8.97×10^{-3}
1.988	1.14×10^{-2}	8.29×10^{-3}	1.03×10^{-2}
2.746	1.89×10^{-2}	1.03×10^{-2}	1.68×10^{-2}
3.794	3.30×10^{-2}	1.67×10^{-2}	2.93×10^{-2}
5.241	5.10×10^{-2}	1.79×10^{-2}	4.57×10^{-2}
7.239	6.68×10^{-2}	1.02×10^{-2}	6.08×10^{-2}
10.000	7.87×10^{-2}	2.03×10^{-2}	7.11×10^{-2}

Table 7.5: 95% confidence level constraints from Experiment II. The entries "N/A" indicate that all values of that parameter are excluded at the 95% confidence level.

λ (mm)	α	$-\alpha$	$\lvert\alpha\rvert$
0.020	9.77×10^{5}	1.24×10^{6}	1.14×10^{6}
0.025	1.19×10^{5}	1.53×10^{5}	1.40×10^{5}
0.032	1.93×10^{4}	2.51×10^{4}	2.29×10^{4}
0.040	3.94×10^{3}	5.14×10^{3}	4.69×10^{3}
0.050	9.64×10^{2}	1.26×10^{3}	1.15×10^{3}
0.063	2.73×10^{2}	3.53×10^{2}	3.23×10^{2}
0.080	8.74×10^{1}	1.11×10^{2}	1.02×10^{2}
0.100	3.10×10^{1}	3.87×10^{1}	3.56×10^{1}
0.126	1.19×10^{1}	1.45×10^{1}	1.35×10^{1}
0.158	4.94	5.78	5.43
0.199	2.17	2.43	2.32
0.250	1.01	1.07	1.04
0.314	4.86×10^{-1}	4.96×10^{-1}	4.91×10^{-1}
0.395	2.43×10^{-1}	2.43×10^{-1}	2.43×10^{-1}
0.546	9.50×10^{-2}	1.02×10^{-1}	9.89×10^{-2}
0.754	3.72×10^{-2}	5.38×10^{-2}	4.84×10^{-2}
1.042	1.28×10^{-2}	3.63×10^{-2}	3.25×10^{-2}
1.439	2.07×10^{-3}	2.79×10^{-2}	2.56×10^{-2}
1.988	N/A	2.01×10^{-2}	1.86×10^{-2}
2.746	N/A	1.47×10^{-2}	1.36×10^{-2}
3.794	N/A	1.31×10^{-2}	1.21×10^{-2}
5.241	N/A	1.35×10^{-2}	1.25×10^{-2}
7.239	7.52×10^{-4}	1.28×10^{-2}	1.17×10^{-2}
10.000	1.86×10^{-3}	1.06×10^{-2}	9.66×10^{-3}

Table 7.6: 95% confidence level constraints of the combined data set.

λ (mm)	α	$-\alpha$	$\lvert\alpha\rvert$
0.020	9.89×10^{5}	1.23×10^{6}	1.14×10^{6}
0.025	1.23×10^{5}	1.49×10^{5}	1.39×10^{5}
0.032	2.03×10^{4}	2.32×10^{4}	2.19×10^{4}
0.040	4.12×10^{3}	4.26×10^{3}	4.19×10^{3}
0.050	6.84×10^{2}	1.17×10^{3}	1.04×10^{3}
0.063	2.11×10^{2}	2.53×10^{2}	2.36×10^{2}
0.080	6.62×10^{1}	5.62×10^{1}	6.20×10^{1}
0.100	2.01×10^{1}	1.74×10^{1}	1.89×10^{1}
0.126	6.66	6.09	6.40
0.158	2.41	2.36	2.38
0.199	9.37×10^{-1}	9.87×10^{-1}	9.63×10^{-1}
0.250	3.88×10^{-1}	4.39×10^{-1}	4.17×10^{-1}
0.314	1.71×10^{-1}	2.05×10^{-1}	1.91×10^{-1}
0.395	8.05×10^{-2}	1.01×10^{-1}	9.27×10^{-2}
0.546	3.14×10^{-2}	4.10×10^{-2}	3.74×10^{-2}
0.754	1.45×10^{-2}	1.99×10^{-2}	1.80×10^{-2}
1.042	7.87×10^{-3}	1.25×10^{-2}	1.11×10^{-2}
1.439	4.63×10^{-3}	1.07×10^{-2}	9.50×10^{-3}
1.988	2.37×10^{-3}	1.13×10^{-2}	1.03×10^{-2}
2.746	9.39×10^{-4}	1.16×10^{-2}	1.07×10^{-2}
3.794	3.13×10^{-4}	1.19×10^{-2}	1.10×10^{-2}
5.241	5.81×10^{-4}	1.25×10^{-2}	1.15×10^{-2}
7.239	1.75×10^{-3}	1.15×10^{-2}	1.05×10^{-2}
10.000	2.38×10^{-3}	1.00×10^{-2}	9.04×10^{-3}

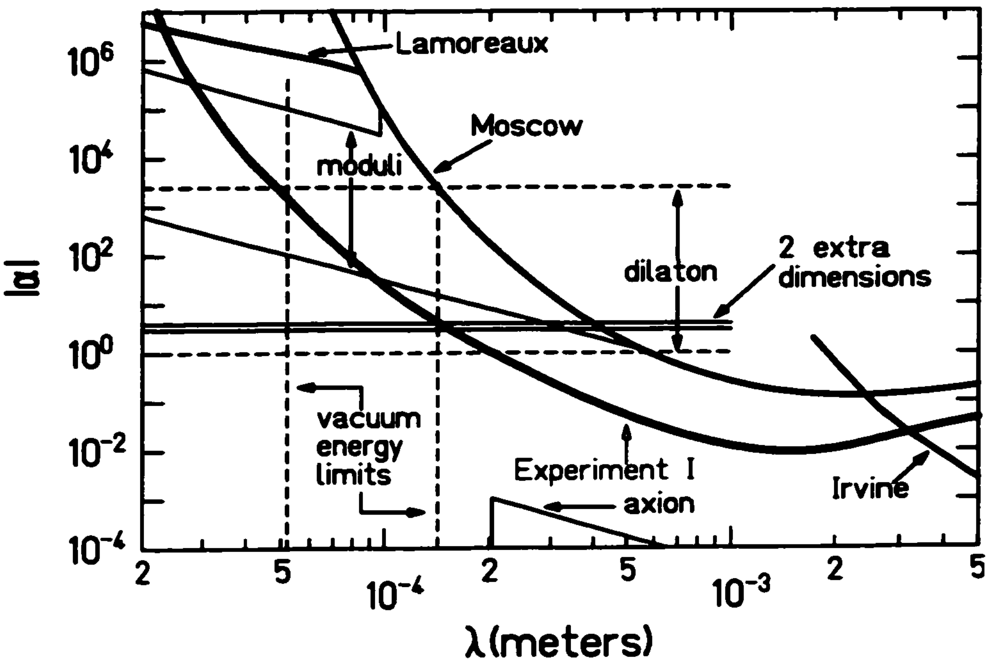

Figure 7.5: Constraint from Experiment I on a Yukawa violation of the ISL. The area above the curve is excluded at the 95% confidence level. We made an improvement over previous work by up to a factor of $\sim 10^4$. The relaxation of the constraint at large distances is due to the 2.5% overall scale factor uncertainty.

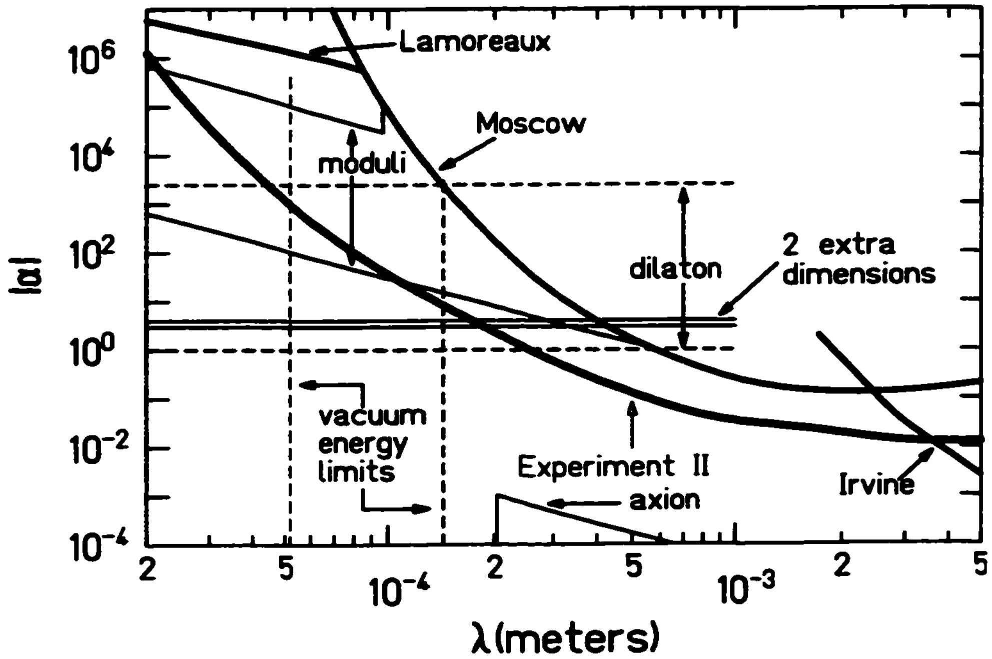

Figure 7.6: Plot of the 95% confidence level constraint on $|\alpha|$ obtained from the Experiment II data set. The improved scale factor uncertainty gives a better constraint at large λ. We also obtained an improved constraint at very short distances because the minimum separation achieved for this data set was smaller than that of Experiment I.

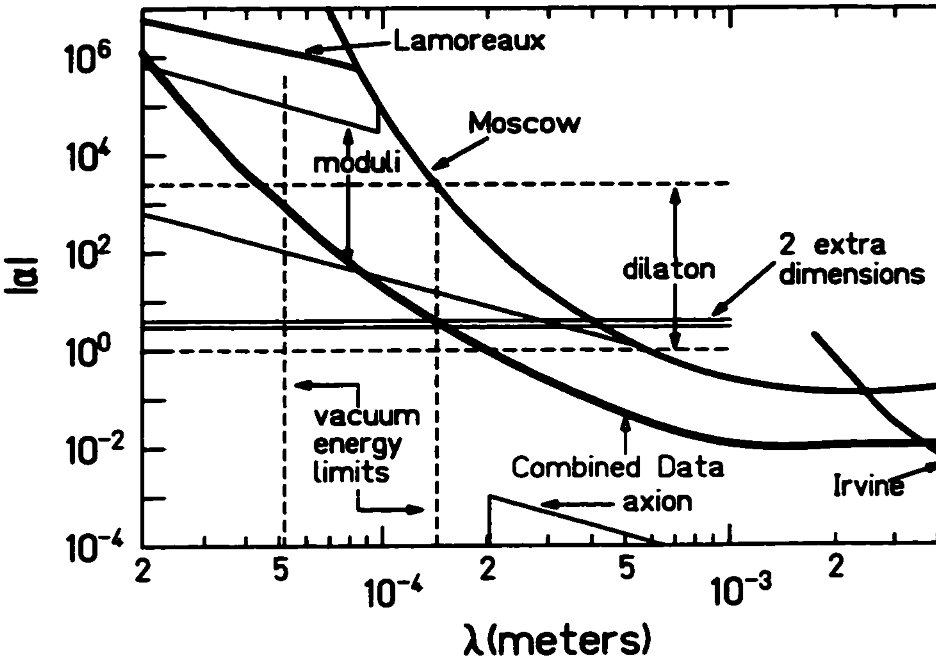

Figure 7.7: 95% confidence level constraint obtained from the combined data set.

Chapter 8

CONCLUSIONS: IMPLICATIONS OF THE RESULTS

The results provide stringent new constraints on extensions of the Standard Model. We detected no new physics; the gravitational ISL proved valid over our experimental distance scale. The limits we establish in the following sections use the constraint on $|\alpha|$ from the combined analysis, shown in Figure 7.7.

8.1 Constraints on Extra Dimension Scenarios

Our results provide the most sensitive direct measurements to date on the size of large extra dimensions. According to the formalism discussed in Ref. [9], we may use these results to constrain the size of the largest of any extra dimension. We assume the extra dimensions are not of equal size and the compactification geometry is taken to be an orbifold. In this case, if one of these extra dimensions is substantially larger than the others, we would expect its strength to be $\alpha = 1$, and its size $R^* = \lambda$. By determining the point at which the curve from Figure 7.7 crosses the line $|\alpha| = 1$ we may constrain the largest extra dimension to have a size $\lesssim 200$ μm. This represents a factor of 3 improvement over previous experiments.

We saw in Chapter 1 that in the particular case that all of the extra dimension have equal size (such as the scenario proposed in Ref. [5]), one should observe a deviation from inverse-square behavior with a strength of 3-4 times that of gravity with two large extra dimensions. Since $R^* = \lambda$ for this scenario as well, we may constrain the size of the extra dimensions to be ≤ 150 μm, the point at which the curve in

Figure 7.7 crosses $|\alpha| = 3$. Again we obtained a three-fold improvement over previous experiments on the size of such extra dimensions. If we use Equation 1.4 (with $n = 2$) to convert this to a minimum unification energy scale, we find $M^* \geq 4.0$ TeV.

8.2 Application to Other Theoretical Models

Other models, such as those which predict violations of the gravitational ISL from new particles or the vacuum energy density associated with the cosmological constant, are less precise in predicting the expected values of α and λ. However, by inspection of Figure 7.7, we see that the results of this work have eliminated a large region of the parameter space encompassed by these predictions. In particular, we place conservative limits by considering the points at which our constraint crosses the upper boundary of the predictions.

For dilaton and moduli interactions we may take an upper limit for the associated Yukawa range of the particles. We exclude all moduli with a range (which we may interpret as a Compton wavelength) greater than $\sim$ 90 μm at the 95% confidence level. This constraint implies the mass of the lightest modulus must be $m \gtrsim \hbar c/\lambda \approx$ 0.002 eV. Similarly, the dilaton mass is constrained to be greater than $\sim$ 0.001 eV. Our constraints on the strength of the interactions mediated by these particles improve upon previous constraints by up to a factor of 10^4 for Yukawa ranges down to 20 μm. Again, these are the best limits to date on the properties of interactions mediated by these particles.

The region labeled "vacuum energy limits" in Figure 7.7 shows the region associated with an ISL violation arising from the energy density of the cosmological constant as described in Ref. [16]. We see that our results constrain such an interaction to have a strength relative to gravity of $\alpha \lesssim 1000$ for $\lambda = 50$ μm. This limit represents an improvement over the previous constraint by a factor of about 1000. Because these theoretical models favor an interaction strength of $|\alpha| \sim 1$ for $\lambda \sim 0.1$ mm, this remains a very interesting region of parameter space to probe (these values lie just outside the region constrained by these experiments).

8.3 The Next Generation Eöt-wash Short-Range Experiment

We are currently in the process of performing a next-generation experiment, based on the same general principles, with which we hope to probe gravity at length scales below $\sim 100\ \mu$m. The pendulum and attractor for this experiment have 22-fold symmetry and have shapes optimized to test gravity at shorter distances. A schematic drawing of the new pendulum and attractor pair is shown in Figure 8.1.

We have already made many improvements that will increase the sensitivity of this next measurement dramatically. First, the pendulum and attractor are both made from molybdenum. The increased density of this material automatically increases our sensitivity to short-range interactions by a factor $\rho_{Mo}^2/(\rho_{Cu}\ \rho_{Al}) \approx 4.3$. Precise placement of the holes has suppressed the torque from Newtonian gravity by a factor of 5 over the configurations reported here. Other improvements, such as a new magnetic damper, mechanical supports, torsion fiber, and data acquisition system have already improved the statistical noise for a typical run by a factor of $\sim$3-4.

Future improvements planned for this apparatus include better thermal and seismic isolation and the implementation of a very clean environment surrounding the instrument. Cleanliness is a major factor in achieving the smallest possible pendulum-to-attractor separation. We are also investigating different machining techniques which may allow the implementation of more sensitive geometries.

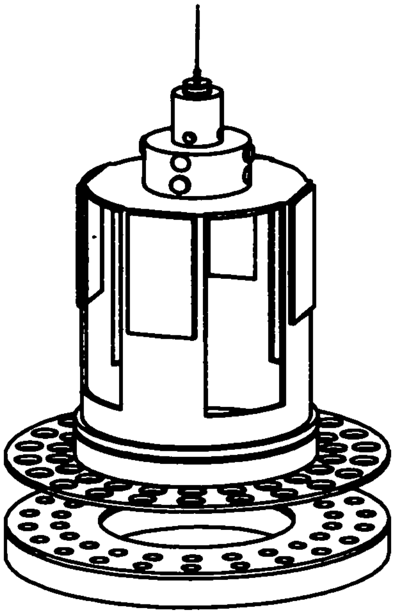

Figure 8.1: Schematic of the next generation short-range experiment. The design has 22-fold rotational symmetry. Newtonian torques are suppressed to a high degree and short-range effects are enhanced relative to the previous experiments.

BIBLIOGRAPHY

[1] I.I. Shapiro *et al.* *Phys. Rev. Lett.*, 28:1594, (1972).

[2] J.H. Taylor. *Class. Quantum Grav.*, 10:S167, (1993).

[3] R.V. Pound and J.L. Snider. *Phys. Rev. Lett.*, 13:539, (1964).

[4] R.J. Weyman *et al.* *Nature*, 285:641, (1980).

[5] N. Arkani-Hamed, S. Dimopoulos, and G. Dvali. *Phys. Lett. B*, 429:263, (1998).

[6] N. Arkani-Hamed, S. Dimopoulos, G. Dvali, and N. Kaloper. *Phys. Rev. Lett.*, 84:586, (2000).

[7] A. Kehagias and K. Sfetsos. *Phys. Lett. B*, 472:39, (2000).

[8] E.G. Floratos and G.K. Leontaris. *Phys. Lett. B*, 465:95, (1999).

[9] K. Dienes, private communication.

[10] L. Randall and R. Sundrum. *Phys. Rev. Lett.*, 83:4690, (1999).

[11] D.B. Kaplan and M.B. Wise. *J. High Energy Phys.*, 0008:37, (2000).

[12] S. Dimopoulos and G.F. Giudice. *Phys. Lett. B*, 379:105, (1996).

[13] R. Sundrum. *J. High Energy Phys.*, 9907:1, (1999).

[14] A.G. Riess *et al. Astron. J.*, 116:1009, (1998).

[15] S. Perlmutter *et al. Astrophys. J.*, 517:565, (1999).

[16] Silas R. Beane. *hep-ph/9702419*, (1997).

[17] E. Fischbach and C.L. Talmadge. *The Search for Non-Newtonian Gravity.* Springer-Verlag, New York, (1999).

[18] C. Hanhart, D.R. Phillips, S. Reddy, and M.J. Savage. *nucl-th/0007016v2*, (2000).

[19] S. Cullen and M. Perelstein. *Phys. Rev. Lett.*, 83:268, (1999).

[20] T. Ferbel. *hep-ex/0103009v2*, (2001).

[21] C. Adloff *et al. Phys. Lett. B*, 479:358, (2000).

[22] M. Acciarri *et al. Phys. Lett. B*, 464:135, (1999).

[23] S.K. Lamoreaux. *Phys. Rev. Lett.*, 78:5, (1997).

[24] V.P. Mitrofanov and O.I. Ponomareva. *Sov. Phys. JETP*, 67:1963, (1989).

[25] J.K. Hoskins, R.D. Newman, R. Spero, and J. Schultz. *Phys. Rev. D*, 32:3084, (1985).

[26] G.C. Long, H. Chang, and J. Price. *Nucl. Phys.*, B529:23, (1999).

[27] G.L. Smith, C.D. Hoyle, J.H. Gundlach, E.G. Adelberger, B.R. Heckel, and H.E. Swanson. *Phys. Rev. D*, 61:145, (2000).

[28] G.L. Smith. *A Short Range Test of the Universality of Free Fall.* PhD thesis, University of Washington, (1996).

[29] J.H. Gundlach, G.L. Smith, E.G. Adelberger, B.R. Heckel, and H.E. Swanson. *Phys. Rev. Lett.*, 78:2523, (1997).

[30] L.D. Landau, E.M. Lifshitz, and L.P. Pitaevskii. *Electrodynamics of Continuous Media.* Pergamon Press, New York, (1984).

[31] Presently at Phsikalisches Institut, Heidelberg, Germany.

[32] W.H. Press, S.A. Teukolsky, W.T. Vetterling, and B.P. Flannery. *Numerical Recipes in C.* Cambridge University Press, New York, second edition, (1996).

[33] P.R. Saulson. *Phys. Rev. D*, 42:2437, (1990).

[34] Y. Su. *A New Test of the Weak Equivalence Principle.* PhD thesis, University of Washington, (1992).

[35] C.D. Hoyle, U. Schmidt, B.R. Heckel, E.G. Adelberger, J.H. Gundlach, D.J. Kapner, and H.E. Swanson. *Phys. Rev. Lett.*, 86:1418, (2001).

VITA

Charles D. Hoyle, Jr. was born in Vallejo, California on April 23, 1974 but spent much of his youth in Stillwater, Minnesota. He attended the University of Colorado in Boulder, Colorado and earned a B.A. (cum laude) in Physics in May, 1996. He entered the Physics Department at the University of Washington in July of that same year, initially studying Nuclear Physics with Professor Adelberger. He joined the Eöt-Wash Gravity Group in April, 1997 and earned his M.S. that December.